UNIVERSITY OF GAZİANTEP

GRADUATE SCHOOL OF NATURAL & APPLIED SCIENCES

ANALYSIS, APPLICATIONS, AND A NOVEL DESIGN OF DOUBLE NEGATIVE METAMATERIALS

Ph. D. THESIS

IN

ELECTRICAL & ELECTRONICS ENGINEERING

BY

CUMALİ SABAH

JUNE 2008

Analysis, Applications, and a Novel Design of Double Negative Metamaterials

Ph. D. Thesis

in

Electrical & Electronics Engineering

University of Gaziantep

By

Cumali SABAH

June 2008

For everything in the world – for civilization, for life, for success – the truest guide is knowledge and science.

Mustafa Kemal ATATÜRK

The Great Founder of Modern Republic of Türkiye

ABSTRACT

ANALYSIS, APPLICATIONS, AND A NOVEL DESIGN OF DOUBLE NEGATIVE METAMATERIALS

Cumali SABAH

Ph. D. in Electrical and Electronics Engineering

Supervisor: Prof. Dr. Savaş Uçkun

June 2008, 179 pages

Double negative metamaterials are composite materials in which both the permittivity and the permeability are simultaneously negative over a certain frequency band and constructed artificially. They are designed to show specific and unfamiliar electromagnetic features not commonly found in nature. Also, their physical features are different from the conventional materials. Due to these unique physical features, double negative metamaterials attracted a great amount of attention in recent years. In this thesis, the properties and potential applications of double negative metamaterials are explored. In addition, some tools are presented to realize new types of metamaterials in the microwave frequency range.

First, the fundamental electromagnetic properties of double negative metamaterials are investigated. The plane wave in double negative medium, left-handed systems, the extraordinary features of double negative metamaterials, and negative refraction are given in detail. Second, the characterization and realization of

double negative metamaterials are studied to form a base about how they can be created and generated. In this manner, the analytical (hypothetical, Lorentz, Drude, and cold plasma media) and physical models are analyzed. Then, electromagnetic wave propagation in the presence of double negative metamaterial is studied. Normal and oblique incidence cases for the planar boundaries of two semi infinite media containing conventional dielectric medium and double negative metamaterial are examined. Both the theoretical and numerical results are given. Next, the slab of double negative metamaterial sandwiched between two different semi-infinite dielectric media is studied. Additionally, some simulations are illustrated for the application purpose of perfect lens and parabolic wave refractor. After that, double negative metamaterials are used to design and analyze several types of stratified structures. Mirrors, high reflection coatings, distributed Bragg reflector, stratified cold plasma stacks, and the combination of multilayer cold plasma, Lorentz, and Drude layers with conventional dielectric slabs are created in order and their scattering characteristics are shown. The advantageous of the stratified structures containing double negative metamaterials versus the conventional multilayer structures are also discussed. High reflection and transmission coatings; band pass, stop band, reflection, transmission, multi band-pass, multi saw-comb, oscillating, and multi notch filters characteristics at some frequency regions are obtained in the numerical investigation. These results can be used to generate new devices and equipments such as reflectors, coatings, and filters with high efficiency. At last, new types of metamaterials that exhibit negative refraction properties at the microwave frequency range are designed. This novel metamaterials are constructed using triangular split ring resonator and wire strip. Three new metamaterials comprised of triangular split ring resonator and wire strip are created and simulated. After designing and creating processes, novel metamaterial slabs are manufactured using hot-press technique. Then, some transmission experiments are provided to observe the characteristics of these novel metamaterials experimentally. These new materials can be used for several potential applications of double negative metamaterials in the microwave, millimeter wave and optical regimes.

Key Words: Double Negative Medium, Metamaterial, Lorentz, Drude, Cold Plasma, Multilayer Structures, Triangular Split Ring Resonator.

ÖZET

ÇİFT NEGATİF METAMALZEMELERİN ANALİZ, UYGULAMA VE YENİ TASARIMI

Cumali SABAH

Doktora Tezi, Elektrik ve Elektronik Mühendisliği Bölümü

Tez Yöneticisi: Prof. Dr. Savaş Uçkun

Haziran 2008, 179 sayfa

Çift negatif metamalzemeler, elektrik ve manyetik geçirgenlikleri belirli bir frekans aralığında negatif olan ve yapay olarak elde edilen bileşik malzemelerdir. Bu malzemeler, genel olarak doğada bulunmayan, kendine özgü ve farklı elektromanyetik özellikler gösterebilmeleri için tasarlanırlar. Bunların fiziksel özellikleride bilinen malzemelerden farklıdır. Bu benzersiz fiziksel özelliklerinden dolayı, çift negatif metamalzemeler son yıllarda büyük ölçüde ilgi odağı olmuşlardır. Bu tezde, çift negatif metamalzemelerin özellikleri ve potansiyel uygulama alanları araştırılmıştır. Buna ilaveten, mikrodalga frekansı aralığında yeni tür metamalzemelerin gerçekleştirilmesi için bazı uygulamalar sunulmuştur.

İlk olarak, çift negatif metamalzemelerin temel elektromanyetik özellikleri incelendi. Çift negatif ortam içerisindeki düzlemsel dalga, solak sistemler, çift negatif metamalzemelerin olağandışı özellikleri ve negatif kırılma kavramları detaylıca verildi. İkinci olarak, çift negatif metamalzemelerin nasıl yaratıldığı ve

oluşturulduğuna temel oluşturmak için, bu malzemelerin tanımı ve niteliği çalışıldı. Bu bağlamda, analitik (hypothetical, Lorentz, Drude ve soğuk plazma ortamları) ve fiziksel modeller analiz edildi. Daha sonra, çift negatif metamalzemelerin varlığında bulunan elektromanyetik dalga yayılımı çalışıldı. Bilinen yalıtkan ortam ve çift negatif metamalzemeden oluşan yarı sonsuz iki düzlemsel ortama dik ve açılı gelen dalga durumları incelendi. Teorik ve nümerik sonuçların ikiside verildi. Bundan sonra, iki farklı yalıtkan ortam arasına yerleştirilmiş çift negatif metamalzeme dilimi çalışıldı. Buna ilaveten, mükemmel mercek ve parabolik dalga kırıcı amaçlı uygulamalar için bazı simülasyonlar gösterildi. Sonra, çok katmanlı yapıların tasarım ve analizi için çift negatif metamalzemeler kullanılarak çeşitli yapılar oluşturuldu. Sırasıyla, aynalar, yüksek yansımaya sahip katman ve kaplamalar, dağıtıcı Bragg yansıtıcılar, çok katmanlı soğuk plazma dilimleri; ve bilinen yalıtkan ortamlar ile birleştirilmiş çok katmanlı soğuk plazma, Lorentz ve Drude tabakları oluşturulup bunların karakteristik özellikleri gösterildi. Çift negatif metamalzemeler içeren çok katmanlı yapıların, bilinen çok katmanlı yapılara karşı avantajları tartışıldı. Nümerik sonuçlarda, bazı frekans aralıkları için yüksek yansıma ve iletime sahip katmanlar; bant geçiren, söndürme kuşağı bandı, yansıma, iletim, çoklu bant geçiren, çoklu testere-tarak, salınım ve çoklu çentik filtre karakteristikleri elde edildi. Bu sonuçlar, yansıtıcılar, kaplamalar ve süzgeçler gibi yeni aygıt ve aletlerin üretilmesi için kullanılabilir. Sonunda, mikrodalga frekansı aralığında negatif kırılma özellikleri gösteren yeni tip metamalzemler tasarlandı. Bu yeni metamalzemler, üçgensel halka şeklindeki ucu açık (yarıklı) rezonatörler ve tel şeritler kullanılarak oluşturludu. Üçgensel halka şeklindeki ucu açık rezonatörler ve tel şeritlerden oluşan üç adet yeni metamalzeme meydana getirildi ve simülasyonu yapıldı. Tasarım ve oluşturma işlemlerinden sonra, sıcak pres (ütüleme) yöntemi ile yeni metamalzeme katmanları imal edildi. Daha sonra, yeni metamalzemelerin özelliklerini deneysel olarak gözlemlemek için bazı iletim deneylerinin yapımı sağlandı. Bu yeni malzemeler, mikrodalga, milimetre dalga ve optik sistemlerde çift negatif metamalzemelerin çeşitli potansiyel uygulamalarında kullanılabilirler.

Anahtar Kelimeler: Çift Negatif Ortam, Metamalzeme, Lorentz, Drude, Soğuk Plazma, Çok Katmanlı Yapılar, Üçgensel Halka Şeklindeki Ucu Açık Rezonatör.

ACKNOWLEDGEMENTS

CONTENTS

LIST OF FIGURES

xiii

xiv

LIST OF TABLES

NOMENCLATURE

List of Symbols

ε, μ Permittivity and permeability of the medium

ε_o, μ_o Permittivity and permeability of free space

ε_i, ε_s, ε_t Permittivities of the incident, DNS and transmitted medium

μ_i, μ_s, μ_t Permeabilities of the incident, DNS and transmitted medium

$\boldsymbol{k}$ Wave propagation vector

k Wave number of the medium

k_i, k_r, k_t Wave numbers of the incident, reflected, and transmitted medium

k_0, k_s Wave number of free space and the double-negative slab

$\boldsymbol{k}_s^+$, $\boldsymbol{k}_s^-$ Wave propagation vector of the forward and backward wave

$\boldsymbol{S}$ Poynting vector

n Refractive index

$\boldsymbol{r}$ Distance vector in spherical coordinate system

$\boldsymbol{a}_x$, $\boldsymbol{a}_y$, $\boldsymbol{a}_z$ Unit vectors along x-, y-, and z- axis

ω Angular frequency

f_{ep}, f_{mp}	Electric and magnetic plasma frequencies
f_{eo}, f_{mo}	Electric and magnetic resonance frequencies
δ_e, δ_m	Electric and magnetic damping frequencies
c	speed of light
$\boldsymbol{E}$, $\boldsymbol{H}$	Electric and magnetic field vector
$\boldsymbol{E}_i$, $\boldsymbol{E}_r$, $\boldsymbol{E}_t$	Incident, reflected, and transmitted electric field vectors
E_i, E_r, E_t	Magnitude of the incident, reflected, and transmitted electric field vectors
$\boldsymbol{E}_s$	Total electric field vector in the double-negative slab
E_s^+, E_s^-	Forward and backward electric fields in the double-negative slab
θ_i, θ_r, θ_t	Incidence, reflection and transmission angles
θ_s^-, θ_s^+	The transmission and the reflection angles in double-negative slab
θ_c	Critical angle
$[U]$	Transfer matrix
u_{ab}	The elements of the transfer matrix
P_r, P_t	Reflected and transmitted powers
$R^{TE, TM}$	Reflection coefficient of TE and TM waves
$T^{TE, TM}$	Transmission coefficient of TE and TM waves
S_{11}, S_{21}	S parameters

CHAPTER 1

INTRODUCTION

Electromagnetic wave theory is well-established scientific discipline which has wide variety of applications in science and technology include, but are not limited to, electromagnetic materials, remote sensing, power systems, wireless communications, radar systems, and optics. Unconventional materials such as composite and/or complex media are the part of electromagnetic materials research and one of the most challenging areas in the electromagnetics' community. Metamaterials are well-known composite/complex media and there has been a growing interest on the studies of them due to their numerous potential applications. Today, metamaterials are classified with different names due to their various composition elements such as plasmas, photonic crystals, double negative metamaterials, single negative materials, and chiral media. It is very difficult to find a suitable definition for the term metamaterial. There are many definitions existing in the literature and some of them are given as follows:

- Electromagnetic metamaterials are artificially structured composites that can be engineered to have desired electromagnetic properties, while having other advantageous material properties [1].

- Structures composed of macroscopic scattering elements [2].

- Meta-materials, materials whose permeability and permittivity derive from their structure [3].

- Metamaterials are a new class of ordered nanocomposites that exhibit exceptional properties not readily observed in nature. These properties arise

from qualitatively new response functions that are not observed in the constituent materials and result from the inclusion of artificially fabricated, extrinsic, low dimensional inhomogeneities [4].

- Metamaterials are defined as macroscopic composites having a man-made, three dimensional, periodic cellular architecture designed to produce an optimized combination, not available in nature, of two or more responses to a specific excitation. Each cell contains metaparticles, macroscopic constituents designed with low dimensionality that allow each component of the excitation to be isolated and separately maximized. The metamaterial architecture is selected to strategically recombine local quasi-static responses, or to combine or isolate specific non-local responses [5].

- Metamaterials, which are broadly defined as effectively homogenous artificial structures with unusual properties, represent a new paradigm in physics and engineering [6].

The prefix *meta* comes from Greek (it is also used in Latin) and it means *after*. Often the prefix is used also for *along with*, *beyond*, *among*, *in the midst of*, *according to*, and *behind*. There are numerous words in English and other languages starting with *meta* like, for example, *metabolism*, *metalinguistics*, *metamerism*, *metaphysics*, *metamorphosis*, *metastasis*, etc. However, the common word in engineering, *metal* is of different origin. With this background in mind, it seems that in the choice and use of metamaterial, this meta-prefix emphasizes the transcendental aspect of the meaning. A metamaterial needs to be qualitatively different from its components. New phenomena and novel properties should emerge when *ordinary* pieces are brought together. The whole should be more than the sum of its parts. Quantitative differences become qualitative ones. There is a word such a behavior of systems. It is *emergence* [7].

The idea of double negative (DNG) metamaterials has recently achieved a significant importance in electromagnetics' community due to the exhibition of their

unusual properties different from any known media in some microwave, millimeter-wave and optical frequency bands. The progress of the fabrication technologies enables the construction of them at these frequency bands, and so their potential applications are growing day by day. Basically, DNG metamaterial is, by definition, a composite material in which both the permittivity and the permeability are simultaneously negative over a certain frequency band whose electromagnetic features are different from the conventional materials and constructed artificially. These are the hand made structures that can be designed to show specific and unexplored electromagnetic properties not commonly found in nature. Several terminologies are recommended for DNG metamaterials such as left-handed media (LHM), double negative (DNG) materials, backward-wave media (BW media), negative index media (NIM), negative refractive index metamaterials (NRM), negative index of refraction media (NIR), and etc. The phenomena of DNG metamaterial and stratified DNG metamaterials are discussed in detail throughout this thesis, and the results of this discussion may enable to design and characterization of them for specific applications on new devices, components, and apparatus such as filters, absorbers, lenses, microwave components, antennas, and etc.

Basically, electromagnetic wave interactions through the semi-infinite, single slab, stratified DNG metamaterial layers, and the design of novel DNG metamaterials will be analyzed and studied in this thesis. In addition, the combination of stratified double negative metamaterial and dielectric layers will be investigated. Perfect lens, parabolic refractor, and some filter applications of DNG metamaterials will be shown. Then, the design and realization of novel DNG metamaterials based on triangular split ring resonators and wire strips will be studied. Simulation results will be presented for the realization purpose. After that, some transmission experiments will be performed using new metamaterial slabs to examine their characteristics in the microwave frequency band.

1.1 Background

The concept of artificial materials appears to begin in the late nineteenth century, in 1898, with the study of Indian scientist Jagadis Chunder (or Chandra) Bose on optical activity [8]. He conducted the first microwave experiment on twisted structures which were essentially artificial chiral materials by today's definition. Later in 1914, Karl F. Lindman, who is the first scientist showing the effect of a chiral medium on electromagnetic waves, worked on artificial chiral media by embedding many randomly oriented small wire helices in a host medium [9]. In 1948, W. E. Kock made lightweight microwave lenses by arranging conducting spheres, disks, and strips periodically and effectively tailoring the effective refractive index of the artificial media [10]. Then, Tinoco and Freeman were interested in chiral phenomena and the rotation of the polarization plane of linearly polarized waves in 1957 [11]. After that, Harvey showed that some devices and components can be constructed by length scaling using artificial materials for application in the lower frequencies [12]. Since then, artificial complex materials have been subject of research for many scientist and DNG metamaterials are the last version of artificial materials that extensively cover the recent studies in the electromagnetics' community at the present time.

DNG metamaterials were first envisioned by Russian physicist Victor G. Veselago in 1967 [13]. He investigated various electromagnetic properties of such material and presented that the electric field vector E, the magnetic vector H, and the wave vector k form a left-handed triplet of vectors, and the Poynting vector S and the wave number k are in opposite directions. In addition, he showed the Doppler effect and Vavilov-Cerenkov radiation is reversed in DNG metamaterial. He also showed the negative refraction and backward waves in this metamaterial. However, some ideas on negative refraction and backward waves were suggested by many scientists long before Veselago's work. In 1904, H. Lamb suggested the existence of backward waves in which the phase of waves moves in the direction opposite from that of the energy flow [14]. In his study, he proposed a certain artificial mechanical model of a

one-dimensional medium in which the group velocity can be negative. Apparently, he himself did not think his example could have any physical application. But as it turns out, there exist entirely real media in which for certain frequency ranges the phase and group velocities are in fact directed towards each other. Note that, his examples involved the mechanical systems rather than electromagnetic waves. Around the same time, A. Schuster, who discussed the backward waves in electromagnetism, briefly notes Lamb's work in his book and gives a speculative discussion of its implications for optical refraction, should a material with such a properties ever be found [15]. He cited the fact that within the absorption band of, for example, sodium vapour a backward wave will propagate. But, because of the high absorption region in which the dispersion is reversed, he was pessimistic about the applications of negative refraction. In 1905, H. C. Pocklington showed that in a specific backward-wave medium, a suddenly activated source produces a wave whose group velocity is directed away from the source, while its velocity moves toward the source [16]. Then, Mandel'shtam himself referred to Lamb's study; and the problems of energy velocity and its relation to group velocity were presented [17], [18]. The effect of negative group velocity on the familiar problems of reflection and refraction and the negative group velocity in crystal lattices were also considered in his studies. Next, the radiation property as in the previous works was rediscovered by G. D. Malyuzhinets in 1951 [19]. He noted that the phase velocity of waves at infinity should point from infinity to the source in DNG metamaterials. What was perhaps even more interesting, he considered as an example a one-dimensional artificial transmission line. After that, general properties of wave propagation in a medium with negative refractive index have been discussed by D. V. Sivukhin [20]. He noticed that media with negative parameters are backward wave media, but had to state that media with negative permittivity and permeability are not known. The question on the possibility of their existence has not been clarified. Some unusual aspects of the transition radiation and Cherenkov radiation in the frequency region characterized by negative group velocities have been revealed by V. E. Pafomov in his studies between 1956 and 1959 [21–23]. The negative refraction phenomenon in periodical media was discussed by R. A. Silin in 1959 [24]. Note that, the studies mentioned in [14–24] were not systematic studies and it is assumed that they were related with the backward wave and its negative velocity works. But the study of Veselago was a systematic study of electromagnetic

properties of materials with negative parameters. Due to this reason the study of Veselago has been usually considered as the first study which was published in Russian in 1967 and translated into English in 1968. In addition, there were many studies in the literature after Veselago's study [25–34].

At last, the concept of negative permittivity and negative permeability came to true by Pendry's studies. Pendry *et al.* presented their studies in 1996 [35] on the artificial metallic construction which shows the negative permittivity and in 1999 [36] on the split rings which show the negative permeability. In 2000, Smith *et al.* realized the construction of the DNG material using the combination of the split rings and wires [37]. They carried out many experiments at microwave frequencies to show the characteristics of DNG material. In 2001, Shelby *et al.* performed the first experimental investigation of the negative refraction on the DNG materials at microwave frequencies [38]. The results of this experiment done for the negative refraction are criticized by Valanju *et al.* in 2002 [39]. They stated that negative refraction is impossible for any real physical signal with the finite bandwidth. This statement was found incorrect by Pendry and Smith in 2003 [40]. Ziolkowski and Heyman studied the electromagnetic wave propagation in DNG analytically and numerically to observe the characteristic features of propagation and scattering in DNG and to apply the results to perfect lens notion [41]. Kong examined the electromagnetic wave interaction with stratified DNG isotropic media [42]. He investigated in detail the reflection and transmission analysis, field solution of guided waves, linear and dipole antennas in stratified DNG media. Conceptual and speculative ideas for potential applications of the DNG materials were suggested, and physical remarks and intuitive comments were provided by Engheta in 2002 [43]. Mathematical analysis and physical explanations for some structures are also given in his study. Chew studied some reflection on the DNG material in 2005 [44]. The energy conservation property of a DNG material and the realistic Sommerfeld problem of a point source over a DNG material half space and a DNG slab are analyzed in [44].

The studies on DNG metamaterials continue to be of great interest and practical importance for the researcher due to the progress of the fabrication technologies and the variety potential applications [45–61].

1.2 Thesis Motivation

The main purpose of this thesis is to understand the basic properties of DNG metamaterials, to present their potential applications formed by stratified DNG metamaterials, and to show wave interactions with DNG metamaterials. In addition to these, the design of new DNG metamaterials is in the main goals of this thesis. In the following, the organization of this thesis is briefly outlined.

The aim of Chapter 2 is understand the fundamental electromagnetic properties of DNG metamaterials in detail. The most important contribution of this chapter is to provide the solid understanding of the plane wave in DNG medium, left-handed systems, the unusual and extraordinary features of DNG metamaterials, and negative refraction. This chapter will provide to easily recognize the concept of DNG metamaterials especially in the following chapters.

The major point of Chapter 3 is to study characterization and realization of DNG metamaterials. The contribution of this chapter is to provide a perceptive that how DNG metamaterials can be generated both analytically and physically. In the analytical models, hypothetical, Lorentz, Drude, and cold plasma medium models are used to create DNG metamaterials. Additionally, physical models are mentioned throughout this chapter. The relationships between the analytical and physical models are also given. The results of this chapter will be used in the design and development process to generate novel DNG metamaterials and new structures containing DNG metamaterials for the potential applications.

In the fourth chapter, we will have the concept of the electromagnetic wave propagation in the presence of DNG metamaterial. We will begin from normal incidence and continue with oblique incidence for the planar boundaries of two semi infinite media containing conventional dielectric medium and DNG metamaterial. Both the theoretical and numerical results will be given. Then, the slab of DNG metamaterial sandwiched between two different semi infinite dielectric media will be studied. Hypothetical, Lorentz, Drude, and cold plasma medium models mentioned in Chapter 3 are used to realize DNG metamaterial. Additionally, for the purpose of the potential application of the DNG metamaterial, some simulation will also be provided. Especially, the applications of flat lens and parabolic wave refractor will be presented in these simulations. Most of the work presented in Chapter 4 appeared as articles in Journal of Optoelectronics and Advanced Materials [62] and Opto-Electronics Review [63].

The final two chapters are concerned with addressing the potential applications of DNG metamaterials. In Chapter 5, DNG metamaterials will be used to design and analyze stratified structures. The motivation of this work was to investigate the potential benefits of being able to design some stratified structures with DNG metamaterials. So that, mirrors with DNG slabs, high reflection coatings consisted of DNG and DPS layers, distributed Bragg reflector (DBR) based on DNG and DPS slabs, stratified DNG stacks of cold plasma medium, multilayer media comprised of DNG stacks of cold plasma and conventional DPS layers, and multilayer structure of DNG Lorentz/Drude Medium with DPS slabs will be created and their scattering characteristics will be shown in this chapter. The advantageous of the mentioned structures containing DNG metamaterials versus the conventional structures are also discussed. Some important results are obtained in this investigation and they can be used to generate new devices and equipments such as reflectors, coatings, and filters with high efficiency. Some of the achievements represented in Chapter 5 are published as scientific articles in Chinese Physics Letters [64], Journal of Optoelectronics and Advanced Materials [65], and Zeitschrift für Naturforschung A (A Journal of Physical Sciences) [66]. Some of the contents of this chapter have also been submitted to the international SCI journal for the consideration of publication.

In Chapter 6, new types of metamaterials that have negative permittivity and permeability at the microwave frequency range will be presented. This novel metamaterials are constructed using triangular split ring resonator and wire strip. Three new metamaterials comprised of triangular split ring resonator and wire strip are created and simulated. Then, it will be shown that the mentioned novel metamaterials have simultaneously negative permittivity and permeability over a certain frequency band. Thus, they can be used for several potential applications in the microwave, millimeter wave and optical regimes. At last, some new metamaterial slabs will be manufactured to make transmission experiments to explore the characteristics of new metamaterial slabs. Some parts of this chapter have been submitted to the international SCI journal for the consideration of publication.

In the conclusion part, a brief summary of the results obtained during this thesis work will be included. Future works and further studies for potential applications of the DNG materials will be suggested, and physical remarks and intuitive comments will also be provided in this part.

CHAPTER 2

FUNDAMENTALS OF DOUBLE NEGATIVE METAMATERIALS

2.1 Introduction

In this chapter, common electromagnetic features of DNG metamaterials will be introduced and discussed in detail. We will start from the dispersion characteristics of DNG metamaterial and then continue with electrical and magnetic properties of such material. After that, general properties of this kind of media and the concept of negative refection will be given. In this manner, the fundamentals of DNG metamaterials will be overviewed and examined.

2.2 Dispersion Characteristic and Plane Waves in DNG Medium

The dispersion characteristic or dispersion relation of a medium is the basic quantity which determines the propagation of electromagnetic waves in matter. This relation contains the information of the permittivity and permeability of the medium. This is due to the fact that they are the only parameters of the substances that appear in the dispersion equation [13]

$$\left| \frac{\omega^2}{c^2} \varepsilon_{ij} \mu_{ij} - k^2 \delta_{ij} + k_i k_j \right| = 0 \tag{2.1}$$

which gives the connection between the angular frequency ω of a monochromatic wave and its wave number k. In the case of an isotropic substance, Equation (2.1) takes simpler form as

$$k^2 = \frac{\omega^2}{c^2}n^2 \qquad (2.2)$$

where n^2 is the square of the refraction index of the substance and it is given by

$$n^2 = \varepsilon\mu \qquad (2.3)$$

where ε and μ are the permittivity and permeability of the substance. From Equation (2.2) and Equation (2.3), it can be said that a simultaneous change of the signs of permittivity ε and permeability μ has no effect on these relations [13]. However, DNG metamaterials with simultaneously negative permittivity and permeability have specific and unique electromagnetic properties that different from conventional materials. At this point, as it will be seen in the upcoming paragraph, it should be better to call the Maxwell equations and the constitutive relations to see what happens to the electromagnetic laws because of these negative parameters.

In a monochromatic plane wave, the electromagnetic field vectors $\boldsymbol{E}$ and $\boldsymbol{H}$ can be described as follows

$$\boldsymbol{E}(\boldsymbol{r}), \boldsymbol{H}(\boldsymbol{r}) \approx \exp(j\boldsymbol{k}\boldsymbol{r} - j\omega t). \qquad (2.4)$$

Let us write the Maxwell equations and see what they tell us

$$\nabla \times \boldsymbol{E}(\boldsymbol{r}) = -\frac{1}{c}\frac{\partial \boldsymbol{B}(\boldsymbol{r})}{\partial t} \qquad (2.5\text{a})$$

$$\nabla \times \boldsymbol{H}(\boldsymbol{r}) = \frac{1}{c}\frac{\partial \boldsymbol{D}(\boldsymbol{r})}{\partial t} \qquad (2.5\text{b})$$

and the constitutive relations

$$\boldsymbol{B}(\boldsymbol{r}) = \mu \boldsymbol{H}(\boldsymbol{r}) \qquad (2.6\text{a})$$

$$\boldsymbol{D}(\boldsymbol{r}) = \varepsilon \boldsymbol{E}(\boldsymbol{r}) \qquad (2.6\text{b})$$

where $\varepsilon = \varepsilon_r \varepsilon_o$ and $\mu = \mu_r \mu_o$. Substituting (2.4) into (2.5) and (2.6) gives

$$\boldsymbol{k} \times \boldsymbol{E}(\boldsymbol{r}) = \frac{\omega}{c}\mu \boldsymbol{H}(\boldsymbol{r}) \qquad (2.7\text{a})$$

$$\boldsymbol{k} \times \boldsymbol{H}(\boldsymbol{r}) = -\frac{\omega}{c}\varepsilon \boldsymbol{E}(\boldsymbol{r}). \qquad (2.7\text{b})$$

These are the main equations that carry all information about right-handed (conventional or standard) and left-handed (DNG metamaterials) materials. In conventional materials with both positive permittivity ε and positive permeability μ,

Equation (2.7) implies that the triad E, H, and k forms a right-handed system. But, if the permittivity ε and permeability μ are simultaneously negative, the triad E, H, and k forms a left-handed system. However, the time-average Poynting vector (average power density) is still

$$S(r) = \frac{1}{2}\Re\left\{E(r) \times H^*(r)\right\}$$

(2.8)

and it is independent of the signs and values of the permittivity ε and permeability μ. According to Equation (2.8), Poynting vector always forms a right-handed system with the vectors E and H. Also, Poynting vector S and the wave vector k are in the same direction for right-handed materials, and they are in opposite direction for DNG metamaterials. The left- and right-handed systems are shown in Figure 2.1.

(a)   (b)
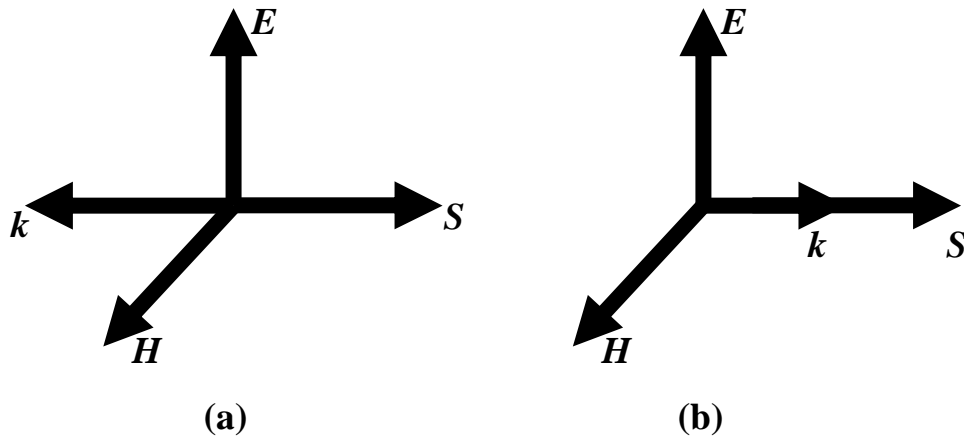
Figure 2.1: Configuration of the triad E, H, and k in (a) left-handed system, (b) right-handed system.

In addition, the wave vector k is in the direction of phase velocity; while the phase velocity and energy flux are in opposite direction in DNG metamaterials. Note

that, the group velocity is negative in DNG metamaterials. Because DNG metamaterials have negative group velocity, sometimes it is called as materials with negative group velocity. Furthermore, Poynting vector is always directed away from the source of the radiation. The wave vector k is directed away from the source for the right-handed materials, but it is towards the source for DNG metamaterials. This is the principal difference between the right-handed materials and DNG metamaterials.

2.3 Properties of DNG Media

In the pervious section, it is indicated that the direction of the phase velocity is opposite to the direction of power flow and to the group velocity in the DNG media. It can be said that there is anti-parallelism between the phase and group velocities and several phenomena connected to the phase of the wave are reversed in such media. Now, let us look at other changes that are not given in the previous section happened in DNG media.

• *Reversed Doppler Effect*: A detector of radiation moving in DNG medium will pursue fewer wave fronts if it is moving towards the source due to the reversal of the phase velocity. When $\Delta\omega > 0$, an observer will see a receding source. The red shift will occur under approaching conditions, and blue shift when the source and receiver more away. The experimental observation of the inverse Doppler shift in which the frequency of a wave is increased on reflecting from a receding boundary is reported in 2003 [6], [13], [67], [68].

• *Reversed Vavilov-Cerenkov Radiation*: The particle motion in a DNG medium generates backward power. The angle of the emission will change to concave. The emitted radiation propagates backwardly [13], [67], [68].

• *Goss-Hanchen Effect*: The lateral shift phenomenon can be negative in total internal reflection situation [6].

- *Lensing Effect*: Perfect and/or super lenses can be creatable with the use of DNG metamaterials. Convex (concave) DNG lenses are diverging (converging). [6], [45], [69–72].

- *Subwavelength Focusing*: Subwavelength focusing of an image can be achievable by flat DNG slab. Low spatial frequency features are focused by reversed Snell's law, while high spatial frequency features are enhanced due to the reversed transfer function associated with surface wave or plasmon excitation [6], [45], [69–72].

- *Reversed Snell's Law*: The reversed Snell's law which relates the incidence angles and refraction in materials is possible in DNG medium.

- *Negative Refractive Index*: The refractive index of a medium must be negative if the permittivity and permeability of the medium are simultaneously negative.

- *Backward Waves*: As mentioned before, the power vector is in the opposite direction to the wave vector k and the phase velocity in DNG media. Also, the vector E, H, and k form a left-handed system in these media. In this system, the power propagates in the opposite direction of k. Thus, the plane wave with the wave vector of k in DNG media is a backward wave [13], [73], [74].

- *Energy*: The simultaneously negative parameters (permittivity and permeability) can only be realized in frequency dispersive media. If the parameters are simultaneously negative, it should be better to review the equation of the energy. The common energy equation is given by

$$W = \varepsilon E^2 + \mu H^2 .$$
(2.9)

If there is neither frequency dispersion nor absorption, we can not have simultaneously negative parameters. When there is frequency dispersion, Equation (2.9) must be replaced by

$$W = \frac{\partial(\varepsilon\omega)}{\partial\omega}E^2 + \frac{\partial(\mu\omega)}{\partial\omega}H^2 .$$
(2.10)

For the energy to be positive, it is required that

$$\frac{\partial(\varepsilon\omega)}{\partial\omega} > 0$$
(2.10a)

$$\frac{\partial(\mu\omega)}{\partial\omega} > 0 .$$
(2.10b)

These inequalities do not mean that the parameters can not be simultaneously negative, but for them to hold it is necessary that the permittivity and permeability depend on the frequency [13].

2.4 Negative Refraction

DNG metamaterials have simultaneously negative permittivity and permeability as stated before. These stand in the third quadrant of the permittivity and permeability $(\varepsilon - \mu)$ diagram which is shown in Figure 2.2. As it is seen from the figure, there are four possibilities for sign of the pair (ε, μ) which are (+, +), (−, +), (−,−), and (+,−). Basically, the first combination is well known in conventional or right-handed materials and the third one corresponds to the new class of DNG metamaterials. For the other two combinations, there are only evanescent waves since one of the permittivity or permeability values is negative and the other is positive.

$$\mu$$

II

$\varepsilon < 0 \, , \, \mu > 0$

$n = j\sqrt{|\varepsilon|\mu} \in \mathfrak{I}$

plasmas

metals at optical frequencies

evanescent wave

I

$\varepsilon > 0 \, , \, \mu > 0$

$n = +\sqrt{\varepsilon\mu} \in \mathfrak{R}, n > 0$

isotropic dielectrics

right-handed (RH) /

forward-wave propagation

$$\varepsilon$$

III

$\varepsilon < 0 \, , \, \mu < 0$

$n = -\sqrt{|\varepsilon| \cdot |\mu|} \in \mathfrak{R}, n < 0$

DNG metamaterials

left-handed (LH) /

backward-wave propagation

IV

$\varepsilon > 0 \, , \, \mu < 0$

$n = j\sqrt{\varepsilon|\mu|} \in \mathfrak{I}$

ferrites

ferromagnetic materials

evanescent wave
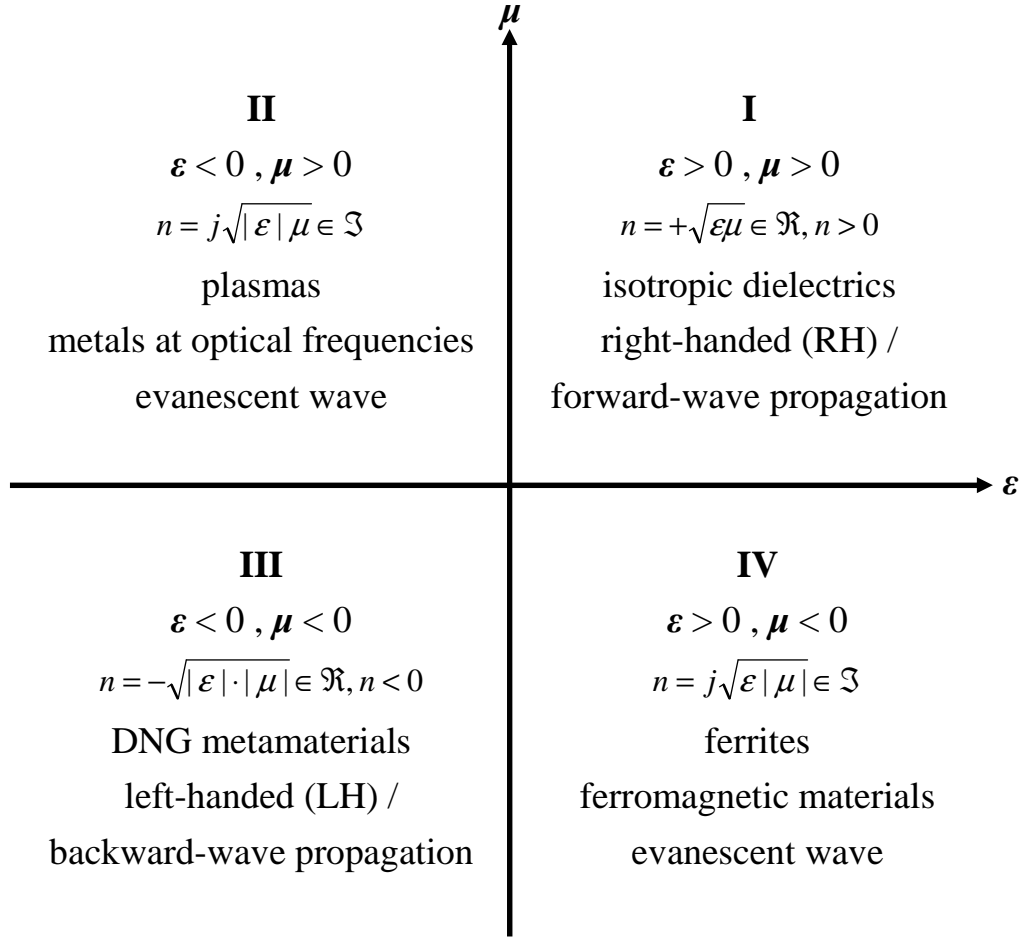
Figure 2.2: Permittivity and permeability ($\varepsilon - \mu$) diagram.

The refraction index is very significant parameter which is mentioned in Figure 2.2. The refraction index of a medium is defined as the ratio of the phase velocity of a wave in a reference medium to the velocity of the medium itself. In general, it can be written as

$$n(\omega) = \sqrt{\varepsilon_r(\omega)\mu_r(\omega)} \tag{2.11}$$

where $\varepsilon_r(\omega)$ and $\mu_r(\omega)$ are the frequency dependent relative permittivity and permeability, respectively. For DNG metamaterials, the frequency dependent relative permittivity and permeability are negative $\{\varepsilon_r(\omega) < 0$ and $\mu_r(\omega) < 0\}$ in a certain frequency band. Thus, we may write

$$\varepsilon_r(\omega) = |\varepsilon_r(\omega)| \cdot \exp(j\pi) \tag{2.12a}$$

$$\mu_r(\omega) = |\mu_r(\omega)| \cdot \exp(j\pi). \tag{2.12b}$$

Then Equation (2.11) becomes

$$
\begin{aligned}
n(\omega) &= \sqrt{|\varepsilon_r(\omega)\mu_r(\omega)| \cdot \exp(2j\pi)} \\
&= \sqrt{|\varepsilon_r(\omega)\mu_r(\omega)|} \cdot \exp(j\pi) \\
&= -\sqrt{|\varepsilon_r(\omega)\mu_r(\omega)|}
\end{aligned}
\tag{2.13}
$$

The refraction index n and its sign are important in the wave propagation. The sign of refraction index is positive in the conventional materials in which the relative permittivity and permeability are simultaneously positive. Eventually, we deal with the forward-wave propagation. But, in DNG metamaterials in which the relative permittivity and permeability are simultaneously negative, the sign of n is negative and thus there is backward-wave propagation. In the cases when one of the relative permittivity or the relative permeability is negative and the other is positive, the value of n is imaginary, so there is no wave propagation. The general sign rules are given in Table 2.1. The sign of the refraction index also plays an important role in the ray diagram. The ray diagram between two different media is given in Figure 2.3. Negative refraction can easily be observed from this figure. In addition, as it is mentioned before, the reversed Snell's law is possible in DNG metamaterials and it can be determined using Figure 2.3.

Table 2.1: The sign rules for the refraction index.

	$\varepsilon_r > 0$	$\varepsilon_r < 0$
$\mu_r > 0$	+	j
$\mu_r < 0$	j	–
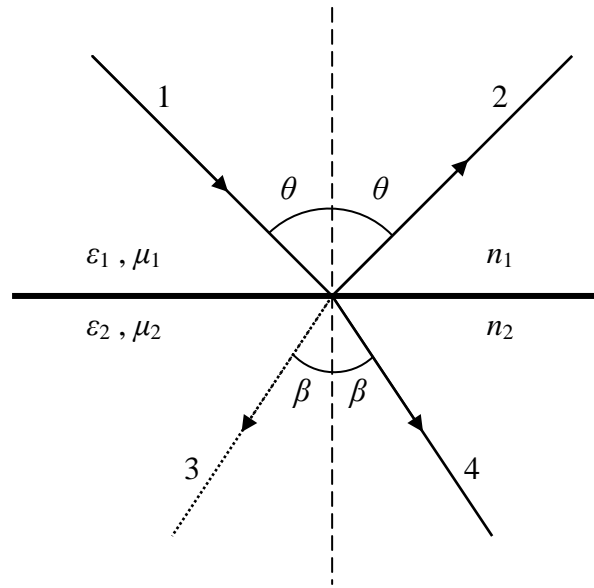
Figure 2.3: Passage of a ray through the boundary between two media, 1 – incident ray, 2 – reflected ray, 3 – refracted ray if the second medium is DNG metamaterial ($n_2 < 0$), 4 – refracted ray if the second medium is conventional medium ($n_2 > 0$).

The usual Snell's law can be written using Figure 2.3

$$\frac{\sin \theta}{\sin \beta} = n_{1,2} = \sqrt{\frac{\varepsilon_2 \mu_2}{\varepsilon_1 \mu_1}} \qquad (2.14)$$

where ε_1 and μ_1 are the permittivity and permeability of the first medium and ε_2 and μ_2 are the permittivity and permeability of the second medium, respectively. Equation (2.14) has to be given a more precise form if the rightnesses of both media are different. Thus, it can rewritten as follows

$$\frac{\sin \theta}{\sin \beta} = n_{1,2} = \frac{p_2}{p_1} \left| \sqrt{\frac{\varepsilon_2 \mu_2}{\varepsilon_1 \mu_1}} \right| \tag{2.15}$$

where p_1 and p_2 are the rightnesses of the first and second media. Note that, the medium is right-handed or conventional medium if $p_1 = +1$, and left-handed or DNG medium if $p_2 = -1$. It is obvious from Equation (2.15) that the refraction index of two media can be negative if the rightnesses of the media are different. In particular, the refraction index of DNG metamaterial relative to vacuum is negative. Furthermore, the negative refraction at the interface between two different media and the reversed Snell's law can be observed, and the comparison of refraction in a DNG metamaterial to that in a conventional material can be seen in Figure 2.4. It is clear that, Figure 2.4 is the basic verification of the reversed Snell's law.
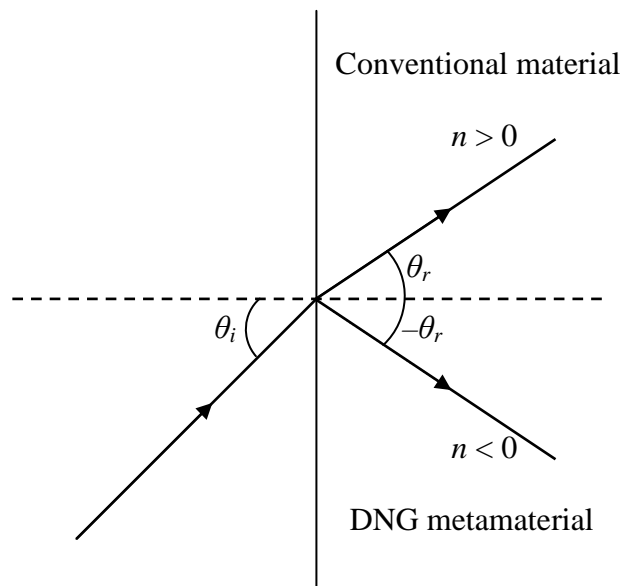
Figure 2.4: Negative refraction at the interface between two different media.

Moreover, it is a well-known and established rendering technique that calculates an image of a scene by simulating the way rays of light travel. It is called the ray tracing technique. An example, regarding reflection, is shown in Figure 2.5 [75]. The rod appears broken towards the left-hand side –the "wrong" side – for a negative index when looking at the side of the glass. Note that the rod appears broken towards the rear if one directly looks at the air-"water" interface in (c) because rays traveling from the under-"water" part of the rod towards the rear are negatively refracted at this interface towards the observer [76].

(a) (b) (c)
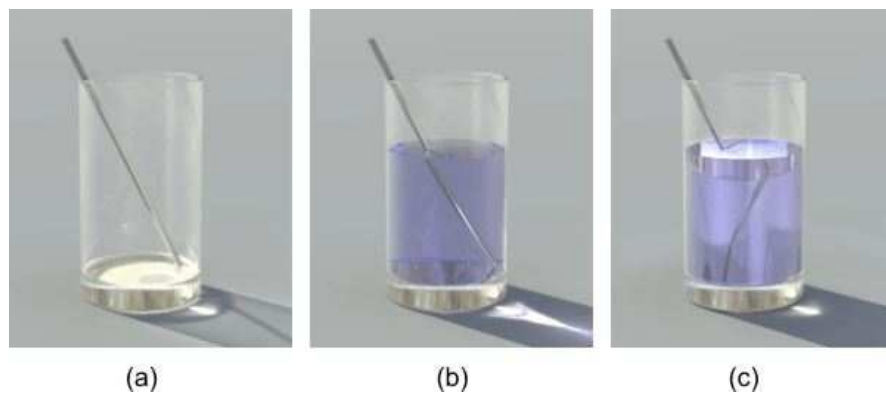
Figure 2.5: (a) Calculated ray tracing image of a metal rod in an empty drinking glass. (b) Same scenery, but the glass is filled with normal water, leading to leading to ordinary refraction. (c) The water is replaced by "water" with a fictitious refractive index.

2.5 Summary and Discussion

In this chapter, the fundamentals of DNG metamaterials are reviewed and examined. The dispersion characteristic of this medium is firstly given and dispersion equation is determined. Secondly, plane waves in these media are examined. Left-handed system and the relation between the wave numbers and powers in such media are illustrated. Then, the unusual and extraordinary features of DNG metamaterials are discussed. Reversed Doppler Effect, reversed Vavilov-Cerenkov radiation, Goss-Hanchen effect, lensing effect, subwavelength focusing, reversed Snell's law, negative refractive index, backward waves, and the situation of the energy in DNG metamaterials are mentioned. Then, the phenomenon of negative refraction is studied in detail. In this way, the basics of DNG metamaterials are review and the DNG phenomenon are described. All of these works will be useful and they can provide to easily understand the concept of DNG metamaterials especially in the following chapters.

CHAPTER 3

CHARACTERIZATION AND REALIZATION OF DOUBLE NEGATIVE METAMATERIALS

3.1 Introduction

The characterization and realization of DNG metamaterials are very important because the physical models of DNG metamaterials are designed and created in the base of these descriptions. For this reason, it will be tried to investigate how the DNG metamaterials are formed. In this research, DNG metamaterials are described using analytical/theoretical and physical/practical models. Hypothetical, Lorentz, Drude, and cold plasma medium models are explained to produce DNG metamaterials in the analytical models. Basic properties of these medium models are given in detail and some numerical examples are also provided to illustrate the features of them. After that, physical models and their properties are explained. Furthermore, the relation between the analytical and physical models is also studied throughout this chapter.

3.2 Analytical Models

From the past to the present, DNG metamaterials were characterized by many models consisting of non-dispersive and dispersive media. Here, some DNG metamaterial models and their basic properties will be discussed.

3.2.1 Hypothetical DNG Medium Model

Hypothetical DNG medium is the theoretical medium with both negative isotropic dielectric permittivity and permeability, firstly suggested and investigated by Veselago in 1967. Basically, this medium is a non-dispersive medium and the material parameters (permittivity and permeability) can be selected directly from negative values such as $\varepsilon = -4\varepsilon_o$ and $\mu = -2\mu_o$. For this selection, the refraction index n can be calculated from Equation (2.13) as $n = -2.8284$. In addition, the wave number k becomes $k = k_o n = -2.8284k_o$ where k_o is the free space wave number.

3.2.2 Lorentz Medium Model

Lorentz medium is a frequency dispersive medium in which the permittivity and permeability of the material are the function of the frequency. These materials have resonance phenomena caused by the oscillation of the electron and nuclei subject to an applied field. Lorentz was the first to study such phenomena when developing the theory of the electron. The model conceptually replaces the atoms and molecules of a real material by a set of harmonically bound electron oscillators, resonant at some frequency ω_o. At frequencies far below ω_o, an applied electric field displaces the electrons from the positive core, inducing a polarization in the same direction as the applied electric field. At frequencies near the resonance, the induced polarization becomes very large, as is typically the case in resonance phenomena; the large response represents accumulation of energy over many cycles, such that a considerable amount of energy is stored in the medium relative to the driving field. So large is this stored energy that even changing the sign of the applied electric field has little effect on the polarization near resonance! That is, as the frequency of the driving electric field is swept through the resonance, the polarization flips from in-phase to out-of-phase with the driving field and the material exhibits a negative response. If instead of electrons the material response were due to harmonically bound magnetic moments, then a negative magnetic response would exist. Though

24

somewhat less common than positive materials, negative materials are nevertheless easy to find. Materials with ε negative include metals (e.g., silver, gold, aluminum) at optical frequencies, while materials with μ negative include resonant ferromagnetic or antiferromagnetic systems [77, 78]. As a result, the shape of the dispersive components of the material parameters for DNG metamaterial can be described by using Lorentz medium model.

The generalized permittivity and permeability of this medium can be expressed as [77] (see also [2, 36–38, 78–82])

$$\varepsilon(f) = \varepsilon_o \left(1 - \frac{f_{ep}^2 - f_{eo}^2}{f^2 - f_{eo}^2 + j\delta_e f} \right) \tag{3.1}$$

$$\mu(f) = \mu_o \left(1 - \frac{f_{mp}^2 - f_{mo}^2}{f^2 - f_{mo}^2 + j\delta_m f} \right) \tag{3.2}$$

where f_{ep}, f_{mp} are the electric and magnetic plasma frequencies, f_{eo}, f_{mo} are the electric and magnetic resonance frequencies, and δ_e, δ_m are the electric and magnetic damping frequencies, respectively. As it can be predicted from Equation (3.1) and Equation (3.2), the permittivity and permeability of Lorentz medium can be simultaneously negative over a certain frequency band. In light of Equation (3.1) and Equation (3.2), some numerical examples are prepared to see and understand how the material parameters (ε and μ) of Lorentz medium work. For simplicity, $f_{ep} = f_{mp} = f_p$, $f_{eo} = f_{mo} = f_o$, and $\delta_e = \delta_m = \delta$ are selected to obtain the same response for the permittivity and permeability. The following values are considered: $f_p = 20$ GHz, $f_o = 5$ GHz, and $\delta = 0, 0.1, 1, 10, 100$ GHz. Figure 3.1 shows the relative permittivity and permeability of Lorentz medium when the damping frequencies change. According to the theory of electrodynamics, the real parts of the permittivity and permeability

are negative while the imaginary parts of them are positive for DNG medium. This condition is satisfied for all numerical results obtained here. There is no imaginary part for the permittivity and permeability when the damping frequency is zero. This means that the medium is the lossless Lorentz medium. Also, the negative band for the permittivity and permeability is narrow in Lorentz medium model. In addition, from the results obtained, the width of negative band is directly proportional with increasing the damping frequency. In addition, we also see that if damping frequency δ is very large, the plasma effect will completely disappear. Furthermore, the negative region occurs between the plasma and resonance frequencies.
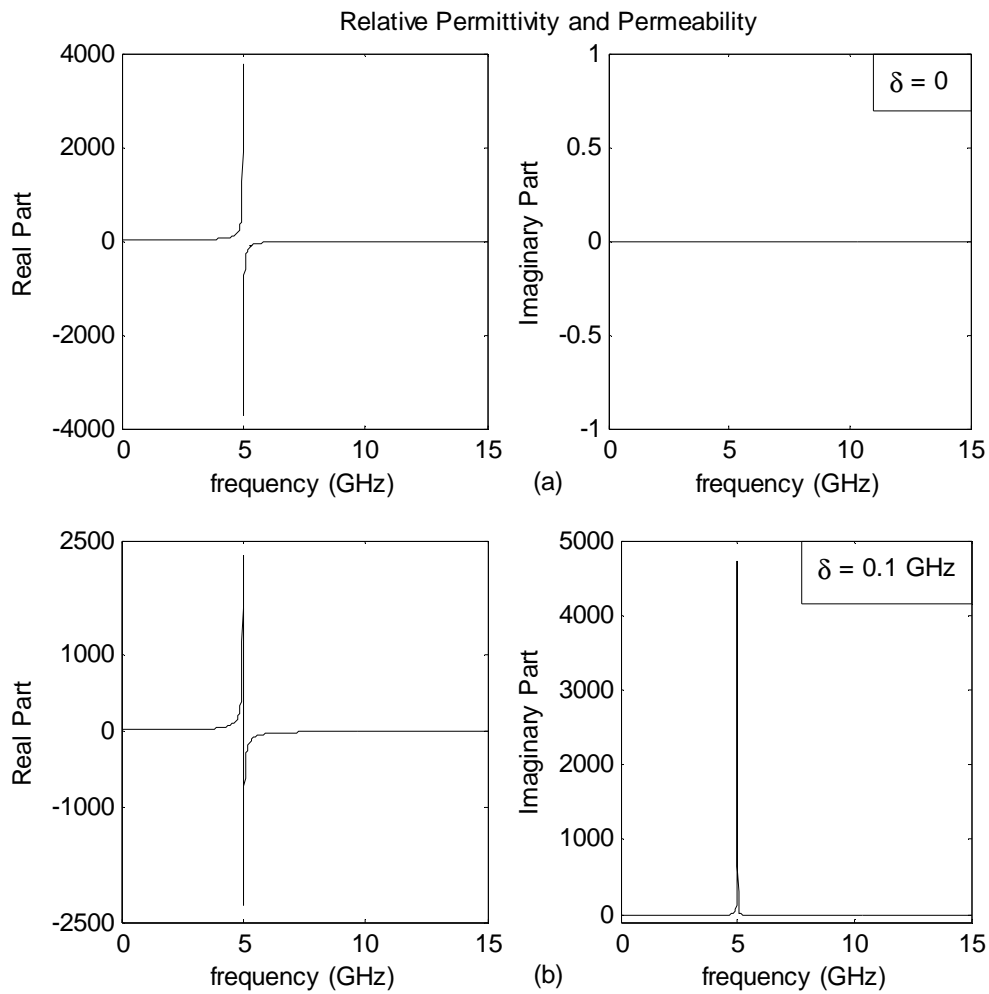
Figure 3.1: Relative permittivity and permeability of Lorentz medium for different damping frequencies.
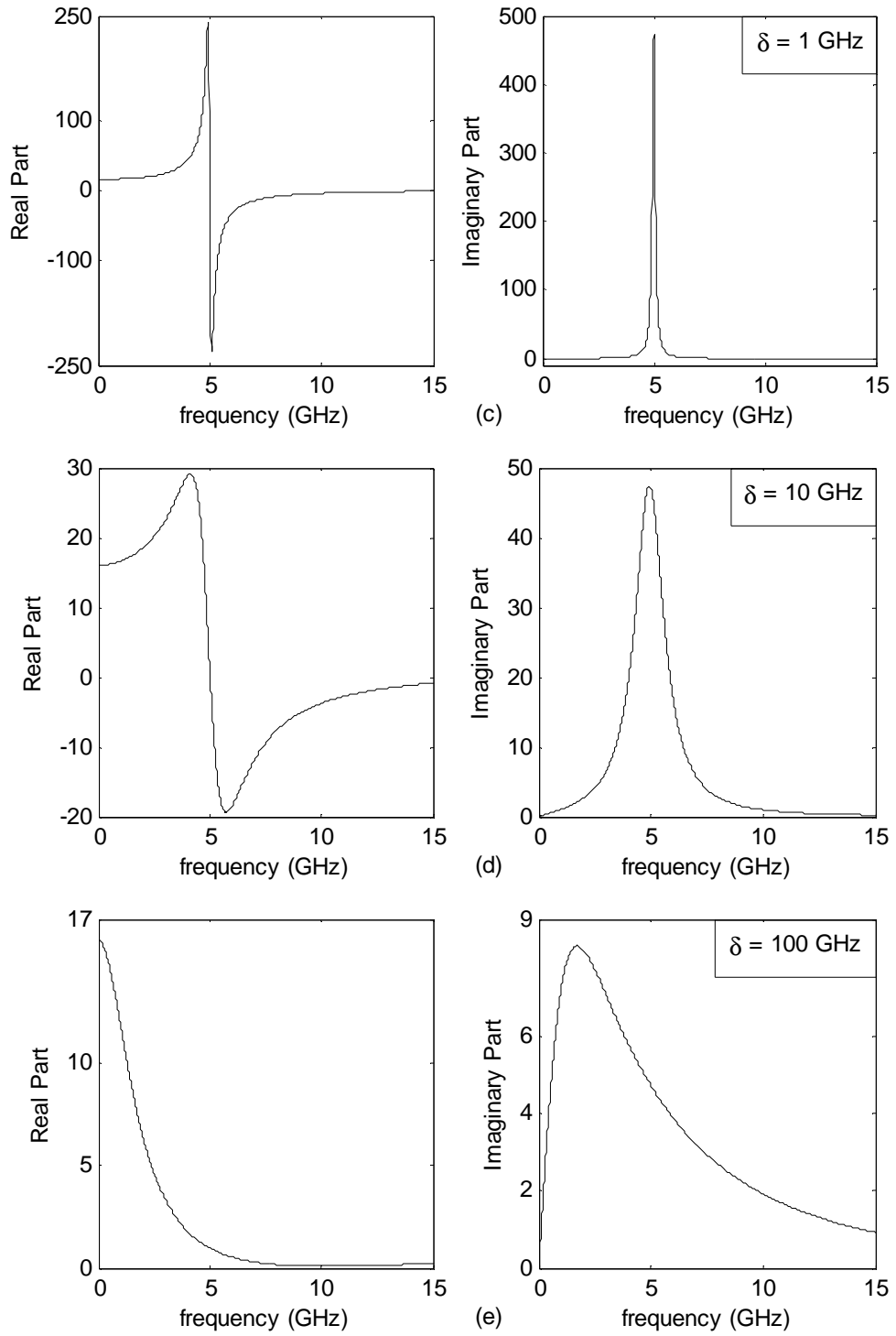
Figure 3.1: (continue) Relative permittivity and permeability of Lorentz medium for different damping frequencies.
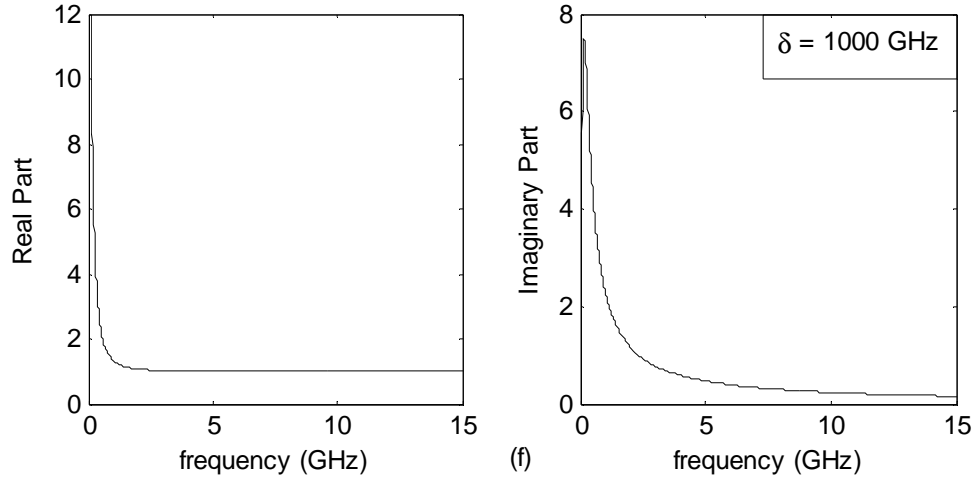
Figure 3.1: (continue) Relative permittivity and permeability of Lorentz medium versus frequency for different damping frequencies.

3.2.3 Drude Medium Model

Drude medium model is simply a special case of the Lorentz medium model in which the electric and magnetic resonance frequencies are zero, $f_{eo} = f_{mo} = 0$. This model is used in many studies such as those reported in [35], [41], [78], [80], [83], and [84]. Generally, this model can be used to describe the collective oscillation of free electrons in metallic materials. The frequency dependent permittivity and permeability of the medium can be easily determined from Equation (3.1) and Equation (3.2) as

$$\varepsilon(f) = \varepsilon_o \left(1 - \frac{f_{ep}^2}{f^2 + j\delta_e f} \right) \tag{3.3}$$

$$\mu(f) = \mu_o \left(1 - \frac{f_{mp}^2}{f^2 + j\delta_m f} \right) \tag{3.4}$$

Note that, the simultaneously negative frequency band for the permittivity and permeability is not narrow as in the previous model. Here, this band is wider than the band of the Lorentz medium model as it can be observed from the material parameters ε and μ. Some examples are presented numerically to observe this band. Plasma and damping frequencies are selected to be equal each other for simplicity ($f_{ep} = f_{mp} = f_p$, and $\delta_e = \delta_m = \delta$). The frequencies are selected as: $f_p = 20$ GHz and $\delta = 0, 1, 100$ GHz. Figure 3.2 presents the relative permittivity and permeability of Drude medium against the frequency when the damping frequencies change. The requirements of DNG medium, Re(ε) < 0, Re(μ) < 0, Im(ε) > 0, and Im(μ) > 0, are again fulfilled in all numerical results. Lossless Drude medium, Im(ε)= 0, and Im(μ) = 0, is obtained when $\delta = 0$. Negative band for the permittivity and permeability is wide in Drude medium model. The width of negative band is not more affected from the damping frequency except its high values such as 100 GHz. In addition, the imaginary parts of the permittivity and permeability can be negligible at high frequencies. Comparing Lorentz and Drude models it can be seen that Drude model has wider negative band than Lorentz model. This negative band is more easily arranged in Drude model. Also, the damping frequency in Lorentz model has a significant effect while managing the negative permittivity and permeability. In turn, it has not such a significant effect in Drude model.
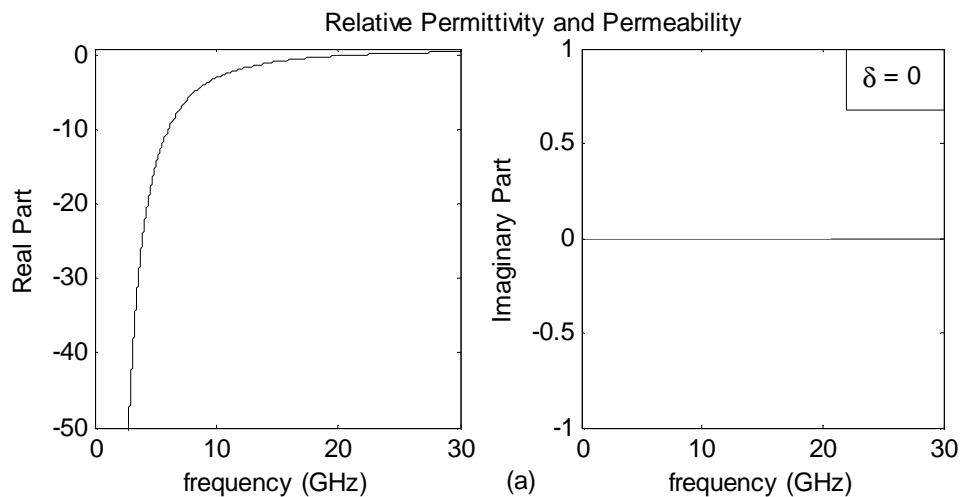
Figure 3.2: Relative permittivity and permeability of Drude medium against the frequency for different damping frequencies.
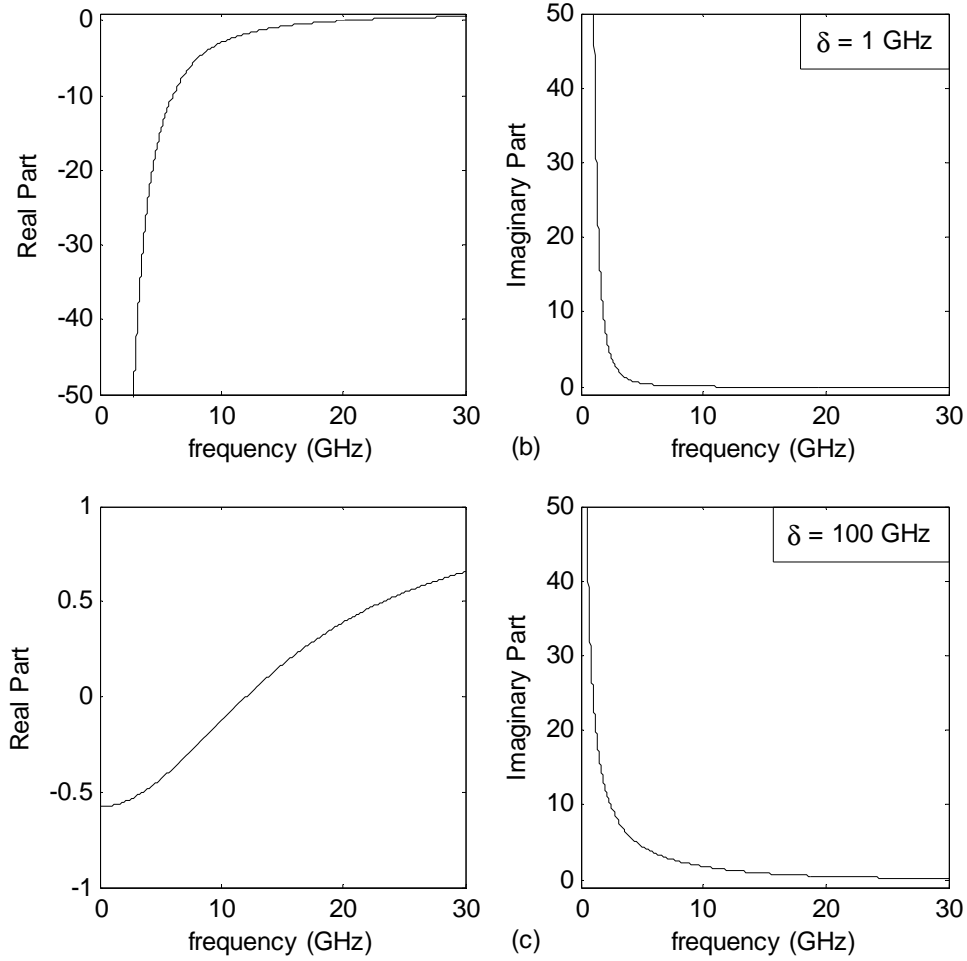
Figure 3.2: (continue) Relative permittivity and permeability of Drude medium against the frequency for different damping frequencies.

3.2.4 Cold Plasma Medium Model

Another frequency dispersive medium is the cold plasma medium which has Lorentz type dispersion (k-ω relation) relation. This model has also frequency dependent material properties $\varepsilon(f)$ and $\mu(f)$. The cold plasma medium model can be obtained from the Drude medium model when the electric and magnetic damping frequencies are set to be zero, $\delta_e = \delta_m = 0$. Thus, the Drude medium will reduce to cold plasma medium as [45, 80, 85–87]:

$$\varepsilon(f) = \varepsilon_o \left(1 - \frac{f_{ep}^2}{f^2} \right)$$ (3.5)

$$\mu(f) = \mu_o \left(1 - \frac{f_{mp}^2}{f^2} \right)$$ (3.6)

Note that, the cold plasma medium model parameters have pure lossless material parameters ε and μ which means the frequency dispersive and lossless DNG metamaterials can be characterized using these parameters. This is the main difference among the other models. Numerical examples for cold plasma model are provided when $f_{ep} = f_{mp} = f_p$. The following values are considered: $f_p = 1$, 10, 30, and 50 GHz. Figure 3.3 displays the relative permittivity and permeability of the cold plasma medium for various f_p. The negative band for the permittivity and permeability in the cold plasma model is widest among the other models. Also, this band is more easily managed in this model than the others.
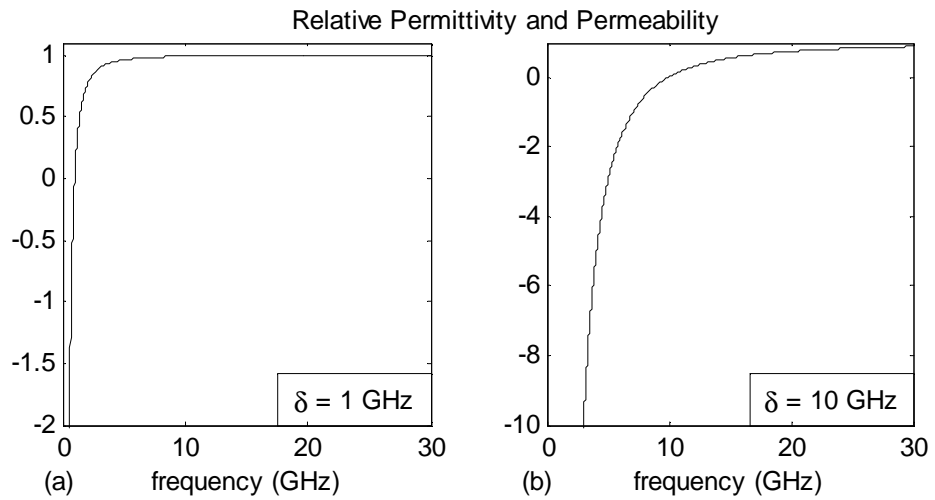
Figure 3.3: Relative permittivity and permeability of the cold plasma medium as a function of the frequency for various plasma frequencies.
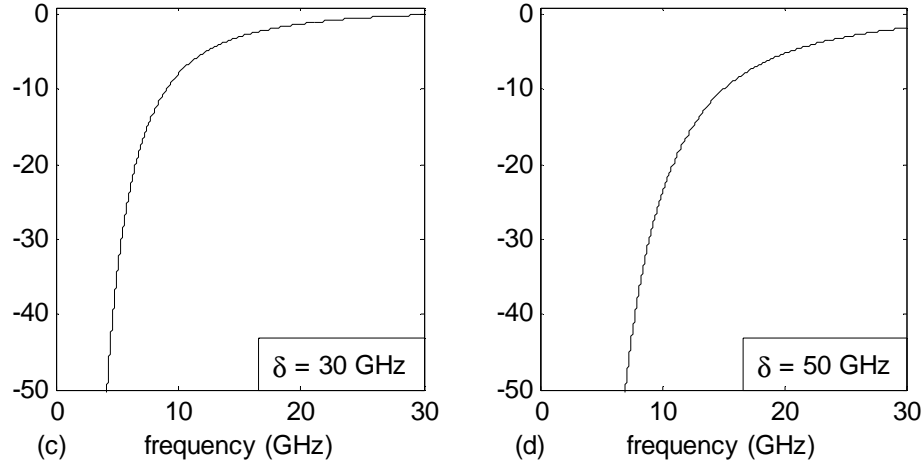
Figure 3.3: (continue) Relative permittivity and permeability of the cold plasma medium as a function of the frequency for various plasma frequencies.

3.3 Physical Models

Nowadays, the realization of DNG metamaterial in the macroscopic view is achievable and feasible by replacing the succession of metallic rings and rods (wire strips) in a homogeneous host medium. This approach is possible since the rings and the separations between the rods are very small compared to the operation wavelength. In this approach, metallic rods are used to provide negative permittivity and metallic rings for negative permeability. The studies of the negative permittivity due to the metallic rods and the negative permeability due to the metallic split rings respectively can be found in Pendry's works [35, 36]. Then, the combination of rods and rings was firstly presented by Smith *et al*. [37]. The first metamaterial realized by Smith and his group is shown in Figure 3.4. The first metamaterial consist of periodic metallic rods and circular split rings in a host medium.

Figure 3.4: First metamaterial comprised of metallic rods and circular split rings.

After the first metamaterial, several methods and very advanced technological facilities to generate new types of metamaterials have been developed by many research groups. Especially, design of split rings based on the shape and geometry has been gained importance day by day in recent years. Numerous types of different ring and ring-like structures such as circular, square, Ω-shaped, U-shaped, S-shaped and etc. are used to produce new metamaterials. In the light of the known structures, triangular split rings are proposed in this thesis which is not studied yet. These will be discussed in the subsequent chapters. Note that, from the simulations and measurements, the permittivity and permeability of the physical metamaterials were shown to obey a Drude model and a Lorentz model, respectively. As in explained in the previous sections, the permittivity of Drude medium has wide negative band and its imaginary part can be negligible at high frequencies. But, the negative region occurs between the plasma and resonance frequencies for the permeability of Lorentz medium. This region is not wide as in Drude medium. In practice, the mentioned frequencies and the negative band are depend on the shape, geometry, size, class of the metallization and host medium, and many other factors. Detail explanation for the behavior of the permittivity of Drude medium and the permeability Lorentz medium can be found in Sections 3.2.2 and 3.2.3. Now, it will be better to give some examples numerically for the refractive index of physical metamaterials. These examples are not exact response for the refractive index of physical metamaterials. These are approximate examples to understand the estimated behavior of the

refractive index of them. Note that, the refractive index is calculated from the equation of $n = \sqrt{\varepsilon_r \mu_r}$ using the theory explained in Chapter 2.

In the first example, the effect of the damping frequency on the refractive index is investigated. It provides to conclude the loss effect of metamaterial structure due to the metallization and host medium. The theoretical curves for the refractive index are calculated using the following parameters: $f_{ep} = 18$ GHz, $f_{mp} = 15$ GHz, $f_{mo} = 12$ GHz [88], and $\delta_e = \delta_m = \delta = 0.5$, 5, and 10 GHz. Figure 3.5 shows the refractive index, n, as a function of the frequency when the damping frequency changes. As it is seen from the figure, negative band occurs between the magnetic resonance frequency and magnetic plasma frequency (12 GHz and 15 GHz). This means that the permeability is more effective than the permittivity in the computation of negative region. In practice, the metallic split rings play the main roles when the negative frequency band formed. In addition, the real part of the refractive index, Re(n), is zero before 12 GHz ($f < f_{mo}$) and between 15 GHz and 18 GHz ($f_{mp} < f < f_{ep}$). Also, it is positive after 18 GHz ($f_{ep} < f$). The imaginary part of the refractive index, Im(n), is positive before 18 GHz ($f < f_{ep}$) and it is zero after 18 GHz ($f_{ep} < f$). Furthermore, from Figure 3.5(a), Im(n) is zero in the negative band when the damping frequency is small enough. In practice, the refractive index of the feasible metamaterials generally has the following form:

$$\text{Re}(n) \begin{cases} < 0 & f_{mo} < f < f_{mp} \\ = 0 & f < f_{mo} \ \text{ and } \ f_{mp} < f < f_{ep} \\ > 0 & f > f_{ep} \end{cases} \tag{3.7}$$

$$\text{Im}(n) \begin{cases} > 0 & f < f_{ep} \\ = 0 & f > f_{ep} \end{cases}. \tag{3.8}$$

Moreover, when the damping frequency is high, the negative band deforms and metamaterial structure does not work well in the negative region. Thus, the damping frequency must be chosen carefully in the numerical calculations. Physically, the damping frequency represents the electric and magnetic losses which are included in the metallization and host medium. So, the metallization and host medium must be selected carefully to make the metamaterials. This is very important in the design, realization, and fabrication of them. Thus, it can be said that the results obtained here is very useful in the manufacturing process when choosing the metallization and host medium.

In the second example, the refractive index is computed for the various plasma, resonant, and damping frequencies different than the previous example. The computed results are presented in Figure 3.6. The following parameters are used:

$f_{ep} = 12.8$ GHz, $f_{mp} = 10.95$ GHz, $f_{mo} = 10.05$ GHz, and $\delta_e = \delta_m = \delta = 10$ MHz [38] for Figure 3.6(a);

$f_{ep} = 12$ GHz, $f_{mp} = 12$ GHz, $f_{mo} = 10$ GHz, and $\delta_e = \delta_m = \delta = 100$ MHz [80] for Figure 3.6(b); and

$f_{ep} = 20$ GHz, $f_{mp} = 7$ GHz, $f_{mo} = 25$ GHz, and $\delta_e = \delta_m = \delta = 1$ GHz for Figure 3.6(c).

As it seen from Figure 3.6(a) and Figure 3.6(c), frequency response of the refractive index satisfies the conditions given in the equations (3.7) and (3.8). In Figure 3.6(b), the imaginary part of refractive index is zero after f_{mo} (10 GHz) and it is greater than zero before this frequency. The real part of it is zero before f_{mo} (10 GHz), it is negative between f_{mo} (10 GHz) and f_{mp} (12 GHz), and it is positive after f_{mp} since the electric and magnetic plasma frequencies are equal each other. The bandwidth of the negative region in Figure 3.6(c) is wider than the others. The results show that for well designed metamaterials, it is necessary to know the effect of the shape, geometry, size, class of the metallization and host medium of the structure.
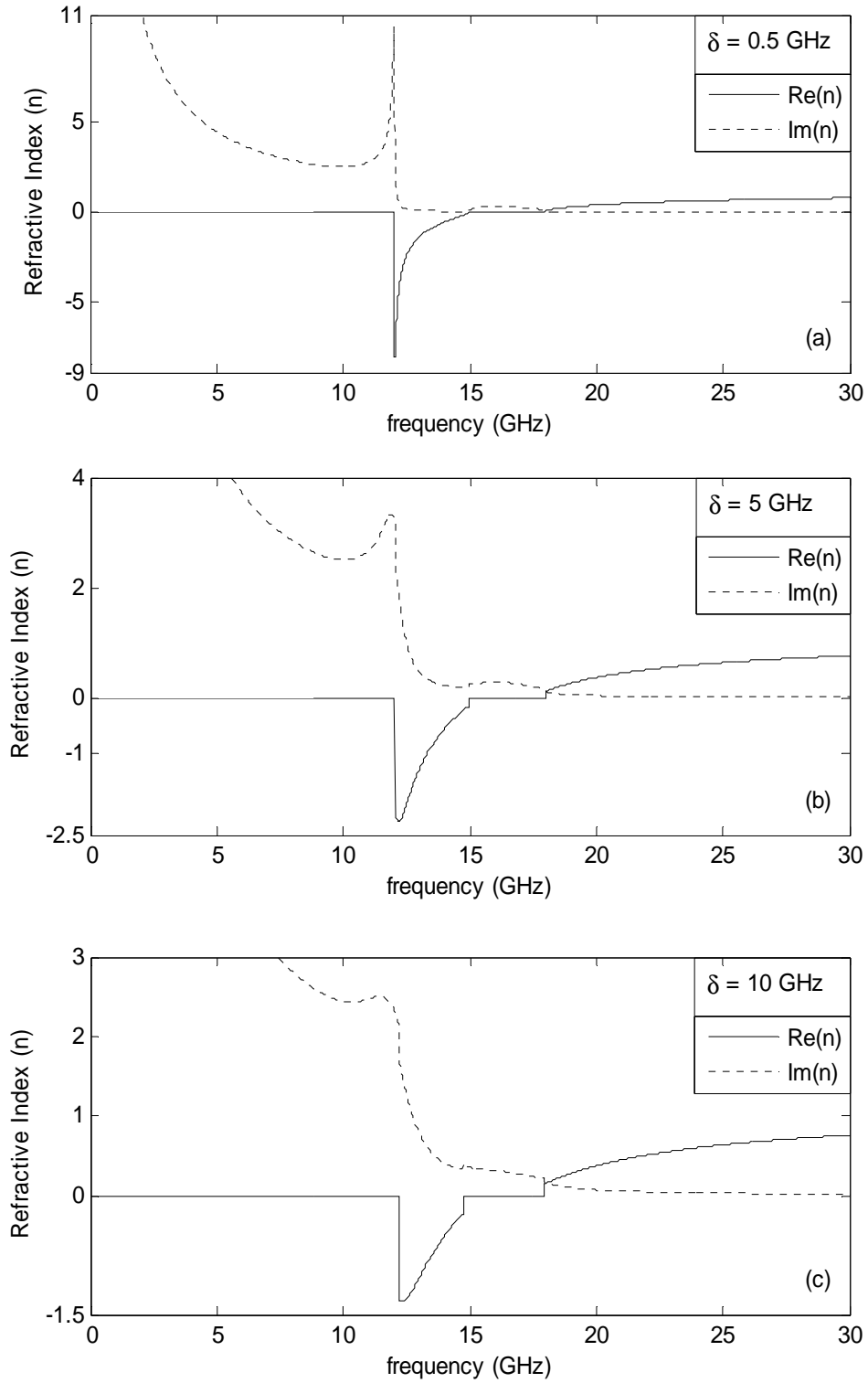
Figure 3.5: Real and imaginary parts of the refractive index, *n*, as a function of the frequency for different damping frequencies. f_{ep} = 18 GHz, f_{mp} = 15 GHz, f_{mo} = 12 GHz, and $\delta_e = \delta_m = \delta$.
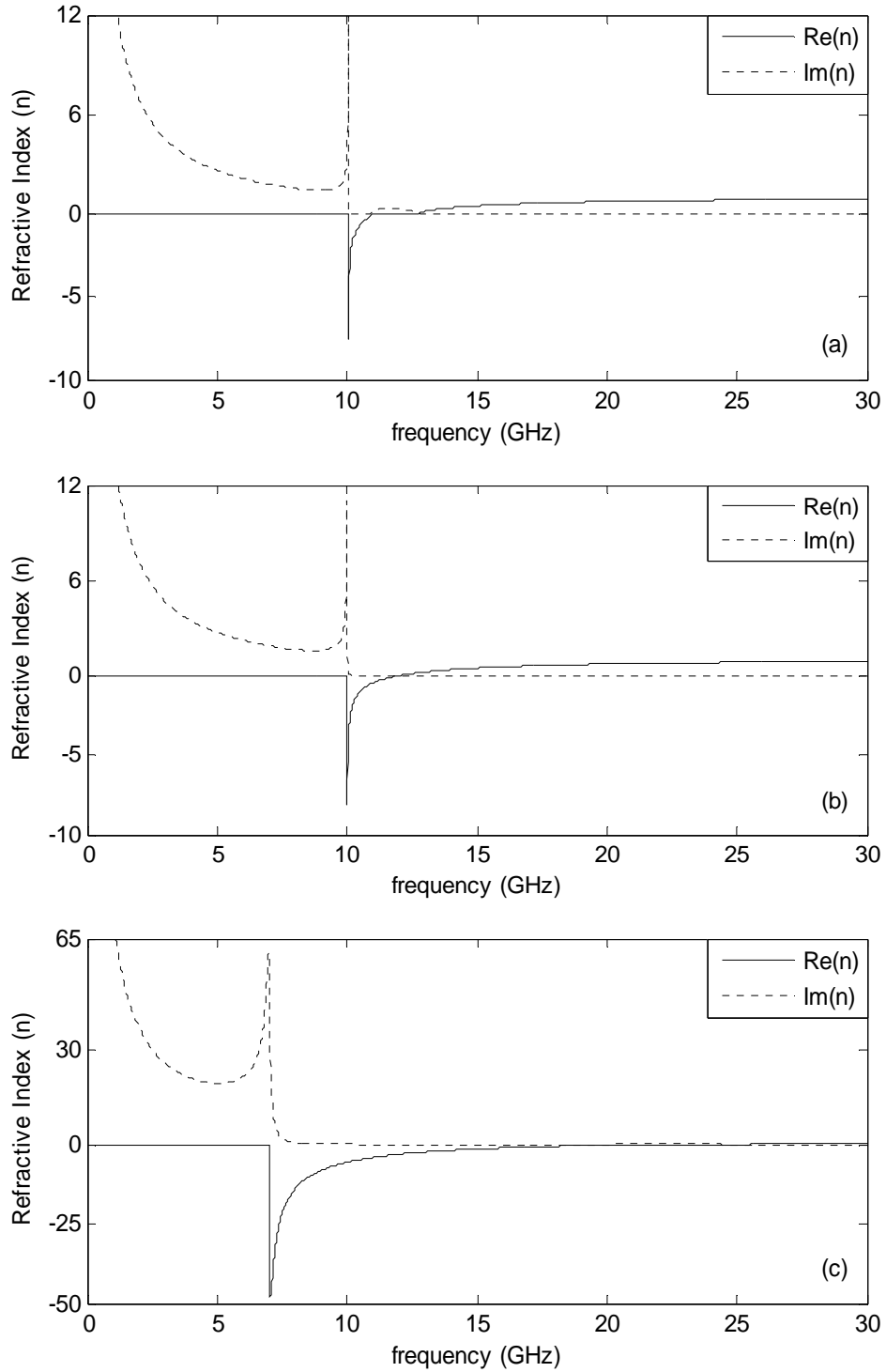
Figure 3.6: Real and imaginary parts of the refractive index, n, against the frequency. (a) $f_{ep} = 12.8$ GHz, $f_{mp} = 10.95$ GHz, $f_{mo} = 10.05$ GHz, and $\delta_e = \delta_m = \delta = 10$ MHz; (b) $f_{ep} = 12$ GHz, $f_{mp} = 12$ GHz, $f_{mo} = 10$ GHz, and $\delta_e = \delta_m = \delta = 100$ MHz; (c) $f_{ep} = 20$ GHz, $f_{mp} = 7$ GHz, $f_{mo} = 25$ GHz, and $\delta_e = \delta_m = \delta = 1$ GHz.

3.4 Summary and Discussion

The work in this chapter involved the modeling DNG metamaterials associated with the analytical and physical models. First of all, DNG metamaterials are defined using the theoretical formulations given in the analytical models. In these models, hypothetical, Lorentz, Drude, and cold plasma media are used to define DNG metamaterials. Basic properties of the mentioned medium models are given and then DNG metamaterials are constructed using them. The permittivity and permeability of each medium model and their characteristics are explained. Then, physical models of DNG metamaterials are clarified and the main features of them are presented. The behavior of the permittivity and permeability of the physical DNG metamaterials are illustrated. The relationship between the analytical and physical models is also mentioned. In addition, numerical results are provided to show the characteristics of the models. After detail investigation, the characterization and realization of the analytical and physical DNG metamaterials are deduced. This is very important because the design and manufacturing processes are based on these aspects. So that, these work will provide some views to understand how DNG metamaterials can be created analytically and physically. Consequently, all results obtained here can be used in the design and fabrication processes to create new DNG metamaterials.

CHAPTER 4

WAVE PROPAGATION IN DOUBLE NEGATIVE METAMATERIALS

4.1 Introduction

In this chapter, electromagnetic wave propagation through the DNG metamaterial will be discussed. Reflection and transmission coefficients will be derived to account for the reflected and transmitted fields by the boundary. Normal and oblique incidence cases will be considered and detail investigation for the monochromatic incident plane wave will be given. The effect of the structure parameters on the reflection and transmission will be pointed out. Then, the slab of DNG metamaterial embedded between two different semi infinite dielectric media will be constructed and examined. The reflection and transmission coefficients; and the reflected, transmitted, and loss powers will be derived for the DNG metamaterial slab. After that, DNG slab will be characterized by the four medium models explained in the previous chapter to find the scattering characteristics of it. Some numerical examples will also be provided to show these characteristics. All numerical examples are verified and validated using transmission line modeling method (TLM) which will be explained in Appendix. In addition, some simulation will also be given to show the application of the DNG metamaterial. Especially, the applications of flat lens and parabolic wave refractor will be presented in these simulations.

4.2 The Case of Normal Incidence

In this section, the reflection and transmission for the monochromatic plane wave with normal incidence on a semi infinite DNG metamaterial will be discussed. In the analysis, the standard procedure will be followed to obtain the reflection and transmission coefficients. First of all, two planar boundaries of double positive (DPS) and DNG media are considered by assuming the incident wave is traveling from the DPS medium to the DNG metamaterial. Here, DPS medium represents the conventional dielectric material. The incident wave is assumed to be perpendicular (normal incidence) to the planar interface formed by two semi infinite media. The geometry of the problem is illustrated in Figure 4.1. In the figure, E, H, and k stand for the electric field, the magnetic field, and the wave number of the related media. Also, ε_i and μ_i (ε_t and μ_t) represent the permittivity and permeability of DPS medium (DNG metamaterial).
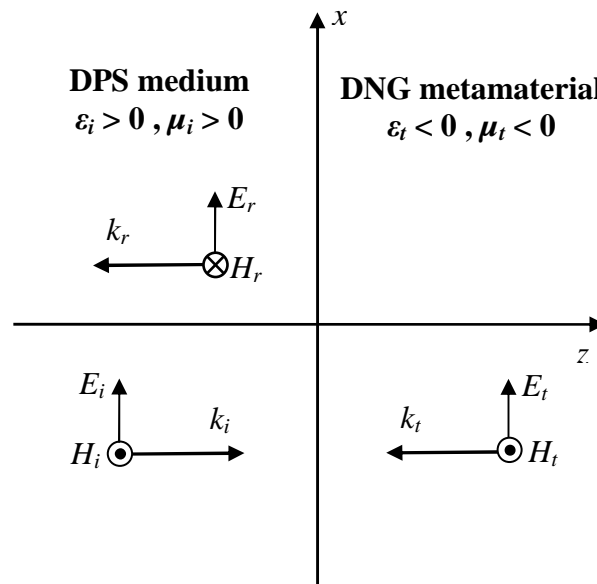
Figure 4.1: Reflection and transmission at normal incidence by two planar semi infinite DPS and DNG media.

Therefore, the incident electric and magnetic fields with the wave number k_i $(=\omega\sqrt{\mu_i\varepsilon_i}$) can be written as follows:

$$\boldsymbol{E_i} = \boldsymbol{a}_x\, E_i \cdot \exp(-jk_i\, z) \tag{4.1a}$$

$$\boldsymbol{H_i} = \boldsymbol{a}_y\, \frac{k_i}{\omega\mu_i}\, E_i \cdot \exp(-jk_i\, z) \tag{4.1b}$$

where E_i is the amplitude of the incident electric field. Note that, $\exp(j\omega t)$ is assumed time dependence and it is suppressed throughout this work. The reflected electric and magnetic fields can be expressed as:

$$\boldsymbol{E_r} = \boldsymbol{a}_x\, E_r \cdot \exp(jk_i\, z) \tag{4.2a}$$

$$\boldsymbol{H_r} = -\boldsymbol{a}_y\, \frac{k_i}{\omega\mu_i}\, E_r \cdot \exp(jk_i\, z) \tag{4.2b}$$

where E_r is the amplitude of the reflected electric field. In the transmitted medium (DNG metamaterial), the transmitted electric and magnetic fields are:

$$\boldsymbol{E_t} = \boldsymbol{a}_x\, E_t \cdot \exp(jk_t\, z) \tag{4.3a}$$

$$\boldsymbol{H_t} = \boldsymbol{a}_y\, \frac{k_t}{\omega\mu_t}\, E_t \cdot \exp(jk_t\, z) \tag{4.3b}$$

41

where E_t is the amplitude of the transmitted electric field and k_t is the wave number of DNG metamaterial.

The reflection and transmission coefficients will now be determined by enforcing continuity of the tangential components of the electric and magnetic fields across the interface. This continuity at the interface of $z = 0$ leads to

$$E_i + E_r = E_t \qquad (4.4a)$$

$$\frac{k_i}{\omega\mu_i}(E_i - E_r) = \frac{k_t}{\omega\mu_t} E_t . \qquad (4.4b)$$

In electromagnetics, the reflection (transmission) coefficient is defined as the ratio of the amplitude of the reflected (transmitted) field to the amplitude of the incident field. Solving Equation (4.4a) and Equation (4.4b) together using the definition of the reflection and transmission coefficients, we can write that

$$R = \frac{k_i\mu_t - k_t\mu_i}{k_i\mu_t + k_t\mu_i} \qquad (4.5a)$$

$$T = \frac{2k_i\mu_t}{k_i\mu_t + k_t\mu_i} . \qquad (4.5b)$$

Therefore, the plane wave reflection (R) and transmission (T) coefficients are functions of the constitutive properties, and they are given by Equation (4.5a) and Equation (4.5b).

Plots of the magnitude of reflection and transmission coefficients versus relative permittivity of hypothetical DNG medium are presented in Figure 4.2. Here, DPS and DNG media shown in Figure 4.1 are assumed to be free space and hypothetical DNG metamaterial, respectively. Note that, the hypothetical DNG medium model is explained in the previous chapter. The following values are used in the computations: $\varepsilon_i = \varepsilon_o$ and $\mu_i = \mu_o$ for free space, $\mu_t = -\mu_o$ for the hypothetical DNG metamaterial for Figure 4.2(a), and $\mu_t = -5\mu_o$ for the hypothetical DNG metamaterial for Figure 4.2(b). It is observed in Figure 4.2 that there is a relative permittivity where the reflection coefficient vanishes and the transmission coefficient reduces to unity. The magnitude of reflection coefficient decreases whereas that of the magnitude of transmission coefficient increases up to this relative permittivity of the hypothetical DNG metamaterial. After this value, the magnitude of reflection coefficient increases while the magnitude of transmission coefficient decreases. As it is well known that reflection coefficient becomes zero and transmission coefficient becomes one when the matching condition of $\varepsilon_i = -\varepsilon_t = \varepsilon_o$ and $\mu_i = -\mu_t = \mu_o$ is satisfied. This can be seen in Figure 4.2(a). The same situation occurs when the relative permittivity and the relative permeability become equal to each other as it can be seen from Figure 4.2(b). Mathematically, this is obvious from Equation (4.5a) and Equation (4.5b). Note that, the magnitude of reflection and transmission coefficients versus relative permeability of hypothetical DNG medium shows the same behavior as in Figure 4.2(a) when $\varepsilon_{tr} = -1$ and as in Figure 4.2(b) when $\varepsilon_{tr} = -5$. It means that the reflection coefficient vanishes and the transmission coefficient becomes unity when the relative permittivity and permeability are equal to each other.
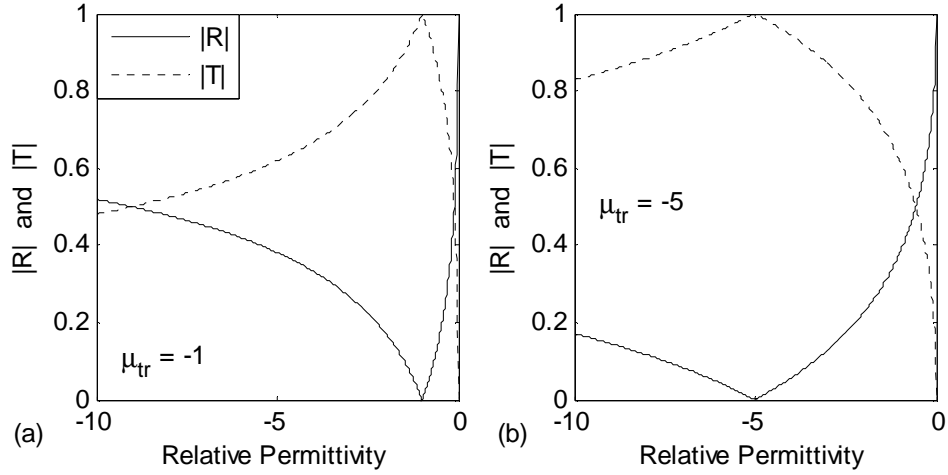
Figure 4.2: Magnitude of reflection and transmission coefficients versus relative permittivity of hypothetical DNG medium.

4.3 The Case of TE Wave Incidence

In this part, the case of TE wave incidence from free space upon a DNG metamaterial is studied. The incident electric field is assumed to have amplitude of E_i and points in the y-direction as shown in Figure 4.3. In this figure, ε_i and μ_i (ε_t and μ_t) stand for the permittivity and permeability of DPS medium (DNG metamaterial). So that, the incident electric and magnetic fields with the incident angle of θ_i and the wave number k_i ($= \omega\sqrt{\mu_i\varepsilon_i}$) can be expressed as:

$$\boldsymbol{E_i} = \boldsymbol{a}_y\, E_i \cdot \exp[-jk_i\,(x\sin\theta_i + z\cos\theta_i)] \tag{4.6a}$$

$$\boldsymbol{H_i} = (-\boldsymbol{a}_x\,\cos\theta_i + \boldsymbol{a}_z\,\sin\theta_i)\frac{k_i}{\omega\mu_i}E_i \cdot \exp[-jk_i\,(x\sin\theta_i + z\cos\theta_i)]. \tag{4.6b}$$

44
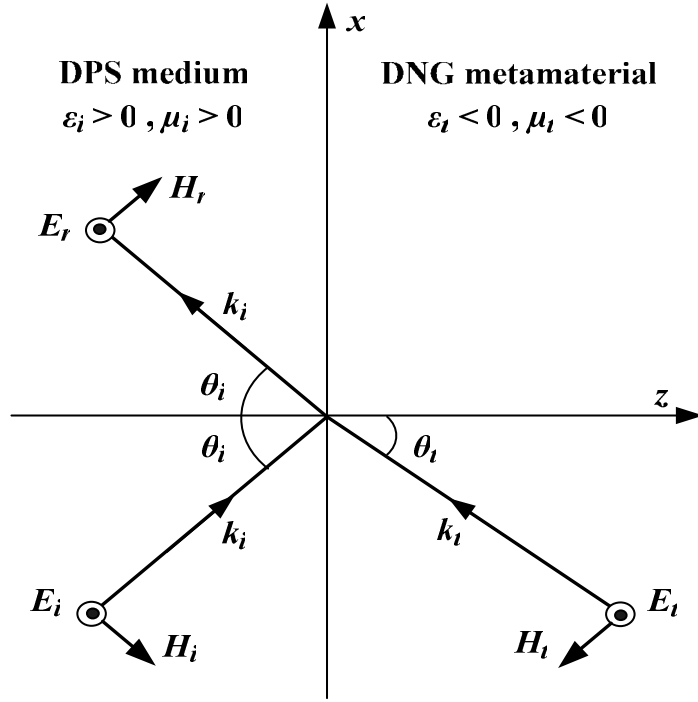
Figure 4.3: Reflection and transmission of TE waves by two planar semi infinite DPS and DNG media.

Similarly the reflected electric and magnetic fields can be written as follows:

$$E_r = a_y \, E_r \cdot \exp[-jk_i \, (x\sin\theta_i - z\cos\theta_i)] \tag{4.7a}$$

$$H_r = (a_x \, \cos\theta_i + a_z \, \sin\theta_i)\frac{k_i}{\omega\mu_i} E_r \cdot \exp[-jk_i \, (x\sin\theta_i - z\cos\theta_i)] \tag{4.7b}$$

where E_r is the amplitude of the reflected electric field. Also, the transmitted electric and magnetic fields can be written as:

$$\boldsymbol{E_t} = \boldsymbol{a}_y \, E_t \cdot \exp[-jk_t \, (x\sin\theta_t - z\cos\theta_t)] \tag{4.8a}$$

$$\boldsymbol{H_t} = (-\boldsymbol{a}_x \cos\theta_t - \boldsymbol{a}_z \sin\theta_t)\frac{k_t}{\omega\mu_t} E_t \cdot \exp[-jk_t \, (x\sin\theta_t - z\cos\theta_t)] \tag{4.8b}$$

where E_t and k_t are the amplitude and wave number of the transmitted electric field, and θ_t is the transmission (refracted) angle.

The reflection and transmission coefficients, and the relation between the incident, reflected, and transmission angles can be obtained by applying the boundary conditions on the continuity of the tangential components of the electric and magnetic fields. That gives the following relation known as Snell's law.

$$k_i \, \sin\theta_i = |\, k_t \, \sin\theta_t \,| \tag{4.9}$$

Using Equation (4.9), the continuity of the tangential components of the electric and magnetic fields yields:

$$E_i + E_r = E_t \tag{4.10a}$$

$$\frac{k_i}{\omega\mu_i}\cos\theta_i(-E_i + E_r) = -\frac{k_t}{\omega\mu_t}\cos\theta_t E_t . \tag{4.10b}$$

Solving the above two equations simultaneously for the reflection and transmission coefficients by means of their definitions given in the previous section leads to:

$$R = \frac{k_i \mu_t \cos\theta_i - k_t \mu_i \cos\theta_t}{k_i \mu_t \cos\theta_i + k_t \mu_i \cos\theta_t}$$

(4.11a)

$$T = \frac{2 k_i \mu_t \cos\theta_i}{k_i \mu_t \cos\theta_i + k_t \mu_i \cos\theta_t}.$$

(4.11b)

R and T of Equation (4.11a) and Equation (4.11b) are usually referred to as the plane wave Fresnel reflection and coefficients for the case of TE wave incidence (perpendicular polarization).

Now, same numerical example is provided to show the effect of the incident angle on the reflection and transmission coefficients. The classifications of DPS and DNG media shown in Figure 4.3 are assumed free space and hypothetical DNG metamaterial, respectively. The permittivities and permeabilities are: $\varepsilon_i = \varepsilon_o$ and $\mu_i = \mu_o$ for free space, $\varepsilon_t = -5\varepsilon_o$ and $\mu_t = -\mu_o$ for the hypothetical DNG metamaterial for Figure 4.4(a), and $\varepsilon_t = -5\varepsilon_o$ and $\mu_t = -5\mu_o$ for the hypothetical DNG metamaterial for Figure 4.4(b). From Figure 4.4, the reflection and transmission coefficients show ordinary increasing and decreasing behaviors, respectively. Note that, $|R|$ becomes zero and $|T|$ becomes one when $\varepsilon_i = -\varepsilon_o$ and $\mu_t = -\mu_o$.
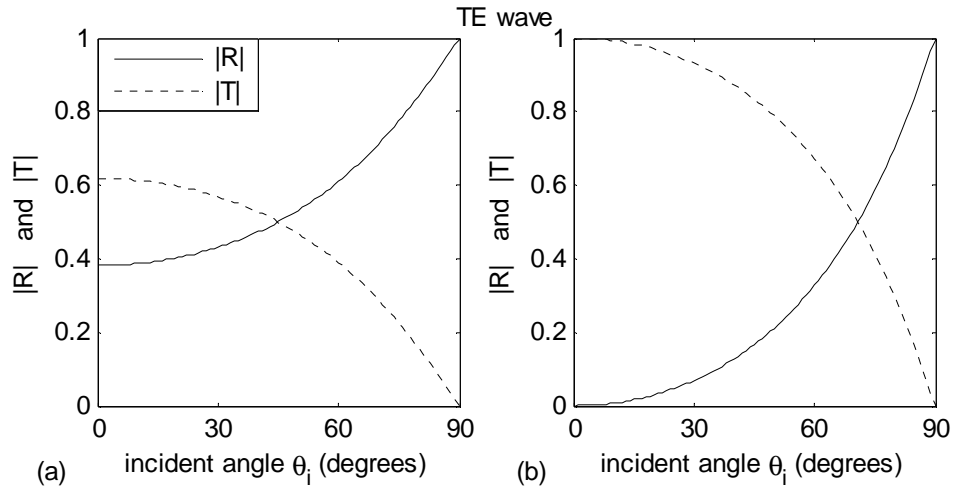
Figure 4.4: Magnitude of reflection and transmission coefficients as a function of incident angle for hypothetical DNG metamaterial. $\{\varepsilon_i = \varepsilon_o, \mu_i = \mu_o;$ (a) $\varepsilon_t = -5\varepsilon_o, \mu_t = -\mu_o;$ (b) $\varepsilon_t = -5\varepsilon_o, \mu_t = -5\mu_o\}$.

4.4 The Case of TM Wave Incidence
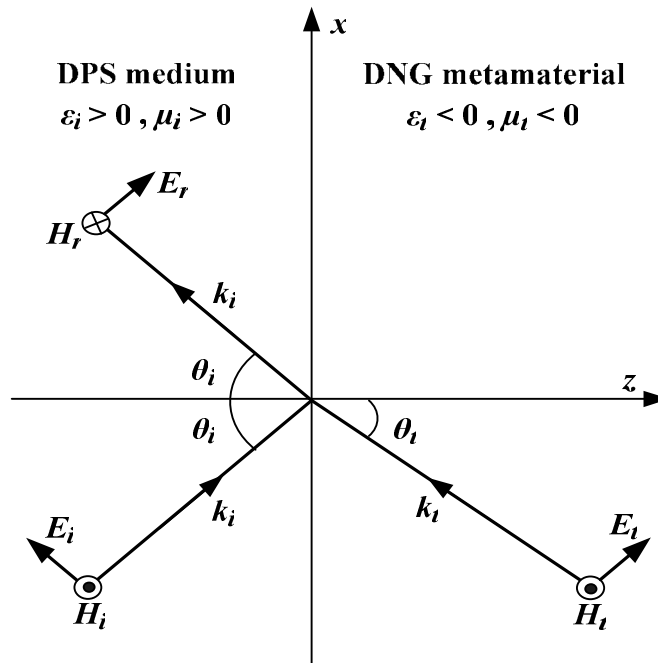
Figure 4.5: Reflection and transmission of TM waves by two planar semi infinite DPS and DNG media.

In the previous two sections, we examined wave reflection and transmission under normal and TE wave incidence. Let us now examine the reflection and transmission of waves under TM incidence. The geometry of the problem is shown in Figure 4.5. Using the same method outlined in the previous two sections, we can write the incident, reflected, and transmitted electric and magnetic fields as:

$$\boldsymbol{H_i} = \boldsymbol{a}_y \, H_i \cdot \exp[-jk_i \, (x\sin\theta_i + z\cos\theta_i)] \tag{4.12a}$$

$$\boldsymbol{E_i} = (\boldsymbol{a}_x \cos\theta_i - \boldsymbol{a}_z \sin\theta_i)\frac{k_i}{\omega\varepsilon_i} H_i \cdot \exp[-jk_i \, (x\sin\theta_i + z\cos\theta_i)] \tag{4.12b}$$

$$\boldsymbol{H_r} = -\boldsymbol{a}_y \, H_r \cdot \exp[-jk_i \, (x\sin\theta_i - z\cos\theta_i)] \tag{4.12c}$$

$$\boldsymbol{E_r} = (\boldsymbol{a}_x \cos\theta_i + \boldsymbol{a}_z \sin\theta_i)\frac{k_i}{\omega\varepsilon_i} H_r \cdot \exp[-jk_i \, (x\sin\theta_i - z\cos\theta_i)] \tag{4.12d}$$

$$\boldsymbol{H_t} = \boldsymbol{a}_y \, H_t \cdot \exp[-jk_t \, (x\sin\theta_t - z\cos\theta_t)] \tag{4.12e}$$

$$\boldsymbol{E_t} = (\boldsymbol{a}_x \cos\theta_t + \boldsymbol{a}_z \sin\theta_t)\frac{k_t}{\omega\varepsilon_t} H_t \cdot \exp[-jk_t \, (x\sin\theta_t - z\cos\theta_t)] \tag{4.12f}$$

where H_i, H_r, and H_t are the amplitudes of the incident, reflected, and transmitted magnetic fields, k_i, and k_t are the wave numbers of the incident and transmitted fields, θ_i and θ_t are the incident and transmission angles. Then, the plane wave reflection and transmission coefficients of a planar interface for TM wave incidence

can be formulated by imposing boundary conditions at the interface. Thus, at $z = 0$, we have

$$k_i \sin \theta_i = |k_t \sin \theta_t| \qquad (4.13a)$$

$$H_i - H_r = H_t \qquad (4.13b)$$

$$\frac{k_i}{\omega \varepsilon_i} \cos \theta_i (H_i + H_r) = \frac{k_t}{\omega \varepsilon_t} \cos \theta_t H_t. \qquad (4.13c)$$

At last, solving Equation (4.13b) and Equation (4.13c) together, the plane wave Fresnel reflection and coefficients for the case of TM wave incidence (parallel polarization) can be found as:

$$R = \frac{-k_i \varepsilon_t \cos \theta_i + k_t \varepsilon_i \cos \theta_t}{k_i \varepsilon_t \cos \theta_i + k_t \varepsilon_i \cos \theta_t} \qquad (4.14a)$$

$$T = \frac{2 k_t \varepsilon_i \cos \theta_i}{k_i \varepsilon_t \cos \theta_i + k_t \varepsilon_i \cos \theta_t}. \qquad (4.14b)$$

The effect of the incident angle on the reflection and transmission coefficients is presented numerically in Figure 4.6. DPS and DNG media shown in Figure 4.5 are assumed free space and hypothetical DNG metamaterial with $\varepsilon_i = \varepsilon_o$, $\mu_i = \mu_o$ for free space, $\varepsilon_t = -5\varepsilon_o$, $\mu_t = -\mu_o$ for the hypothetical DNG metamaterial for Figure 4.6(a), and $\varepsilon_t = -5\varepsilon_o$, $\mu_t = -5\mu_o$ for the hypothetical DNG metamaterial for Figure 4.6(b). It is

apparent that there is a Brewster angle where the reflection coefficient vanishes at 66°. After the Brewster angle, $|R|$ increases. The transmission coefficient shows decreasing response for both selections. From Figure 4.6(b), the same response occurs as in Figure 4.4(b) when $\varepsilon_t = -5\varepsilon_o$, $\mu_t = -5\mu_o$. Note that, $|R| = 0$ and $|T| = 1$ when $\varepsilon_t = -\varepsilon_o$ and $\mu_t = -\mu_o$.
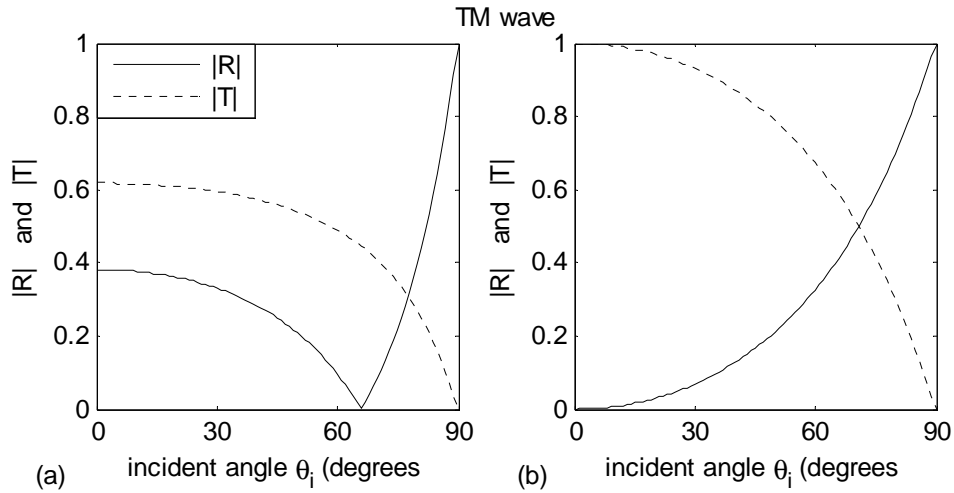
Figure 4.6: Magnitude of reflection and transmission coefficients versus incident angle for hypothetical DNG metamaterial. $\{\varepsilon_i = \varepsilon_o, \mu_i = \mu_o$; (a) $\varepsilon_t = -5\varepsilon_o, \mu_t = -\mu_o$; (b) $\varepsilon_t = -5\varepsilon_o, \mu_t = -5\mu_o\}$.

4.5 Reflection and Transmission by Double Negative Slab

A DNG metamaterial has interesting properties when it is placed as a slab between two dielectric media. In the light of previous three sections, it will be demonstrated that the theoretical and analytical investigations of electromagnetic wave propagation through double negative slab (DNS) embedded between two semi infinite media. It is constructed that a DNS between two different dielectric media with an incident electric field of the perpendicular polarization which reflects, propagates within the structure and transmits from the boundary. After examining the electric and magnetic fields using Maxwell's equations both inside and outside the DNS, the reflection and

transmission characteristics can be determined. The configuration of the problem for DNS comprised of two dielectric media is illustrated in Figure 4.7.
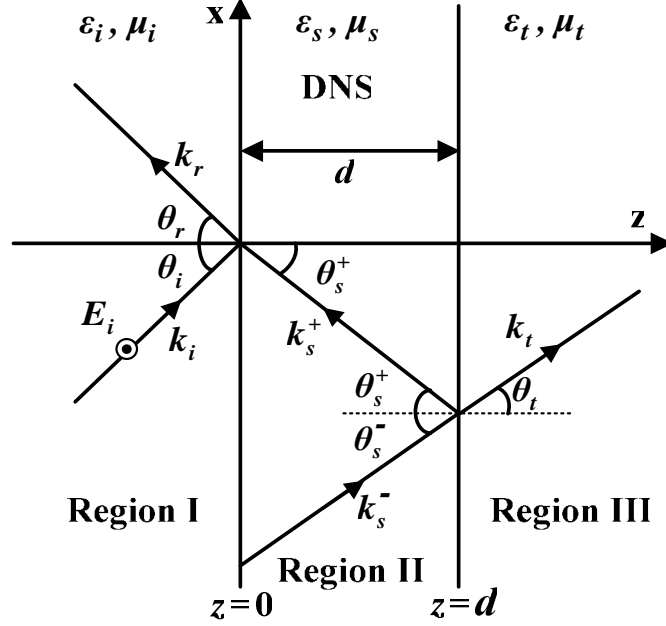
Figure 4.7: Geometry of DNS between two dielectric media for perpendicular (TE) polarized wave incident with an oblique angle.

Region I ($z \leq 0$) and Region III ($z \geq d$) are filled with two different dielectric media which have simultaneously positive permittivity and permeability. In turn, Region II ($0 \leq z \leq d$) is filled with DNG metamaterial which has simultaneously negative permittivity and permeability. A perpendicularly polarized electric field with the wave number k_i is incident on a DNS of the thickness d at the incident angle θ_i. Note again, $\exp(j\omega t)$ time dependence is assumed and suppressed throughout this work. Referring to Figure 4.7, the incident electric field with perpendicular (TE) polarization can be written as follows:

$$\boldsymbol{E} = \boldsymbol{a}_y \, E_i \cdot \exp[-j(k_{ix} x + k_{iz} z)] \tag{4.15}$$

52

where E_i is the amplitude of the incident electric field, k_{ix} ($k_{ix} = k_i\sin\theta_i$) and k_{iz} ($k_{iz} = k_i\cos\theta_i$) are the x- and z-components of the wave number k_i ($k_i = \omega\sqrt{\mu_i\varepsilon_i}$), and $\boldsymbol{a}_y$ is the unit Cartesian vector. According to the incident electric field given in Equation 4.15, the total electric fields in all regions can be expressed as:

$$\boldsymbol{E}_{\mathrm{I}} = \boldsymbol{a}_y\, E_i \cdot \exp[-j(k_{ix}\, x)] \cdot [\exp(-jk_{iz}\, z) + R\exp(jk_{iz}\, z)], \quad z \le 0 \tag{4.16a}$$

$$\boldsymbol{E}_{\mathrm{II}} = \boldsymbol{a}_y\, \exp[-j(k_{sx}\, x)] \cdot [A\exp(-jk_{sz}\, z) + B\exp(jk_{sz}\, z)], \quad 0 \le z \le d \tag{4.16b}$$

$$\boldsymbol{E}_{\mathrm{III}} = \boldsymbol{a}_y\, T\, E_i \cdot \exp[-j(k_{tx}\, x + k_{tz}\,(z-d))], \quad z \ge d \tag{4.16c}$$

where k_s and k_t are the wave numbers, R is the reflection coefficient, A and B are the amplitudes of the electric fields in the DNS, and T is the transmission coefficient. Note that, the subscripts i, s, and t refer to the incident, slab and transmitted medium, respectively. Also, the subscripts x and z represent the x- and z-components of the related wave numbers, respectively. These components for Region II (DNS) and Region III (transmitted region) are given by

$$k_{sx} = k_{tx} = k_{ix} = k_i \sin(\theta_i) \tag{4.17a}$$

$$k_{sz} = -\sqrt{\omega^2 \mu_s \varepsilon_s - k_{ix}^2} \tag{4.17b}$$

$$k_{tz} = \sqrt{\omega^2 \mu_t \varepsilon_t - k_{ix}^2} \tag{4.17c}$$

where $\mu_s(\mu_t)$ and $\varepsilon_s(\varepsilon_t)$ are the permeability and permittivity of the DNS (transmitted medium). Note that, Equation (4.17a) is known as Snell's law which gives the relation among the x-components of the wave numbers. Using the right- and left-hand procedure with Maxwell's equations, the magnetic fields for each region can be written as:

$$\boldsymbol{H}_{\mathrm{I}} = \frac{E_i}{\omega\mu_i} \cdot \exp[-j(k_{ix}x)] \cdot \{(-\boldsymbol{a}_x k_{iz} + \boldsymbol{a}_z k_{ix}) \cdot \exp[-jk_{iz}z]$$
$$+ (\boldsymbol{a}_x k_{iz} + \boldsymbol{a}_z k_{ix})R \cdot \exp[jk_{iz}z]\}$$
(4.18a)

$$\boldsymbol{H}_{\mathrm{II}} = \frac{1}{\omega\mu_s} \cdot \exp[-j(k_{sx}x)] \cdot \{(\boldsymbol{a}_x k_{sz} - \boldsymbol{a}_z k_{sx})A \cdot \exp[-jk_{sz}z]$$
$$+ (-\boldsymbol{a}_x k_{sz} - \boldsymbol{a}_z k_{sx})B \cdot \exp[jk_{sz}z]\}$$
(4.18b)

$$\boldsymbol{H}_{\mathrm{III}} = \frac{TE_i}{\omega\mu_t}(-\boldsymbol{a}_x k_{tz} + \boldsymbol{a}_z k_{tx}) \cdot \exp[-j(k_{tx}x + k_{tz}(z-d))].$$
(4.18c)

Note that, the wave number $k_s = |\boldsymbol{k}_s^+| = |\boldsymbol{k}_s^-|$, $\boldsymbol{k}_s^+$ being the propagation vector of forward wave and $\boldsymbol{k}_s^-$ the propagation vector of the backward wave as shown in Figure 4.7. In addition, the wave number of the DNS is defined as

$$k_s = -\omega\sqrt{\mu_s\varepsilon_s} = -\omega\sqrt{(-\mu_s' + j\mu_s'')(-\varepsilon_s' + j\varepsilon_s'')} = -k' + jk''$$
(4.19)

where μ_s', μ_s'', ε_s', ε_s'', k' and k'' are all positive real numbers. In Equation (4.19), the real part of the complex wave number has to be negative. Because, for the lossless DNS where $\mu_s'' = \varepsilon_s'' = 0$, the complex wave number must turn to

$k_s = -\omega\sqrt{\mu_s'\varepsilon_s'} = -k'$ which is the common knowledge assumed in many studies [35–66].

To find the reflection and transmission coefficients, the continuity of tangential components of the electric and magnetic fields, both in phase and magnitude, is used. The continuity of these fields in phase requires

$$k_i \sin\theta_i = k_r \sin\theta_r = |k_s \sin\theta_s^+| = |k_s \sin\theta_s^-| = k_t \sin\theta_t \tag{4.20}$$

where θ_s^+ and θ_s^- are the reflection angle at $z = 0$ and the transmission angle at $z = d$, respectively. Equation (4.20) gives the relation between the incidence, reflection and transmission angles. From this equation, we obtain $k_i = k_r$, $\theta_i = \theta_r$, and $\theta_s = \theta_s^+ = \theta_s^-$. Now, imposing boundary conditions at the interfaces of $z = 0$ and $z = d$, the reflection and transmission coefficients can be found as:

$$R^{TE} = \frac{[(k_{iz}\mu_s - k_{sz}\mu_i)(k_{sz}\mu_t + k_{tz}\mu_s) \cdot e^{j\varphi}] + [(k_{iz}\mu_s + k_{sz}\mu_i)(k_{sz}\mu_t - k_{tz}\mu_s) \cdot e^{-j\varphi}]}{[(k_{iz}\mu_s + k_{sz}\mu_i)(k_{sz}\mu_t + k_{tz}\mu_s) \cdot e^{j\varphi}] + [(k_{iz}\mu_s - k_{sz}\mu_i)(k_{sz}\mu_t - k_{tz}\mu_s) \cdot e^{-j\varphi}]} \tag{4.21}$$

$$T^{TE} = \frac{4k_{iz}k_{sz}\mu_s\mu_t}{[(k_{iz}\mu_s + k_{sz}\mu_i)(k_{sz}\mu_t + k_{tz}\mu_s) \cdot e^{j\varphi}] + [(k_{iz}\mu_s - k_{sz}\mu_i)(k_{sz}\mu_t - k_{tz}\mu_s) \cdot e^{-j\varphi}]} \tag{4.22}$$

where $k_{pz} = k_p \cdot \cos(\theta_p)$, $(p = i,\ s,\ t)$, and $\varphi = k_{sz}d$. Note that, μ_i, μ_s, and μ_t are the permeabilities of the incident, DNS, and transmitted media. By using the same procedure, the reflection and transmission coefficients for parallel (TM) polarized wave can be formulated as follows:

$$R^{TM} = \frac{[(-k_{iz}\varepsilon_s + k_{sz}\varepsilon_i)(k_{sz}\varepsilon_t + k_{tz}\varepsilon_s) \cdot e^{j\varphi}] - [(k_{iz}\varepsilon_s + k_{sz}\varepsilon_i)(k_{sz}\varepsilon_t - k_{tz}\varepsilon_s) \cdot e^{-j\varphi}]}{[(k_{iz}\varepsilon_s + k_{sz}\varepsilon_i)(k_{sz}\varepsilon_t + k_{tz}\varepsilon_s) \cdot e^{j\varphi}] + [(k_{iz}\varepsilon_s - k_{sz}\varepsilon_i)(k_{sz}\varepsilon_t - k_{tz}\varepsilon_s) \cdot e^{-j\varphi}]} \quad (4.23)$$

$$T^{TM} = \frac{k_t}{k_i} \cdot \frac{4k_{iz}k_{sz}\varepsilon_i\varepsilon_s}{[(k_{iz}\varepsilon_s + k_{sz}\varepsilon_i)(k_{sz}\varepsilon_t + k_{tz}\varepsilon_s) \cdot e^{j\varphi}] + [(k_{iz}\varepsilon_s - k_{sz}\varepsilon_i)(k_{sz}\varepsilon_t - k_{tz}\varepsilon_s) \cdot e^{-j\varphi}]} \quad (4.24)$$

where ε_i, ε_s, and ε_t are the permittivities of the incident, DNS, and transmitted media. Implicit form of these coefficients for both polarizations can be written as:

$$R = \frac{R_{01} + R_{12}\exp(j2k_{sz}d)}{1 + R_{01}R_{12}\exp(j2k_{sz}d)} \quad (4.25)$$

$$T = \frac{4\exp(jk_{sz}d)}{(1+r_{01})(1+r_{12})[1 + R_{01}R_{12}\exp(j2k_{sz}d)]} \quad (4.26)$$

in which R_{01} and R_{12} are the Fresnel's reflection coefficients

$$R_{01} = \frac{1-r_{01}}{1+r_{01}}, \quad R_{12} = \frac{1-r_{12}}{1+r_{12}}, \quad (4.27)$$

where for perpendicular polarizations (TE waves)

$$r_{01} = \frac{\mu_i k_{sz}}{\mu_s k_{iz}}, \quad r_{12} = \frac{\mu_s k_{tz}}{\mu_t k_{sz}}, \quad (4.28)$$

and for parallel polarizations (TM waves)

$$r_{01} = \frac{\varepsilon_i k_{sz}}{\varepsilon_s k_{iz}}, \; r_{12} = \frac{\varepsilon_s k_{tz}}{\varepsilon_t k_{sz}} \; . \tag{4.29}$$

Then, the z-component of the incident, reflected, and transmitted powers can be represented as follows:

$$P_{iz} = \left| \frac{k_{iz}}{\mu_i} E_i^2 \right|, \; P_{rz} = \left| \frac{k_{iz}}{\mu_i} (RE_i)^2 \right|, \text{ and } P_{tz} = \left| \frac{k_{tz}}{\mu_t} (TE_i)^2 \right|. \tag{4.30}$$

If the incident electric field is normalized to unity and DNS is the lossy medium, the conservation of the power yields

$$\left| R^{TE,TM} \right|^2 + \left| \frac{k_{tz} \mu_i}{k_{iz} \mu_t} \right| \cdot \left| T^{TE,TM} \right|^2 = 1 - P_{loss} \; . \tag{4.31}$$

Note that, the power vector is in the opposite direction to the wave vector **k** and the phase velocity. The vectors **E**, **H**, and **k** form a left-handed system. In this system, the power propagates in the opposite direction of **k**. Thus, the plane wave with the wave vector **k** in the DNG medium is a backward wave.

4.5.1 Numerical Results for Hypothetical DNG medium as a DNS

Since the reflected and the transmitted powers are functions of the structure parameters (the permittivities and the permeabilities of the media), the incidence angle, the slab thickness and the frequency, the reflected and transmitted powers have been calculated as functions of the frequency and the incident angle for different structure parameters. Operation frequency is assumed to be $f_o = 10$ GHz and the slab thickness is $d = \lambda_o / 2$ where λ_o is the wavelength in free space at the operation frequency f_o. The thickness of the slab is assumed to be constant in all calculations. Magnitudes of the permeabilities of three media are select to be equal ($\mu_i = -\mu_s = \mu_t = \mu_o$), and six different cases are considered by changing the permittivities of the media. Note that, some parts of this study is presented in [62].

Case (a): $|\varepsilon_t| < |\varepsilon_s| < |\varepsilon_i|$ ($\varepsilon_i = 9\varepsilon_o$, $\varepsilon_s = -4\varepsilon_o$, $\varepsilon_t = \varepsilon_o$); the first dielectric medium is denser than the other media and the last dielectric medium is less dense than the DNS. The critical angle at interface I is $\theta_{c1} = 41.8^o$ and at interface II it is $\theta_{c2} = 30^o$. Figure 4.8(a) shows the reflected and transmitted powers, P_r and P_t, versus incidence angle. It is seen that total internal reflection occurs for TE and TM waves at the incidence angle greater than or equal to 19.5^o, because θ_s becomes greater than θ_{c2} for $\theta_i \geq 19.5^o$.

Case (b): $|\varepsilon_s| < |\varepsilon_t| < |\varepsilon_i|$ ($\varepsilon_i = 9\varepsilon_o$, $\varepsilon_s = -\varepsilon_o$, $\varepsilon_t = 4\varepsilon_o$); the double-negative medium is less dense than the other media. The reflected and transmitted powers versus incidence angle are presented in Figure 4.8(b) for this case. Here total internal reflection occurs at the critical angle of 19.5^o. But in this case, P_r (P_t) for the TE wave does not go sharply to the value of one (zero) after the critical angle.

Case (c): $|\varepsilon_t| < |\varepsilon_i| < |\varepsilon_s|$ ($\varepsilon_i = 4\varepsilon_o$, $\varepsilon_s = -9\varepsilon_o$, $\varepsilon_t = \varepsilon_o$); The results obtained for this case are shown in Figure 4.8(c). The critical angle is 19.5^o at interface II and there is no critical angle at interface I. However, as it can be observed form Figure 4.8(c) that the total reflection occurs $\theta_i \geq 30^o$ since θ_s becomes greater than 19.5^o.

Case (d): $|\varepsilon_i| < |\varepsilon_t| < |\varepsilon_s|$ ($\varepsilon_i = \varepsilon_o$, $\varepsilon_s = -9\varepsilon_o$, $\varepsilon_t = 4\varepsilon_o$); Figure 4.8(d) presents P_r and P_t versus incidence angle for this case. Total reflection occurs at 90° for TE and TM waves. P_t becomes nearly unity around 67° for TM wave. It means that Quasi-Brewster angle occurs at this angle of incidence.

Case (e): $|\varepsilon_s| < |\varepsilon_i| < |\varepsilon_t|$ ($\varepsilon_i = 4\varepsilon_o$, $\varepsilon_s = -\varepsilon_o$, $\varepsilon_t = 9\varepsilon_o$); The reflected and transmitted powers as a function of incidence angle are shown in Figure 4.8(e) for the case where the DNS is less dense than the others. Characteristics of the reflected and transmitted powers of TE and TM waves are similar to the case (b) except for the total reflection angle. Here the total reflection occurs at incidence angle 30°.

Case (f): $|\varepsilon_i| < |\varepsilon_s| < |\varepsilon_t|$ ($\varepsilon_i = \varepsilon_o$, $\varepsilon_s = -4\varepsilon_o$, $\varepsilon_t = 9\varepsilon_o$); Figure 4.8(f) illustrates the reflected and transmitted powers versus incidence angle when the first dielectric medium is less dense than the other media. At 90°, total reflection occurs for both TE and TM waves. Quasi-Brewster angle for TM wave occurs around $\theta_i = 65^o$.
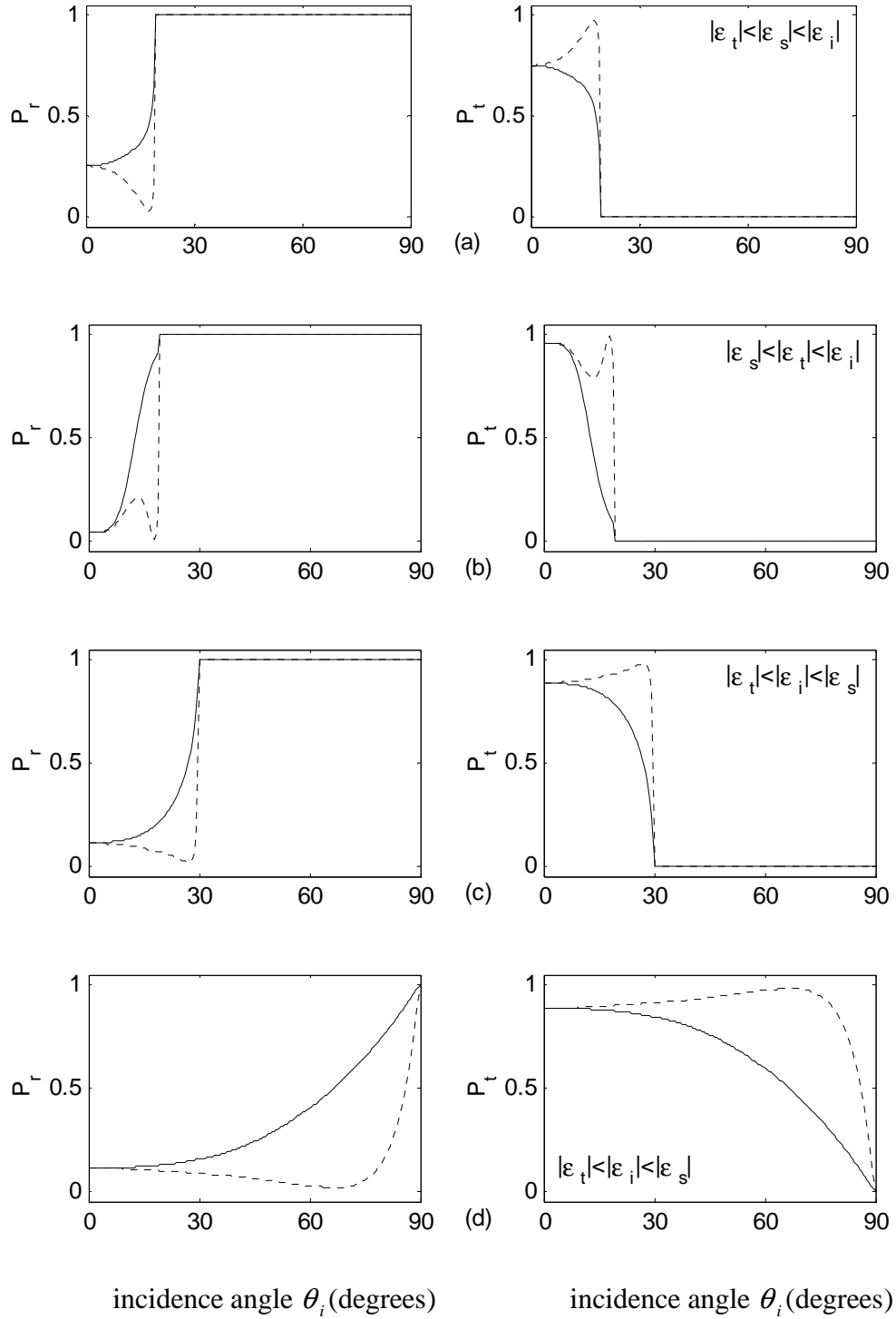
Figure 4.8: Reflected and transmitted powers of TE and TM waves versus incidence angle. Figures on the left hand side denote the reflected powers and on the right hand side denote the transmitted powers. The solid lines correspond to the TE wave and the dotted lines correspond to the TM wave.
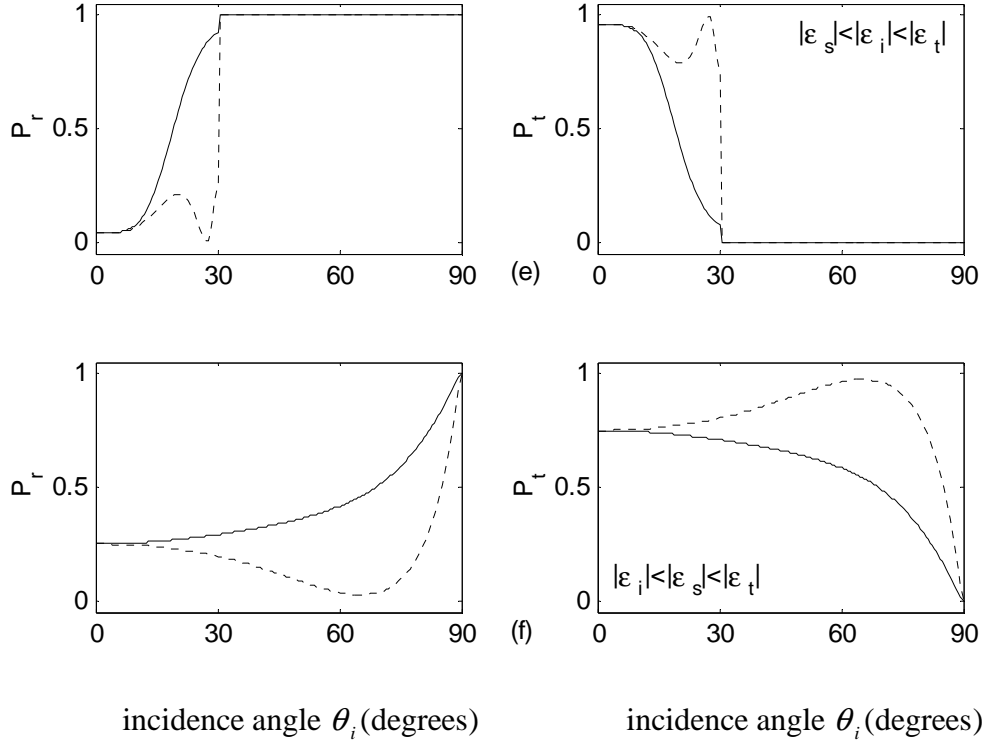
Figure 4.8: (Continue) Reflected and transmitted powers of TE and TM waves versus incidence angle. Figures on the left hand side denote the reflected powers and on the right hand side denote the transmitted powers. The solid lines correspond to the TE wave and the dotted lines correspond to the TM wave.

Another important parameter that influences the reflected and transmitted powers is the frequency of operation. In this paper, the reflected and the transmitted powers of the TE and the TM waves are calculated at various frequencies for different values of $\varepsilon_i, \varepsilon_s, \varepsilon_t$. Note that the permeabilities of the media and the thickness of the slab are the same as in the previous examples. It is also worth mentioning that although the permittivity and the permeability of the DNS are functions of the frequency, it is assumed that both parameters are constant over a frequency band in this study. However, this approximation also allows commenting on the effect of the frequency. P_r and P_t versus frequency are presented in Figure 4.9(a) for the case $|\varepsilon_s| < |\varepsilon_t| < |\varepsilon_i|$ ($\varepsilon_i = 9\varepsilon_o$, $\varepsilon_s = -\varepsilon_o$, $\varepsilon_t = 4\varepsilon_o$) at an incidence angle of $\theta_i = 19^o$ that is very close to the angle where total reflection occurs. It is seen that, at low frequency values, both the TE and the TM waves are totally transmitted. However, as the frequency

increases, the incident power is almost totally reflected in the TE polarization case. The reflected and the transmitted powers remain almost constant over the frequency range studied for the TM polarization case. This result suggests the possibility of separating the TE and TM components of a general wave in a frequency band for a given incidence angle, at which the transmitted wave is almost the TM polarized wave and the reflected wave is almost the TE polarized wave. Figure 4.9(b) shows the reflected and transmitted powers as a function of frequency for the case $|\varepsilon_i| < |\varepsilon_s| < |\varepsilon_t|$ ($\varepsilon_i = \varepsilon_o$, $\varepsilon_s = -4\varepsilon_o$, $\varepsilon_t = 9\varepsilon_o$). For this case, the incident angle is chosen to be 80°, and it can be deduced that P_r and P_t make oscillations at all frequencies considered. P_r and P_t oscillate as the fraction of the thickness of the DNS is varied; this caused by interference. The oscillation has a period and the response of P_r and P_t is symmetric with respect to this period. For given structure parameters, Figure 4.9 suggests the possibility of constructing the reflection and transmission coatings by tuning the fraction of DNS.

Note that, as a first method for the verification, the conservation of the power is satisfied for both polarizations. As a second method, a transmission line equivalent circuit model is obtained for the structure given in Figure 4.7 [89]. Details of this method are given in Appendix. Both methods give the same numerical values for all computations. Thus, the results are verified and validated by means of two methods.

As a conclusion, at a specific frequency of operation, it is deduced that there occurs total internal reflection or total transmission for a given permittivity and permeability set of the structure under investigation. The frequency also changes the behavior of the reflected and the transmitted powers. A special case, where the incidence angle is close to the total reflection angle, is also studied and it is seen that the TE wave is almost totally reflected as the frequency increases as opposed to the TM wave which is almost totally transmitted throughout the frequency range studied. This observation suggests the possibility of separating the TE and TM components of a general wave for a given incidence angle in a frequency band. Furthermore, DNS

can be used in layered structures for constructing the reflection and/or transmission coatings by tuning the thickness of DNS.
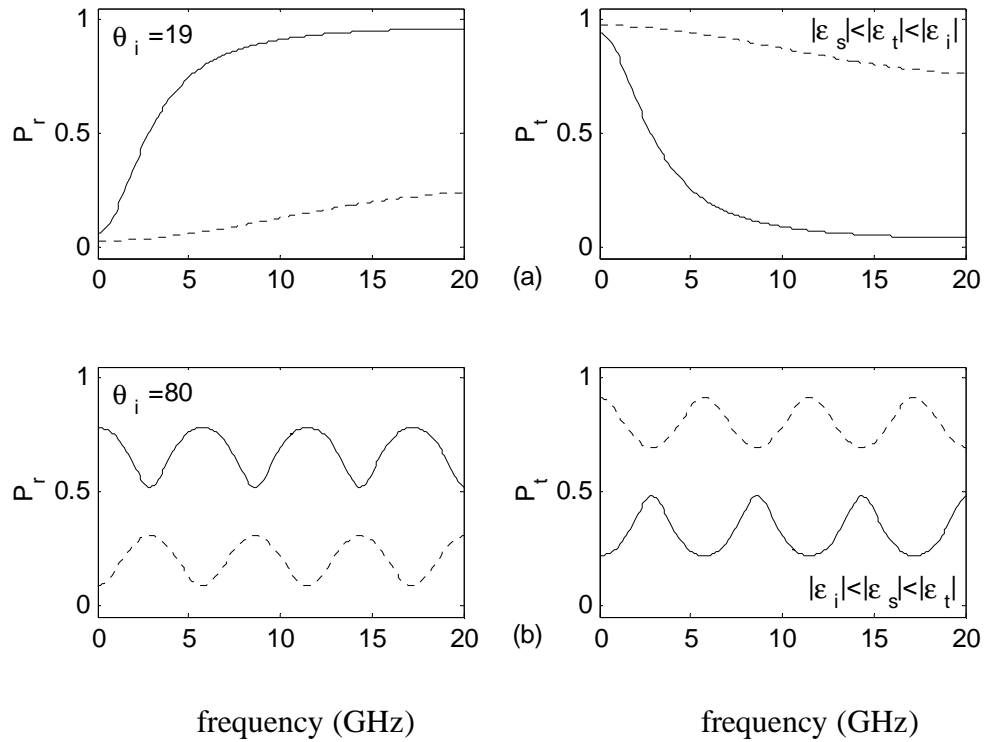
Figure 4.9: Reflected and transmitted powers of TE and TM waves as a function of frequency. Figures on the left hand side denote the reflected powers and on the right hand side denote the transmitted powers. The solid lines correspond to the TE wave and the dotted lines correspond to the TM wave.

4.5.2 Numerical Results for Lorentz Medium as a DNS

In the previous section, the loss power is not considered in the computations due to the lossless DNS. As it is explained in Chapter 3, Lorentz medium has frequency dispersive parameters and it is in the form of lossy medium. The reflected P_r, transmitted P_t, and loss P_{loss} powers for the Lorentz medium model are calculated as a function of the incidence angle, the frequency and the slab thickness for changing values of the damping frequency. In the calculation, the DNS is described by using

the Lorentz medium model in which the permittivity and permeability of the medium are given in Equation (3.1) and Equation (3.2). In the calculations, the following parameters are used as in References [38] and [80], f_{mp} = 13.0 GHz, f_{mo} = 8.0 GHz, f_{ep} = 12.80 GHz, and f_{eo} = 10.30 GHz. The electronic damping frequency and the magnetic damping frequency are selected to be equal each other, $\delta_e = \delta_m = \Gamma$. The design frequency is assumed to become f_o = 11.5 GHz. The design frequency was chosen by an arbitrary decision, but it must be in the frequency band where the permittivity and the permeability of the DNS are both simultaneously negative. Region I and Region III given in Figure 4.7 are assumed to be lossless and the permeabilities of them are equal to the permeability of the free space, $\mu_i = \mu_t = \mu_o$. The relative permittivities of them are 1.0 (free-space) and 16.0 (Germanium), respectively. The slab thickness is assumed to be one half-wavelength long at the design frequency f_o when the incidence angle and the frequency changed. Most of the work presented here appeared as a journal article in Opto-Electronics Review [63].

Figure 4.10 shows the reflected P_r, transmitted P_t, and loss P_{loss} powers for TE and TM waves, respectively, as a function of the incidence angle. We can see that the reflected power slowly decreases up to 34° for TE wave and up to 39° for TM wave. After this angle, it increases consistently with the incidence angle for both waves. The transmitted power remains almost constant up to the mentioned angles and after that it decreases for both waves. The loss power increases between 0° and 40°, reaches its maximum values between 40° and 45° and after that it decreases consistently for TE wave. The loss power for TM wave shows similar characteristic as in TE wave. Note that, as the damping frequency Γ increases, the initial values of the reflected and transmitted powers decrease. But, for the loss power, the initial value increases with the increasing values of the damping frequency. In addition, the low loss condition is happened when Γ = 100 MHz, due to the loss power has small values. This means that the real part of the permittivity and the permeability of the DNS are much greater than the imaginary part of them. This implies the real part of the complex wave number given in Equation (4.19) is also much greater than the imaginary part of it.

Figure 4.11 depicts the frequency variation of the reflected, transmitted, and loss powers at the incidence angle of 30° when the damping frequency changes. The frequency is changed between 10.31 GHz and 12.79 GHz, because the simultaneously negative permittivity and permeability can be realized in this range, according to Equation (3.1) and Equation (3.2). This range can be expanded and/or narrowed by using different resonance, plasma, and damping frequencies that is used in this computation. It can be seen that, from Figure 4.11, P_r, P_t, and P_{loss} for TE and TM waves have a nonlinear characteristic and variable properties when the frequency changes. They show increasing, decreasing and oscillatory behaviours in different frequency ranges. The oscillatory decreasing and increasing features of them can be seen easily. One interesting property is that P_r shows the oscillation characteristic like one-dimensional Fabry-Perot slab oscillation below ~11.5 GHz and it increases rapidly and approaches to unity after ~11.5 GHz when the damping frequency decreases. Thus, it is said that the frequency response of the powers has a non-fixed characteristic in the Lorentz medium model as a frequency-dispersive and lossy DNS.

Figure 4.12 presents the reflected, transmitted, and loss powers for the Lorentz medium model versus the slab thickness at the incidence angle of 30°. The slab thickness is changed from $\lambda/5$ (0.522 cm) to λ (2.609 cm). From Figure 4.12(a), the reflected power changes like an oscillation function for all values of the damping frequency. From Figure 4.12(b), the characteristic of the transmitted power like an oscillatory decreasing function. But this characteristic turns to the ordinary decreasing function when the damping frequency increases. From Figure 4.12(c), the loss power varies as the increasing function with the increasing damping frequency. Also, there is some oscillation in the response of the powers. This allows constructing the reflection and transmission coatings by tuning the fraction of the thickness of DNS.

TE wave   TM wave

Figure 4.10: The reflected, transmitted, and loss powers of TE and TM waves for the Lorentz medium model as a function of the incidence angle.

TE wave   TM wave

Figure 4.11: The reflected, transmitted, and loss powers of TE and TM waves for the Lorentz medium model against the frequency.

TE wave

TM wave

Figure 4.12: The reflected, transmitted, and loss powers of TE and TM waves for the Lorentz medium model versus the slab thickness.

4.5.3 Numerical Results for Drude Medium as a DNS

In this section, the Drude medium model as a DNS is used to compute the reflected P_r, transmitted P_t, and loss P_{loss} powers versus the incidence angle, the frequency and the slab thickness when the damping frequency changes. Note that, most of this work is presented in the journal of Opto-Electronics Review [63]. The permittivity and permeability of the Drude medium model are calculated using Equation (3.3) and Equation (3.4). In our calculations, f_{mp} = 10.95 GHz and f_{ep} = 14.50 GHz are used as in References [36] and [38]. The electronic and magnetic damping frequencies are selected to be equal each other. The design frequency is assumed to become f_o = 6.0 GHz. The slab thickness is again assumed to be one half-wavelength long at the design frequency f_o in which the permittivity and the permeability of the DNS are both simultaneously negative when the frequency and the incidence angle changed. The permeabilities and the relative permittivities of Region I and Region III are the same with the Lorentz medium model.

Figure 4.13 points out the reflected, transmitted, and loss powers versus the incidence angle for TE and TM waves, respectively. The reflected power is monotonically increasing with the angle of incidence for TE and TM waves. However, the transmitted and loss powers for both waves are monotonically decreasing with the angle of incidence. The variation in the damping frequency affects the initial values of the reflected, transmitted and loss powers. The initial value of the loss power increases with the increasing values of the damping frequency. For the reflected and transmitted powers, it decreases when the damping frequency increases. In addition, the low loss condition is again happened as in the Lorentz medium model when Γ = 100 MHz, due to the loss power has small values which refers to $\mu_s' >> \mu_s''$, $\varepsilon_s' >> \varepsilon_s''$, and $k' >> k''$.

Figure 4.14 illustrates the frequency response the reflected, transmitted, and loss powers at the incidence angle of 30° for the changing values of the damping

frequency. Here, the frequency range is between 2.0 GHz and 10.94 GHz. This range is wider than the range of the Lorentz medium model. At this point, we can say that, the simultaneously negative permittivity and permeability can be realized in the wide frequency band for the Drude medium model more easily than for the Lorentz medium model. From Figure 4.14(a), P_r for TE and TM waves displays a slightly oscillatory rising property up to ~10 GHz and then it increases. From Figure 4.14(b), P_t for both waves behaves as an oscillatory increasing function up to ~10 GHz and after that it decreases. From Figure 4.14(c), P_{loss} for TE and TM waves shows an oscillatory decreasing behavior. Thus, it can be said that, the powers generally have oscillatory characteristics in the Drude medium model which is used as a frequency-dispersive and lossy DNS for the given configuration.

Figure 4.15 shows the reflected, transmitted, and loss powers for the Drude medium model as a function of the slab thickness at the incidence angle of 30°. The slab thickness is changed from $\lambda/5$ (1.0 cm) to λ (5.0 cm). It is observed that, the characteristic of P_r of TE and TM waves for this arrangement like an oscillatory function for all damping frequency values. P_t for both waves has an almost periodically decline characteristic when $\Gamma = 100$ MHz. It shows an oscillatory decreasing behavior when $\Gamma = 500$ MHz and $\Gamma = 1$ GHz. On the other hand, P_{loss} for both waves shows an oscillatory increasing behavior with the increasing values of the damping frequency. Also, the reflection and transmission coatings can be constructed by tuning the thickness of DNS.

TE wave   TM wave
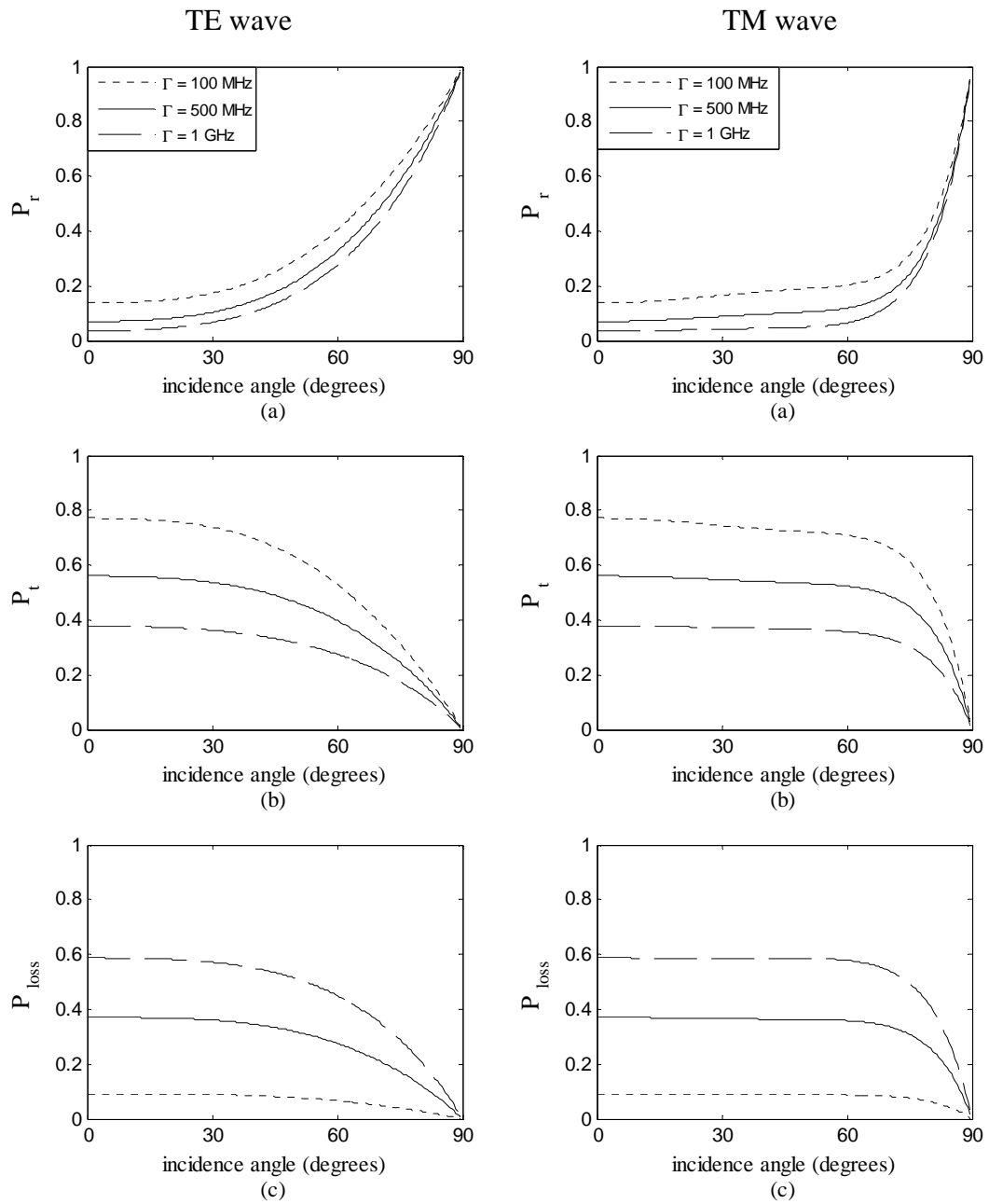
Figure 4.13: The reflected, transmitted, and loss powers of TE and TM waves for the
Drude medium model versus the incidence angle.

TE wave   TM wave
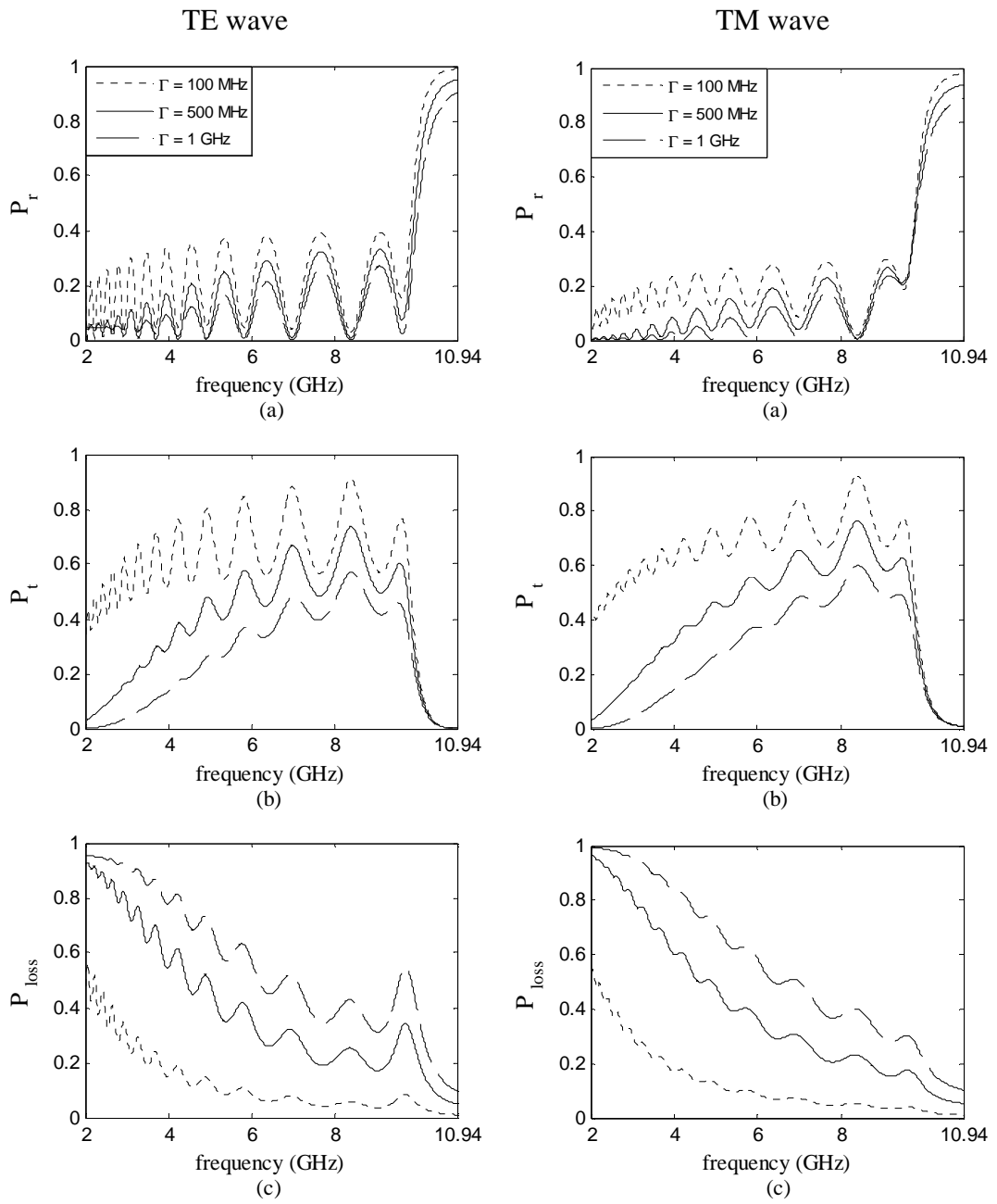
Figure 4.14: The reflected, transmitted, and loss powers of TE and TM waves for the
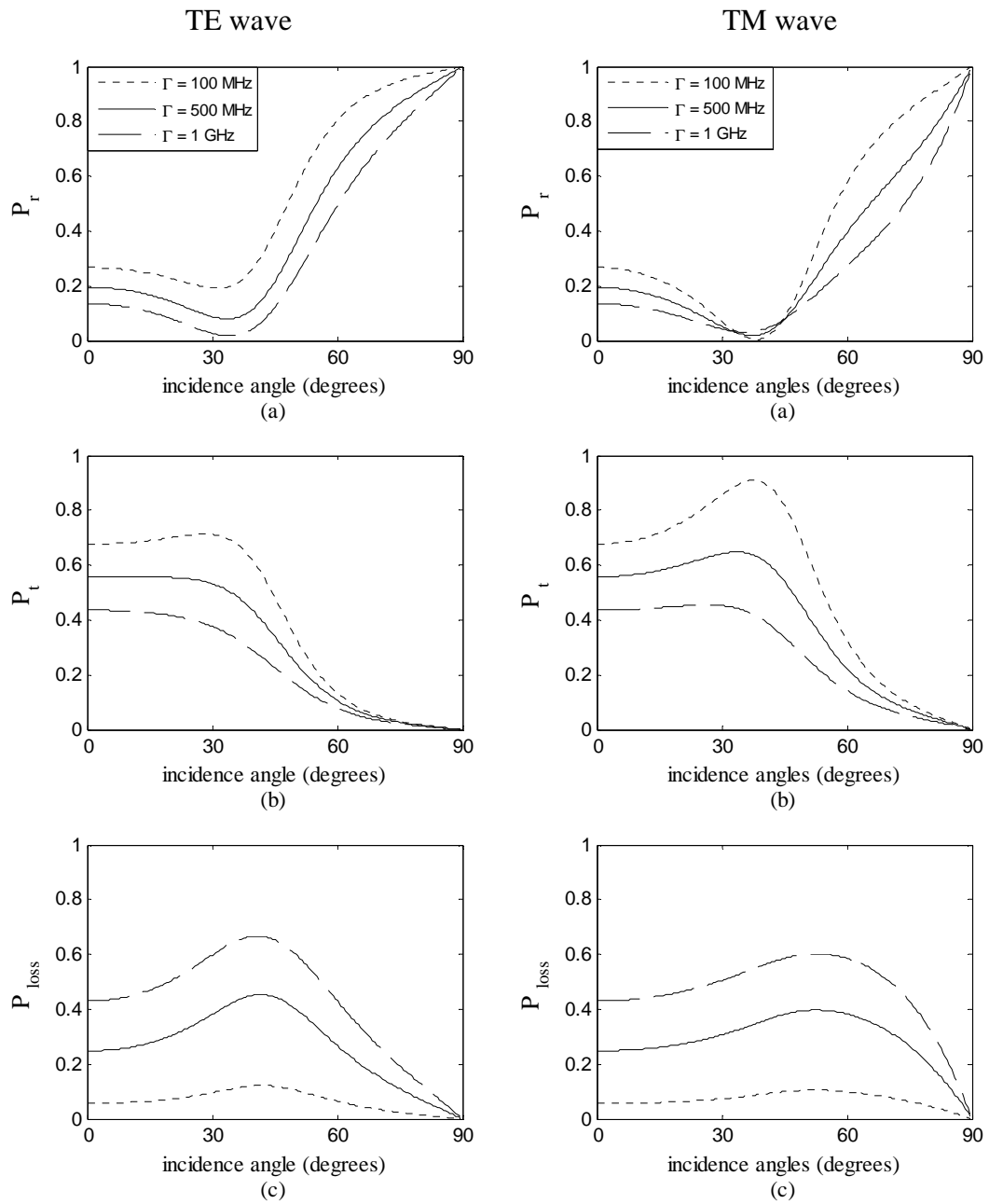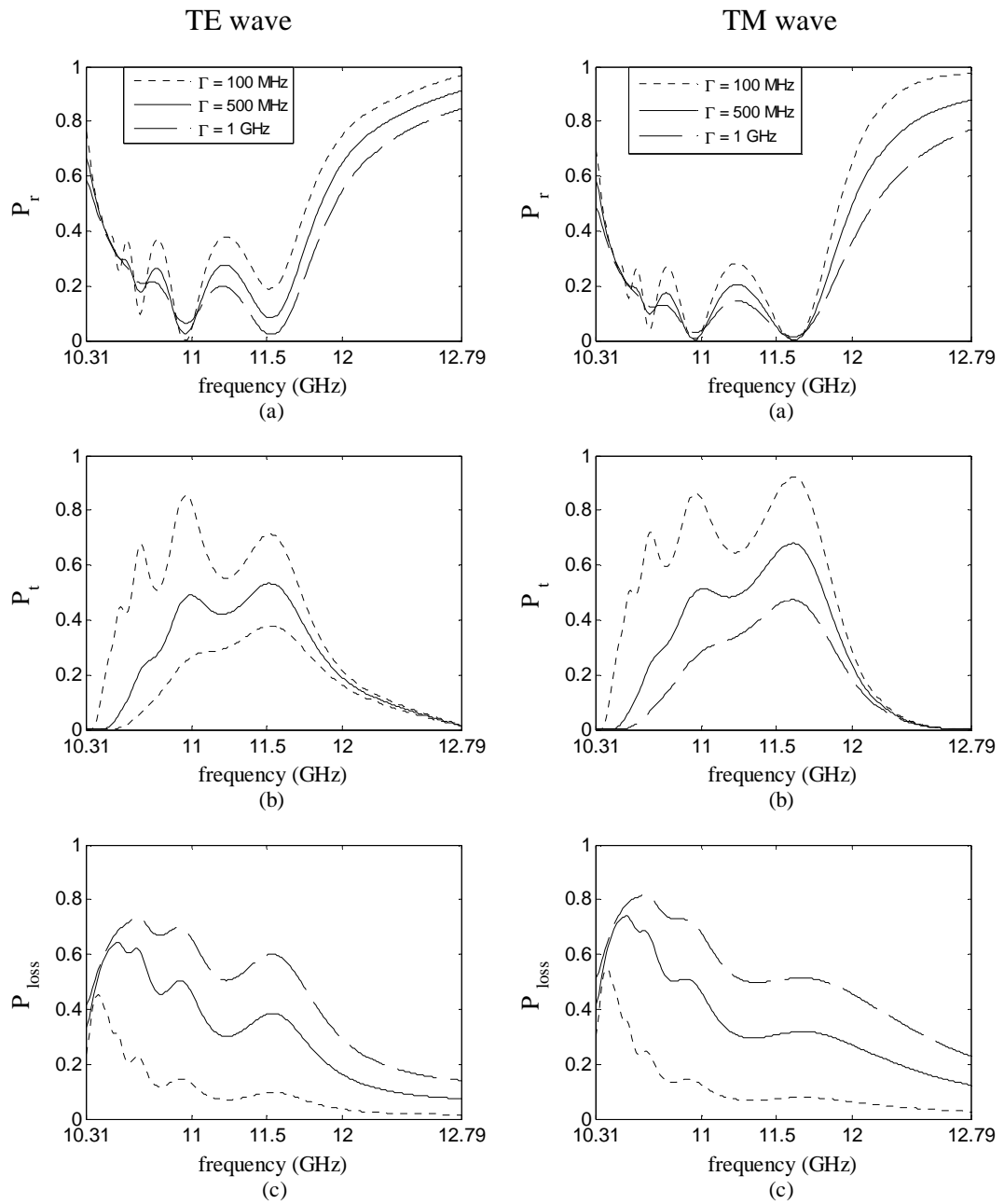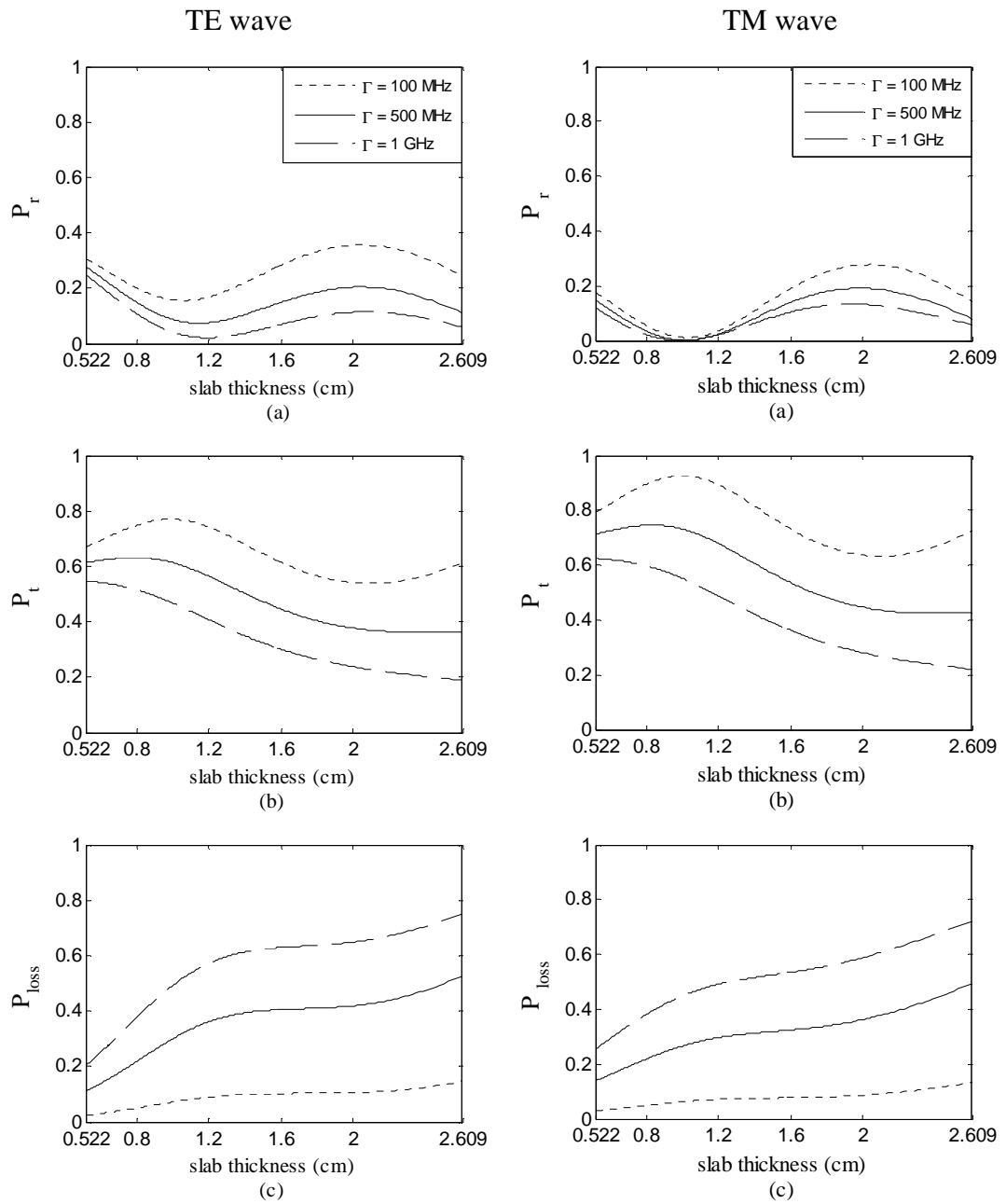Drude medium model against the frequency.

TE wave   TM wave

Figure 4.15: The reflected, transmitted, and loss powers of TE and TM waves for the
Drude medium model as a function of the slab thickness.

4.5.4 Numerical Results for Cold Plasma Medium as a DNS

Here, the cold plasma medium model as a DNS is used to compute the reflected P_r, transmitted P_t, and loss P_{loss} powers versus the incidence angle, the frequency and the slab thickness. The main difference of this medium among the others is that it has frequency dispersive and lossless parameters. The permittivity and permeability of this medium are calculated using Equation (3.5) and Equation (3.6). In the calculations, 8.50 GHz and 14.50 GHz are used for the plasma frequencies. The design frequency is assumed to become $f_o = 6.0$ GHz. The slab thickness is again assumed to be one half-wavelength long at the design frequency f_o when the incidence angle and the frequency varied. The permeabilities and the relative permittivities of Region I and Region III are the same with the Lorentz medium model. In all calculations, dotted line corresponds to $f_{ep} = f_{mp} = 8.50$ GHz, solid line to $f_{ep} = 14.50$ GHz, $f_{mp} = 8.5$ GHz, and dashed line to $f_{ep} = f_{mp} = 14.50$ GHz.

Figure 4.16 shows the reflected and transmitted powers of TE and TM waves versus incidence angle for the cold plasma medium model for different values of the plasma frequencies. It is apparent that as the incidence angle increases, the reflected and transmitted powers for TE wave show ordinary increasing and decreasing behavior, respectively. In the case of TM waves, this behavior appears only when the electric and magnetic plasma frequencies are 14.50 GHz. In the other two situations, there is Brewster angles around 76° and 77° (solid and dotted lines) for TM wave in which the reflection and transmission coefficients become zero and one, respectively.

The reflected and transmitted powers of TE and TM waves against the frequency for the cold plasma medium model are presented in Figure 4.17 when the incidence angle is 30°. The reflected power for TM wave has more oscillation than the reflected power of TE wave between the frequency ranges of 0–3 GHz. Also, the behavior of the reflected wave for both waves show similar frequency response as in the Drude medium (Figure 4.14a). Note that, the reflected power shows also similar behavior

when the plasma frequencies are 14.50 GHz, but the range is not given in this figure. The transmitted power for both waves shows the complementary behavior of the reflected power.

The reflected and transmitted powers of TE and TM waves for the cold plasma medium model as a function of the slab thickness at the incidence angle of 30° are illustrated in Figure 4.18. The slab thickness is changed from $\lambda/5$ (1.0 cm) to λ (5.0 cm). The reflected and transmitted powers for both waves periodically oscillate when the slab thickness changes. This oscillation is not visible in the figure when the plasma frequencies are $f_{ep} = f_{mp} = 8.50$ GHz. The reflected power oscillates between the values of 0.41–0.412 for TE wave and 0.3075–0.3095 for TM wave; and the transmitted power oscillate between the values of 0.588–0.59 for TE wave and 0.6905–0.6925 for TM wave. The reflected power becomes zero for TM wave and it becomes nearly zero for TE wave periodically. On the other hand, the transmitted power becomes unity for TM wave and it becomes almost unity for TE wave periodically. For the given parameters, Figure 4.18 strongly recommends that possibility of manufacturing anti-reflection and/or total-transmission coatings and/or filters by tuning the fraction of the thickness of DNS. Thus, DNS can be used in layered structures for manufacturing the mentioned coatings and/or filters. In many studies, these coating and filters are obtained using more than one slab. Here, we obtained these coatings and filters using one DNG slab. Thus, size reduction for the layer numbers has been realized in this study.

TE wave   TM wave
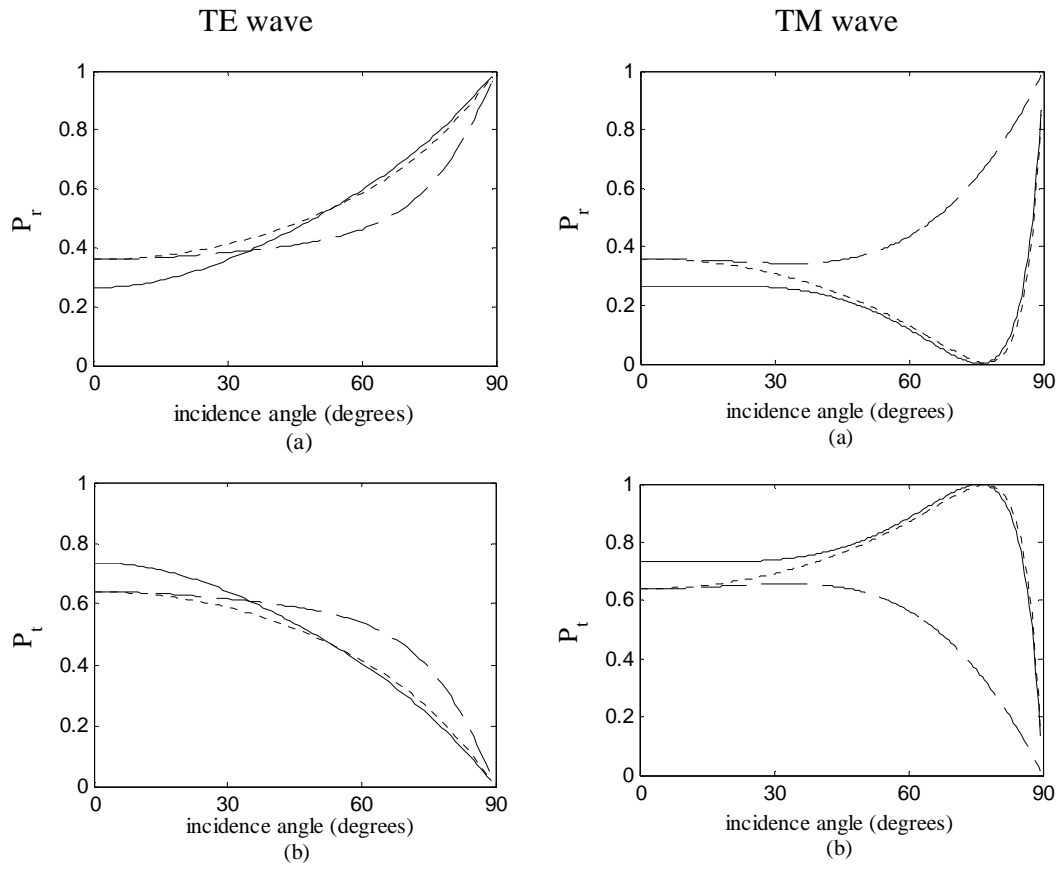
Figure 4.16: The reflected and transmitted powers of TE and TM waves for the cold plasma medium model versus the incidence angle. Dotted line corresponds to $f_{ep} = f_{mp} = 8.50$ GHz; solid line to $f_{ep} = 14.50$ GHz, $f_{mp} = 8.5$ GHz; and dashed line to $f_{ep} = f_{mp} = 14.50$ GHz.
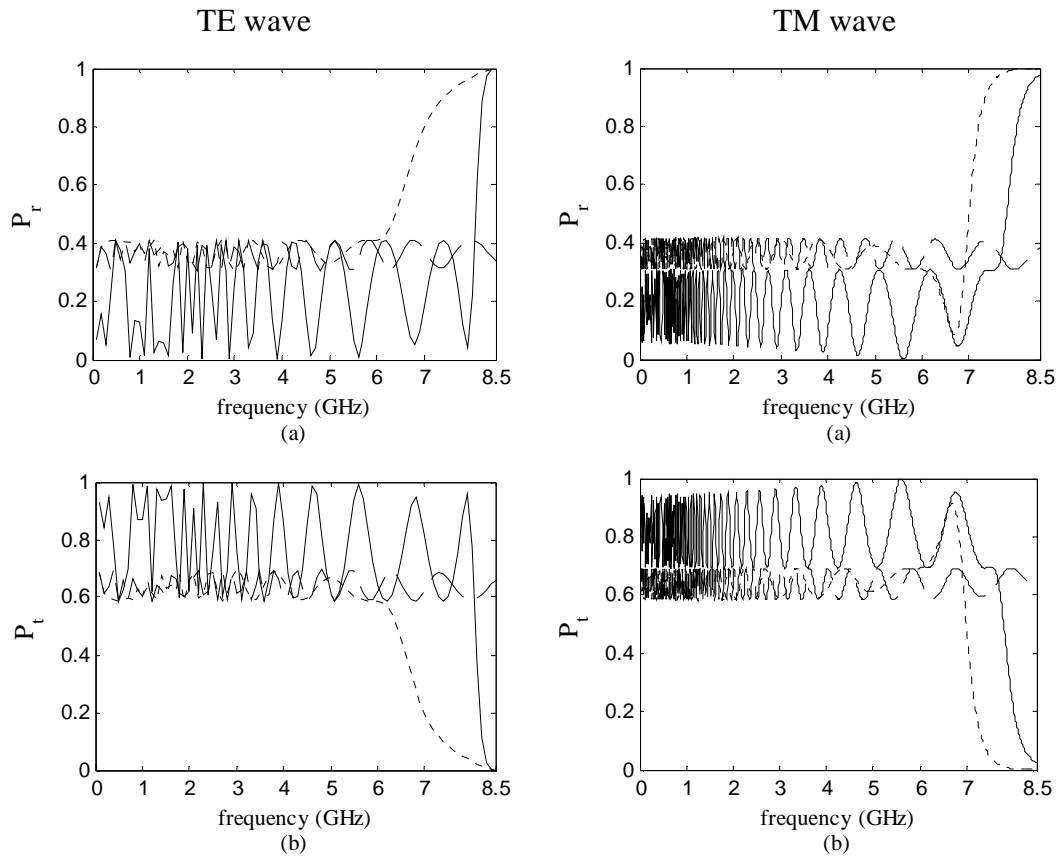
Figure 4.17: The reflected and transmitted powers of TE and TM waves for the cold plasma medium model against the frequency. Dotted line stands for $f_{ep} = f_{mp} = 8.50$ GHz; solid line for $f_{ep} = 14.50$ GHz, $f_{mp} = 8.5$ GHz; and dashed line for $f_{ep} = f_{mp} = 14.50$ GHz.

TE wave
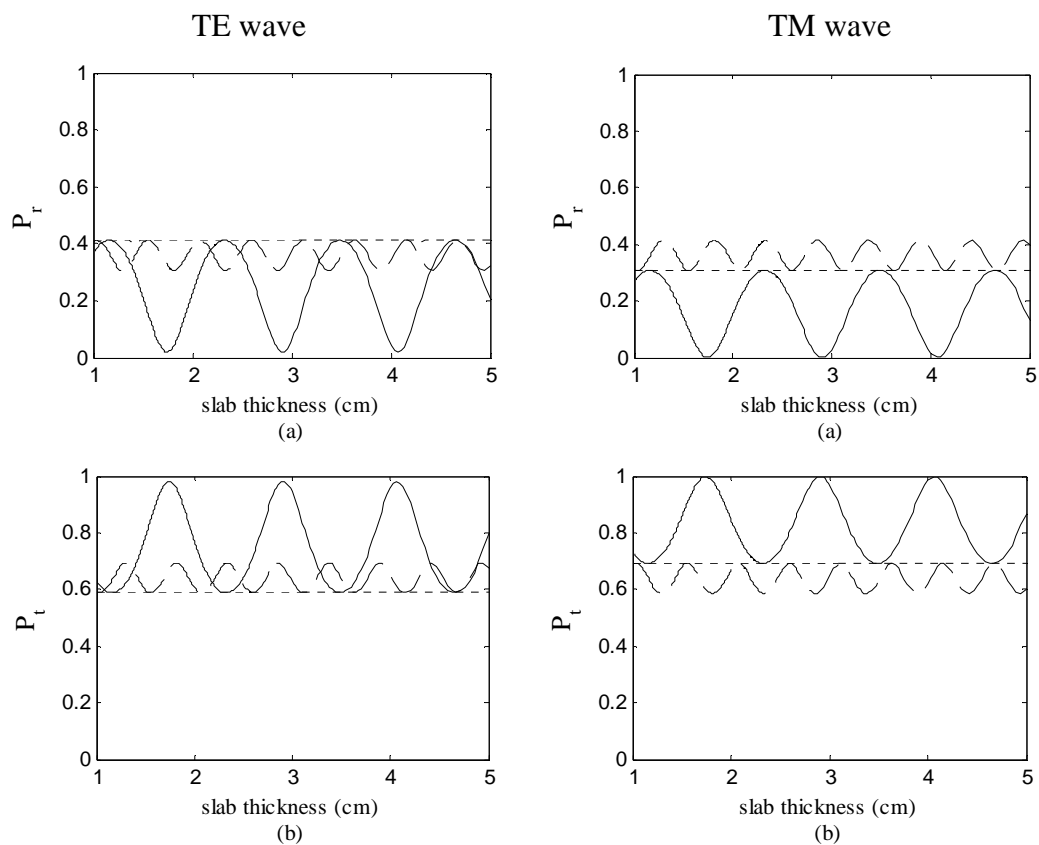
TM wave

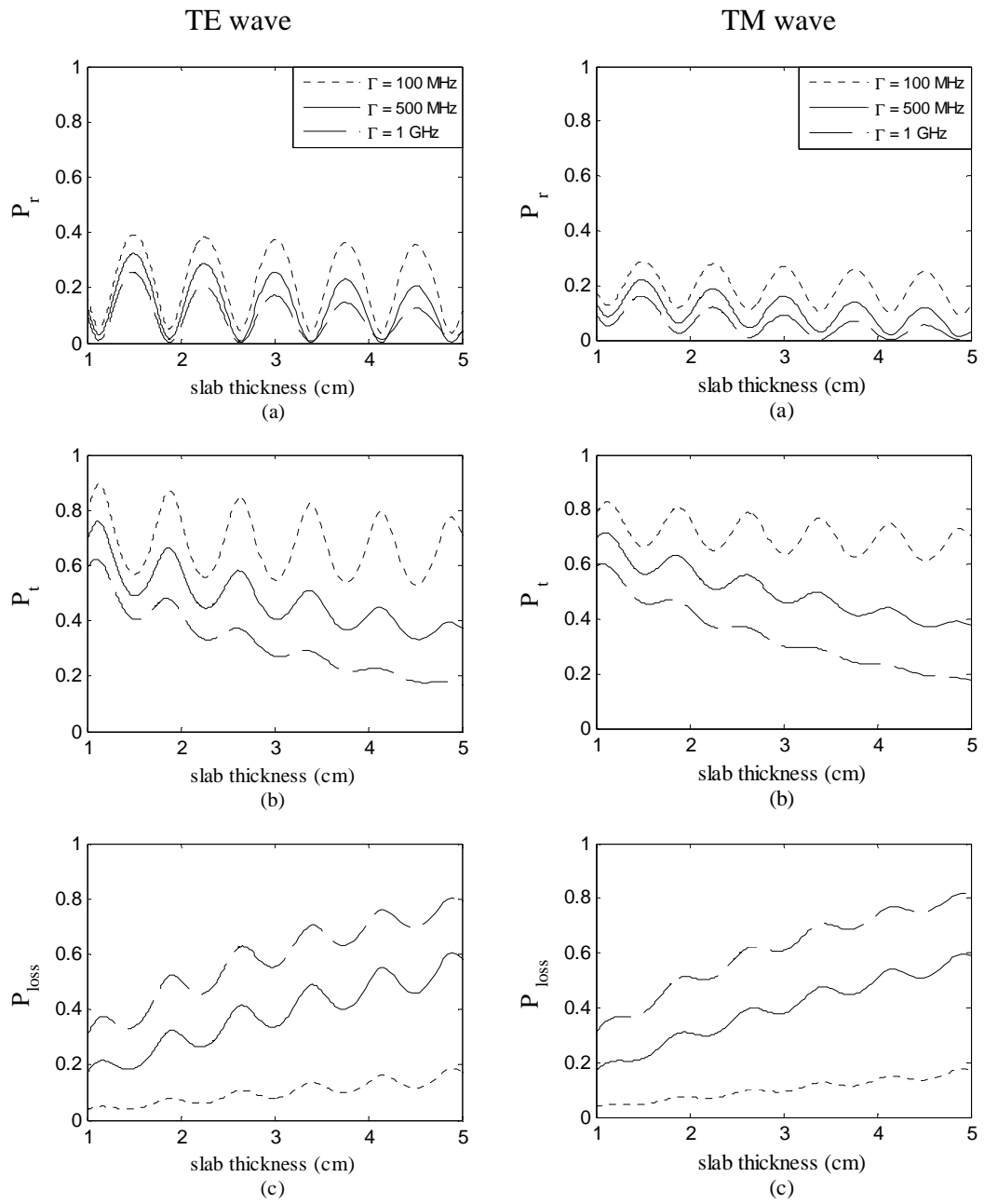Figure 4.18: The reflected and transmitted powers of TE and TM waves for the cold plasma medium model as a function of the slab thickness. Dotted line corresponds to $f_{ep} = f_{mp} = 8.50$ GHz; solid line to $f_{ep} = 14.50$ GHz, $f_{mp} = 8.5$ GHz; and dashed line to $f_{ep} = f_{mp} = 14.50$ GHz.

4.6 Numerical Simulations

In this section, DNG metamaterial is used to demonstrate some simulations of two semi infinite media (DPS and DNG media) and single slab of DNG material. These are used especially to create perfect/flat lenses, refractors, surface plasmon, novel microwave antennas, resonators, waveguides, and etc [6], [13], [42−88]. Here, we deal with the application of flat lens. Such a flat lens is not possible with conventional microwave substrates or materials. The concept of flat lens is based on Snell's Law of Refraction and is depicted in Figure 2.3 and Figure 2.4. If a point source is placed in DPS medium, an image of the point source will be reproduced in DNG medium. DNG medium for the flat lens is realized using the commercial software package, ANSOFT's High Frequency Structure Simulator (HFSS), based on finite-element method (FEM) with an effective medium approach. In this approach, the substrate of DNG medium is assigned a constant negative value of permittivity and permeability in the simulations.

4.6.1 Simulation of DPS and DNG Media

To realize the simulation, two DPS and DNG media are created in HFSS. Figure 4.19 shows the model setup used for the simulation. A voltage point source is placed in the middle of the DPS medium and it is expected that its image will occur in the DNG. The refractive index of DNG will be the negative of the DPS according to the effective medium approach. In the first example, the refractive index of DPS medium is $n = 1.0$, while the DNG medium has a negative refractive index of $n = -0.995$, where $n = \pm\sqrt{\varepsilon_r \mu_r}$. DPS medium is created with a relative permittivity of 1.0 and a relative permeability of 1.0, while DNG medium with a relative permittivity of −1.1 and relative permeability of –0.9. The difference in the numerical values between the DPS and DNG is to create an impedance mismatch to prevent the formation of constructive interference at the interface. After performing the excitation and analysis setup, the simulation can be done to see plots of the electric field and

79

Poynting vector. They can be seen in Figure 4.20 and Figure 4.21. Both figures confirm that the flat lens works. Since the DNG medium supports a backward wave, the field in this region appears to be moving backwards as it is seen from Figure 4.20. In addition, Poynting vector is in the opposite direction of the propagation in DNG medium as it seen from Figure 4.21.
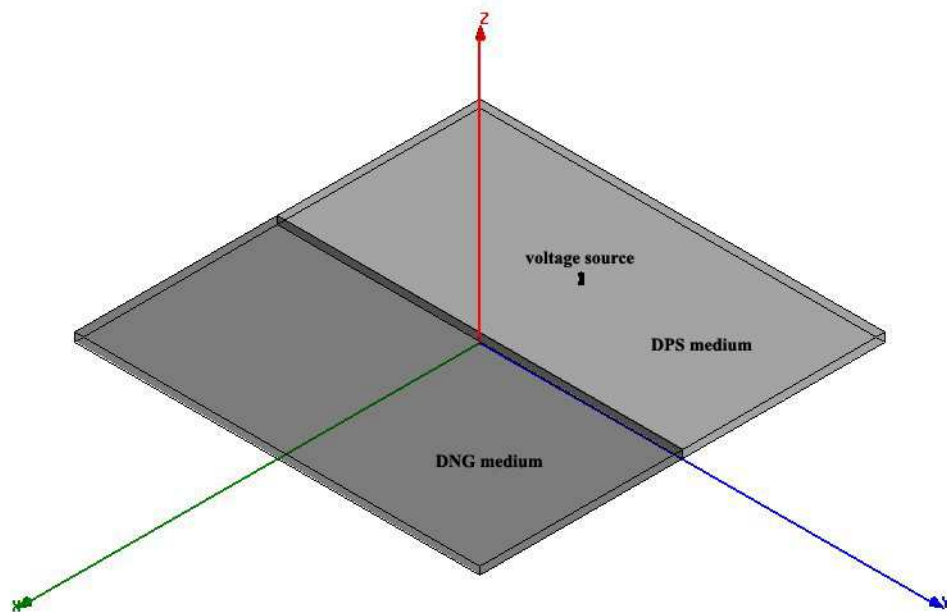
Figure 4.19: Simulation model of semi infinite DPS and DNG media.
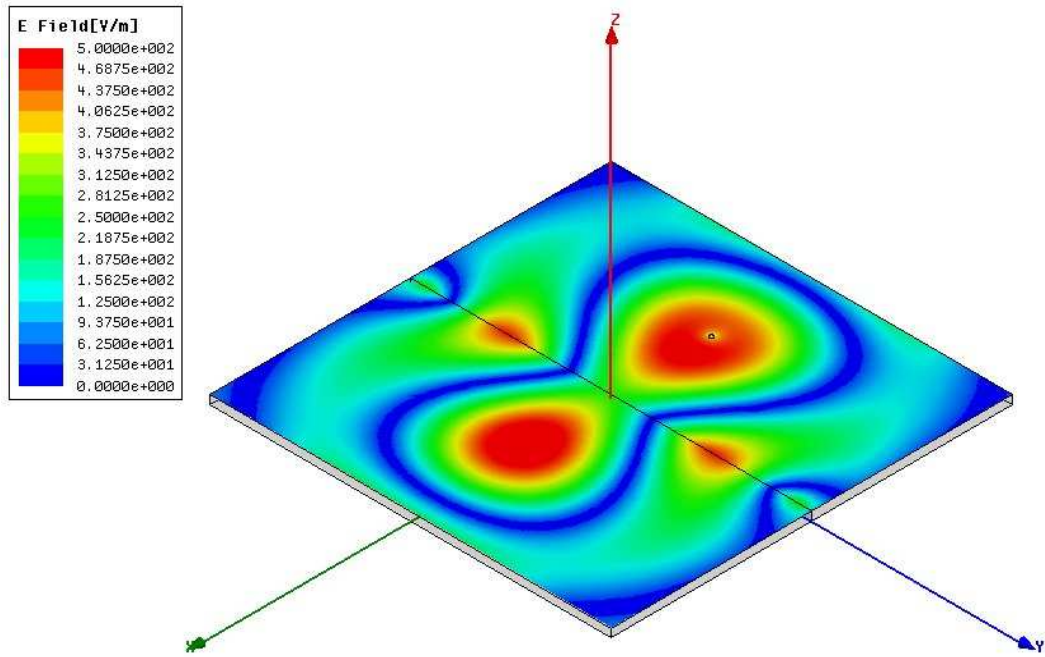
Figure 4.20: Magnitude of the electric field for the first example. ($n_{\mathrm{DPS}} = 1.0$ and $n_{\mathrm{DNG}} = -0.995$)
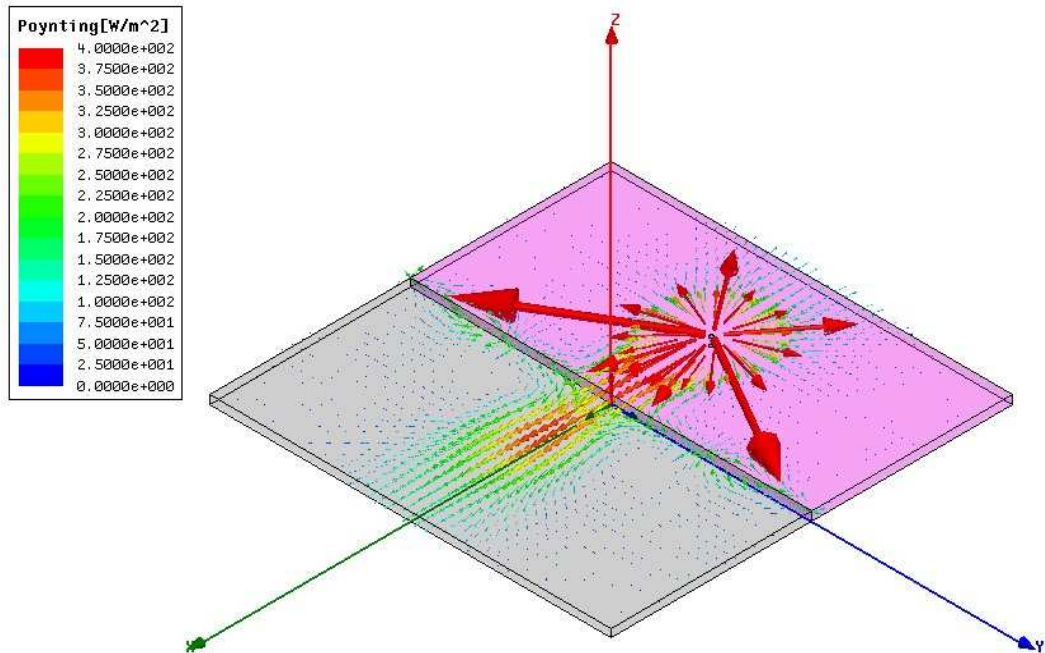
Figure 4.21: Poynting vector for the first example. ($n_{\mathrm{DPS}} = 1.0$ and $n_{\mathrm{DNG}} = -0.995$)

In the second example, another flat lens application is provided using Drude medium parameters given in Chapter 3. The following parameters are used to obtain the permittivity and permeability [57]: $\varepsilon_r = -3.5032$, $\mu_r = -1.0014$ for DNG medium and $\varepsilon_r = 9.0$, $\mu_r = 1.0$ (mica-glass) for DPS medium. Using the same procedure as in the previous example the electric field and Poynting vector can be plotted as in Figure 4.22 and Figure 4.23, respectively. Both figures validate that the flat lens works for the given parameters. From Figure 4.22, it can be seen that DNG medium produces a backward wave and the field is moving backwards. From Figure 4.23, Poynting vector is in the opposite direction of the propagation in DNG medium.

In the third example, the application of DPS and DNG media to the parabolic wave refractor is presented. The parameters of DNG medium is selected to be the same with the previous example. DPS medium is assigned as the vacuum with $\varepsilon_r = 1.0$, $\mu_r = 1.0$. By using the same procedure as in the first example the electric field and Poynting vector can be plotted and they are in Figure 4.24 and Figure 4.25, respectively. As it is seen from Figure 4.24, the electric field in DPS medium is in the circular shape. It transmits to the DNG medium and propagates in the form of parabolic shape. Thus, this structure can be designed and used as a parabolic wave refractor. Note that, Poynting vector is again in the opposite direction of the propagation as in the previous examples.
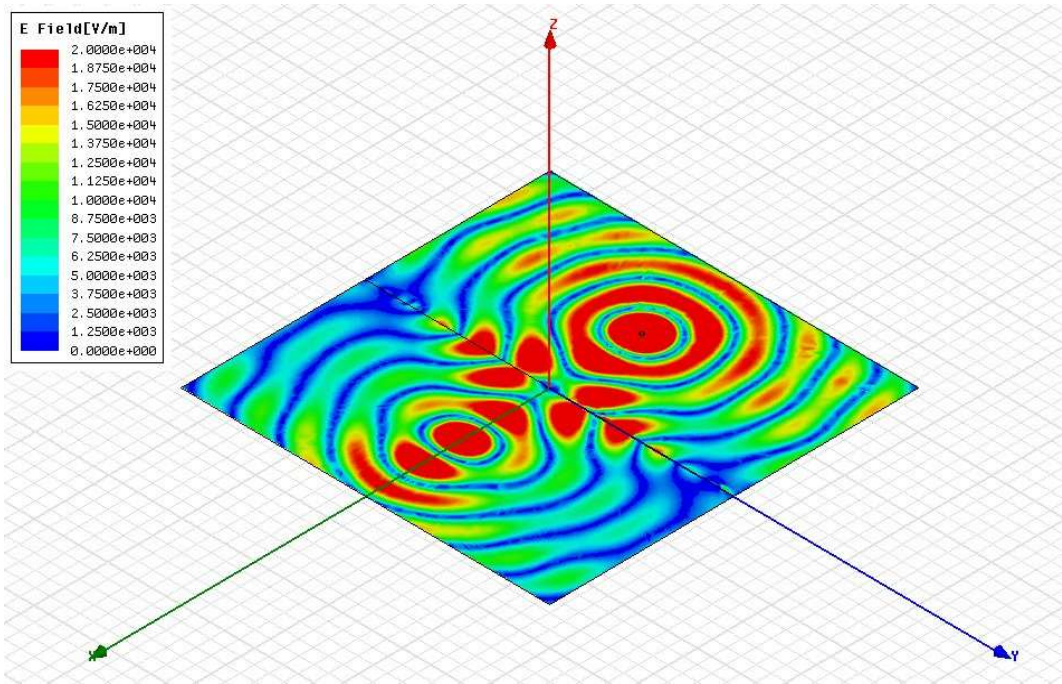
Figure 4.22: Magnitude of the electric field for the second example. ($\varepsilon_r = 9.0$, $\mu_r = 1.0$ for DPS medium and $\varepsilon_r = -3.5032$, $\mu_r = -1.0014$ for DNG medium)
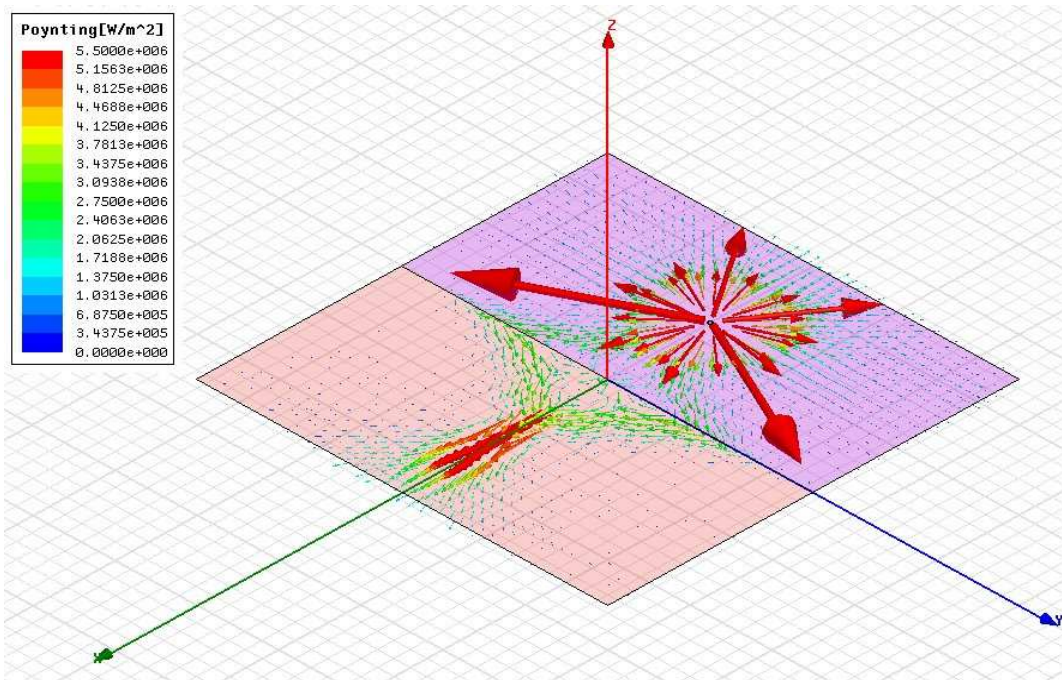
Figure 4.23: Poynting vector for the second example. ($\varepsilon_r = 9.0$, $\mu_r = 1.0$ for DPS medium and $\varepsilon_r = -3.5032$, $\mu_r = -1.0014$ for DNG medium)
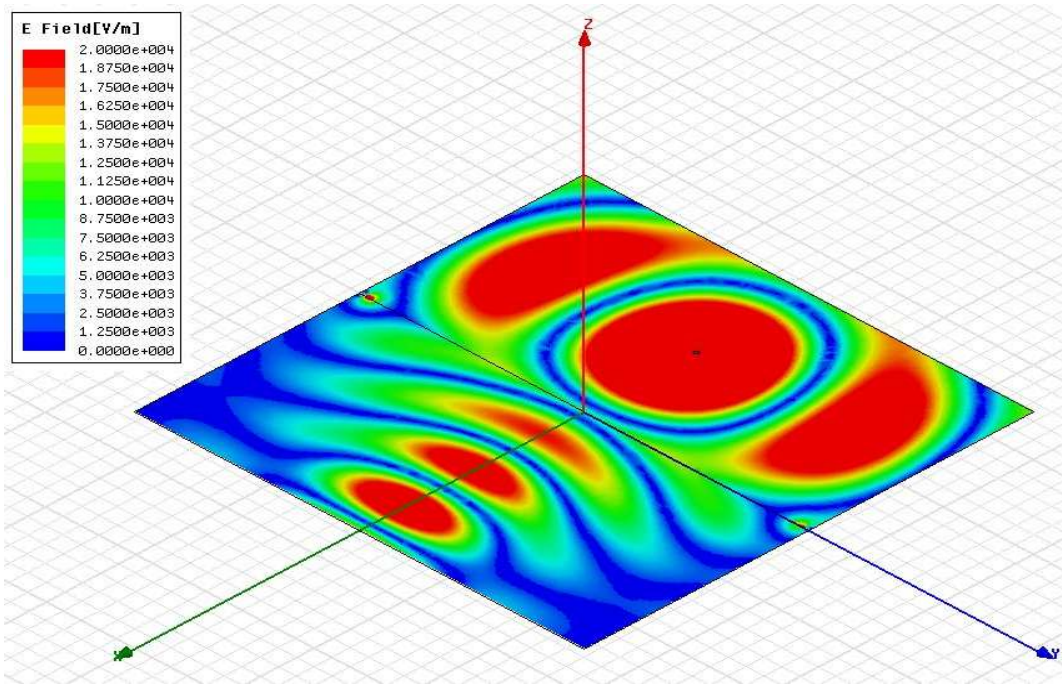
Figure 4.24: Magnitude of the electric field for the third example. ($\varepsilon_r = 1.0$, $\mu_r = 1.0$ for DPS medium and $\varepsilon_r = -3.5032$, $\mu_r = -1.0014$ for DNG medium)
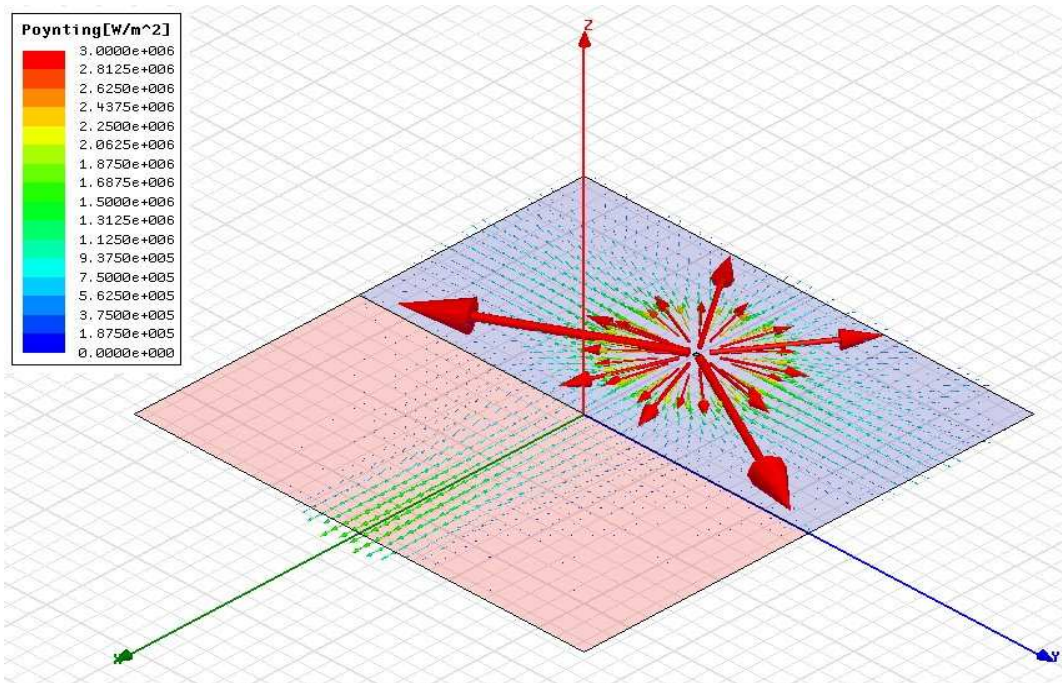
Figure 4.25: Poynting vector for the third example. ($\varepsilon_r = 1.0$, $\mu_r = 1.0$ for DPS medium and $\varepsilon_r = -3.5032$, $\mu_r = -1.0014$ for DNG medium)

4.6.2 Simulation of Single DNS

To simulate the single DNS, the process outlined in the previous section is used. Figure 4.26 shows the geometry of the simulation. DNG medium is assigned using the same parameters as in [57], $\varepsilon_r = -3.5032$, $\mu_r = -1.0014$. DPS-I is the mica-glass with $\varepsilon_r = 9.0$, $\mu_r = 1.0$, and DPS-II is the vacuum with $\varepsilon_r = 1.0$, $\mu_r = 1.0$. The electric field is given in Figure 4.27. As it is seen from this figure, there is backward wave propagation in DNS. In addition, the second image of the voltage source is at the middle of the third medium (DPS-II). But, the first image of the voltage source is not at the middle of the DNS. It shifts toward the DPS-I and DNS interface. This is caused by interference and impedance mismatch at the interface. If the effective medium approach is used to simulate single DNS, the first and the second images will be at the middle of the DNS and DPS-II, respectively, as it is seen from Figure 4.28. Note that, DPS-I and DPS-II are selected to be the vacuum, and DNS is created with $\varepsilon_r = -1.1$ and $\mu_r = -0.9$, in the second simulation.
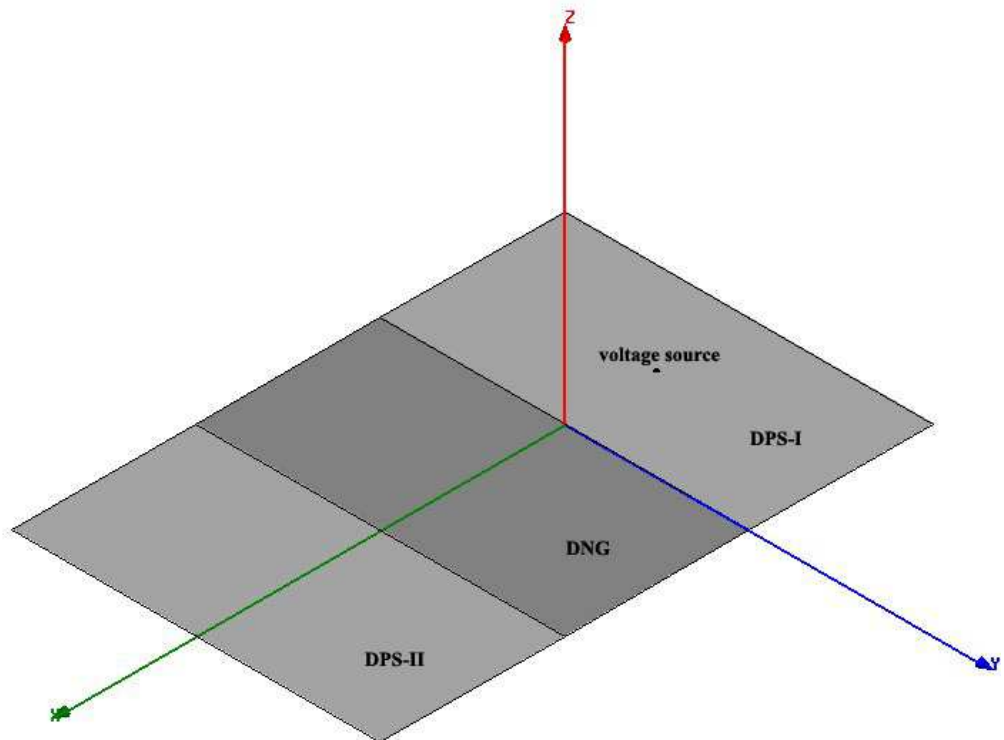
Figure 4.26: Geometry of DNS used in this simulation.
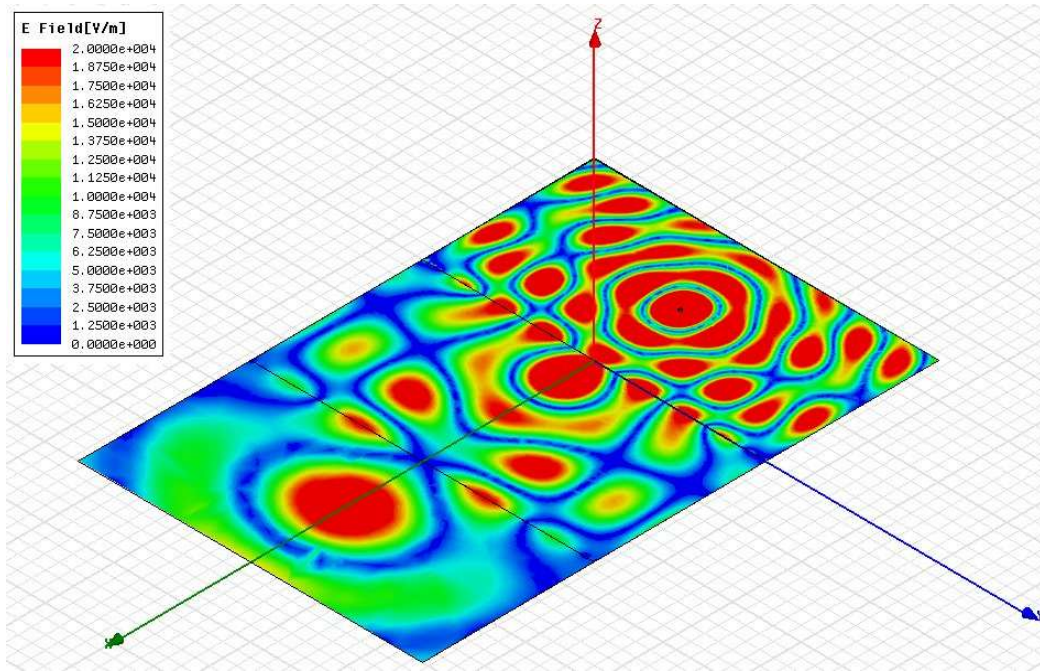
Figure 4.27: Magnitude of the electric field for DNS simulation without using effective medium approach. ($\varepsilon_r = 9.0$, $\mu_r = 1.0$ for DPS-I, $\varepsilon_r = -3.5032$, $\mu_r = -1.0014$. for DNG medium, and $\varepsilon_r = 1.0$, $\mu_r = 1.0$ for DPS-II.)
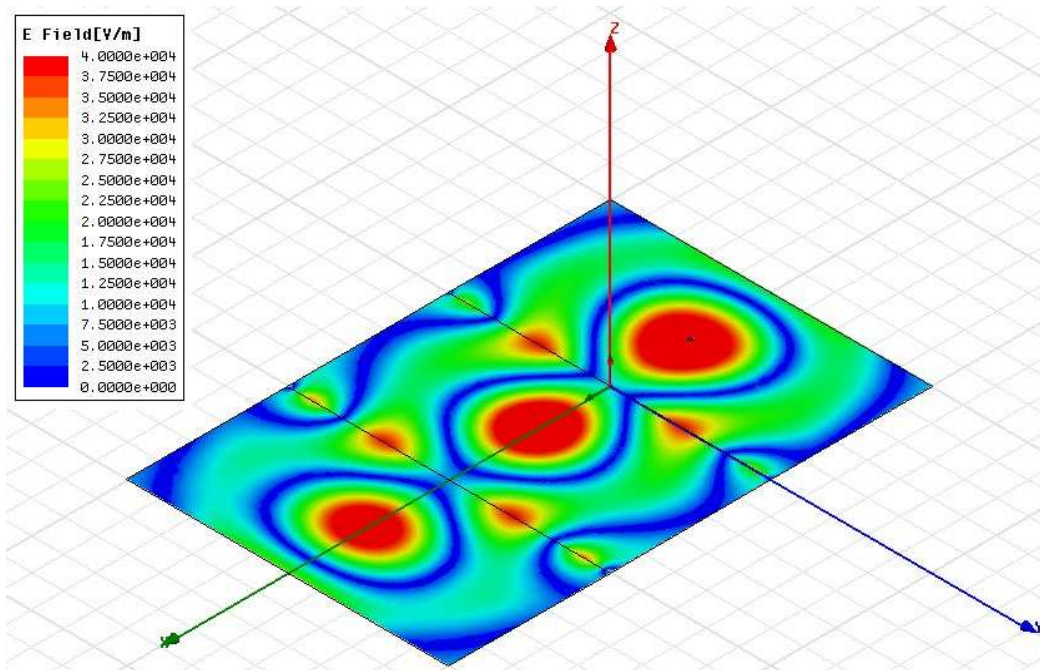
Figure 4.28: Magnitude of the electric field for DNS simulation with using effective medium approach. ($\varepsilon_r = 9.0$, $\mu_r = 1.0$ for DPS-I, $\varepsilon_r = -3.5032$, $\mu_r = -1.0014$. for DNG medium, and $\varepsilon_r = 1.0$, $\mu_r = 1.0$ for DPS-II.)

4.7 Summary and Discussion

In summary, this chapter has discussed the fundamental properties of electromagnetic wave propagation in the presence of DNG metamaterial. It was seen by plane wave analysis, the reflection and transmission coefficients can be derived by means of the recursive method and by using right- and left-hand rules with Maxwell's equations. These coefficients are formulated for both normal and oblique incidences. The effects of the structure parameters (such as permittivity and permeability), the incidence angle and the frequency on the reflection and transmission coefficients are also investigated numerically. Analysis of the double negative slab is also given in this chapter. DNS is characterized by the hypothetical and frequency dispersive media, in order. Then, the powers of carried by the wave are computed and examined. In the numerical results, the effect of the damping frequency on the powers for both TE and TM waves is presented when the incidence angle, the frequency and the slab thickness change. It is observed that, the behaviors of the powers are very sensitive to the varying frequency when the medium have frequency-dependent permittivity and permeability. In practice, an infinite number of surface wave modes can exist on the DNG slab medium and they do not carry the power away in both transverse and longitudinal directions. Simply, the wave cannot propagate very far into a metal, but metals are not inert to the wave. It is possible for the wave to be existed at the surface of a metal. DNG materials support a host of surface modes commonly observed at metal surfaces. In the physical system, the surface modes are easily excited on the interface. The surface modes, however, are negligible on the surface in some cases due to the absorption inside the slab. They are highly dependent on and very sensitive to the material parameters. The surface mode, on the other hand, is sometimes unaffected and they can be removed if the top and bottom interfaces are coated with a thin PEC layer since the PEC-vacuum interface does not support a surface mode. In this work, the material parameters are arranged to allow the surface modes are negligible to not impress the scattering characteristics (reflection, transmission, and etc.) of the frequency dispersive and lossy DNG slab. In addition to the surface wave modes, we can talk about the relation between the scattering characteristics of DNG slab and Fabry-Perot condition/resonance. If the Fabry-Perot condition is fulfilled, the unwanted

reflections can be reduced and/or eliminated. Actually, the reflections can be nearly cancelled out and it can be achieved to the total transmission. The maximum and minimum transmissions occur if the transmitted waves are in phase and out-of-phase, respectively. Whether the multiply-reflected waves are in-phase or not, depends on the wavelength of the wave, the angle of the wave, the thickness of the slab and the refractive index of the material. The Fabry-Perot resonances can be observed from where the transmission power has maximum and minimum values. In addition to these, the results show that the manufacturing of anti-reflection and/or total-transmission coatings and/or filters is achievable by using the suitable design process. Furthermore, the combination of DPS and DNG media are simulated to show the perfect/flat lens and the parabolic wave refractor applications. It can be said that these combinations can be used to manufacture the new lenses and refractors. At last, these results can be used to analyze, fabricate, and integrate the metamaterials in various structures.

CHAPTER 5

DESIGN AND ANALYSIS OF STRATIFIED STRUCTURES

5.1 Introduction

This chapter will present the analysis of electromagnetic wave interaction with the multilayer media comprised of pure DNG metamaterials and mixed DNG-DPS slabs. Theoretically, the multilayer structure is formed from N pieces slabs with different material properties and thicknesses. The incident electric field is assumed a monochromatic plane wave with any arbitrary polarization. Transfer matrix method will be used in the analysis. After obtaining the electric and magnetic fields both inside and outside the multilayer structure and imposing the boundary conditions, the transfer matrix can be obtained. Note that, the elements of the transfer matrix are expressed as a function of the incidence angle, the structure parameters, the thickness of each stack, and the frequency. Then, the incident, reflected, and transmitted powers can easily be determined to observe their features. Thus, the scattering characteristics of the multilayer structure for the electromagnetic wave with any arbitrary polarization will be computed and presented in numerical results. Several applications of DNG metamaterials and mixed DNG-DPS slabs will also be performed and the results of them will be discussed.

5.2 Theoretical Modeling and Analysis

A DNG medium has interesting properties when it is composed as the stratified DNG stacks embedded between two DPS media. The paired DNG-DPS layers are also interesting and they will be explained later. In this study, we consider any arbitrary polarization plane electromagnetic incident electric field from free-space that is encountering the dielectric-DNG stack interface. The stratified DNG stacks considered in this paper is composed of N DNG layers with different material properties and thicknesses as shown in Figure 5.1. In the analysis, exp(*jωt*) time dependence is assumed and suppressed throughout this work.
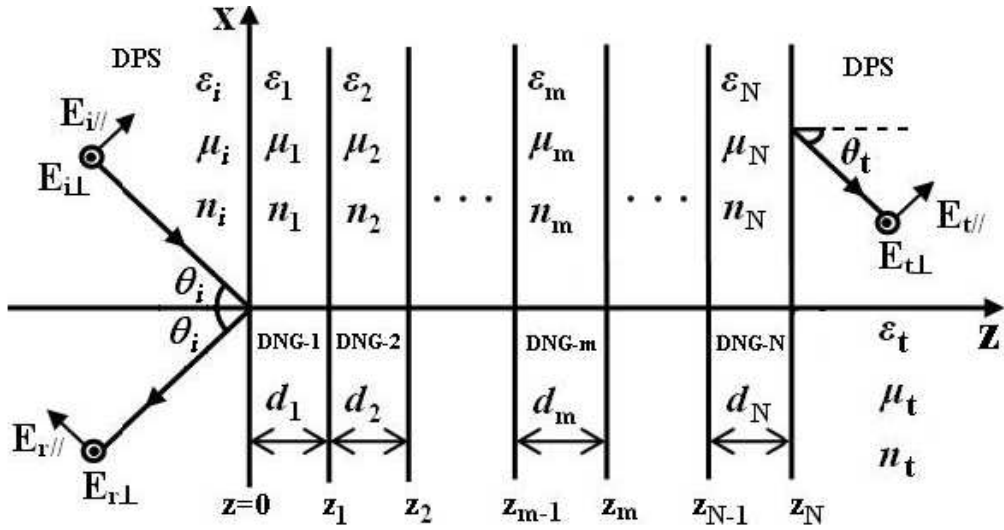
Figure 5.1: The configuration of the stratified DNG stacks.

Referring to Figure 5.1, the incident electric field with any arbitrary polarization can be written (by using the theory outlined in the previous chapter):

$$\boldsymbol{E_i} = [E_{i//}(\cos\theta_i \boldsymbol{a}_x + \sin\theta_i \boldsymbol{a}_z) + E_{i\perp}\boldsymbol{a}_y] \cdot \exp[-j(-k_{ix}x + k_{iz}z)] \tag{5.1}$$

where θ_i is the angle of the incidence, k_{ix} ($= k_i \sin \theta_i$) and k_{iz} ($= k_i \cos \theta_i$) are the x- and z- components of the wave number k_i ($= \omega\sqrt{\mu_i \varepsilon_i}$). Note that, the subscripts // and $\perp$ refer to the parallel and perpendicular components of the electric field vector, respectively. According to the incident electric field given in Equation (5.1), the reflected ($\boldsymbol{E}_r$) and the transmitted ($\boldsymbol{E}_t$) electric fields can be expressed as:

$$\boldsymbol{E_r} = [E_{r//}(\cos\theta_i \boldsymbol{a}_x - \sin\theta_i \boldsymbol{a}_z) + E_{r\perp}\boldsymbol{a}_y] \cdot \exp[-j(-k_{ix}x - k_{iz}z)] \tag{5.2}$$

$$\boldsymbol{E_t} = [E_{t//}(\cos\theta_t \boldsymbol{a}_x + \sin\theta_t \boldsymbol{a}_z) + E_{t\perp}\boldsymbol{a}_y] \cdot \exp[-j(-k_{tx}x + k_{tz}z)] \tag{5.3}$$

where θ_t is the transmission angle, k_t ($= \omega\sqrt{\mu_t \varepsilon_t}$) is the wave number of the transmitted medium, $k_{tx} = k_t \sin \theta_t$ and $k_{tz} = k_t \cos \theta_t$ are the x- and z- components of the wave number k_t.

The electric field in any stack reflects back and transmits to another stack upon reaching the transmitted medium. Therefore, in the mth DNG stack there are two waves, one propagating toward the right interface and the other one propagating toward the left interface. Thus, in the mth DNG stack, the total electric field can be stated as:

$$\begin{aligned}\boldsymbol{E_m} &= [A_{//}(\cos\theta_m \boldsymbol{a}_x + \sin\theta_m \boldsymbol{a}_z) + A_{\perp}\boldsymbol{a}_y] \cdot \exp[-j(-k_{mx}x + k_{mz}z)] \\ &+ [B_{//}(\cos\theta_m \boldsymbol{a}_x + \sin\theta_m \boldsymbol{a}_z) + B_{\perp}\boldsymbol{a}_y] \cdot \exp[-j(-k_{mx}x - k_{mz}z)]\end{aligned} \tag{5.4}$$

where $A_{//}$, $A_{\perp}$, $B_{//}$, and $B_{\perp}$ are the amplitudes of the electric fields inside the mth DNG stack, θ_m is the refracted angle, k_m is the wave number of the mth DNG stack,

$k_{mx} = k_m \sin \theta_m$ and $k_{mz} = k_m \cos \theta_m$ are the x- and z-components of the wave number k_m. In all representations, the subscripts i, m, and t stand for the incident medium, the mth DNG stack, and the transmitted medium, respectively. Note that, the magnetic fields inside and outside the DNG stacks can be found easily using the right- and left-hand procedure with Maxwell's equations and they are skipped here. In addition, the wave number of the mth DNG stack must be negative and it can be given as:

$$k_m = -\omega\sqrt{\mu_m \varepsilon_m} \tag{5.5}$$

To solve the general problem for the incident, reflected, and transmitted power for the stratified DNG stacks shown in Figure 5.1, it is necessary to investigate the interfaces between DPS-DNG media and two DNG media. Thus, imposing the boundary conditions at the interfaces $z = 0$, $z = z_m$ (m = 1, 2, 3, ……, N-1) and $z = z_N$, the relationships among the fields in all regions can be obtained by the transfer matrix $[U]$ which is expressed as:

$$\begin{bmatrix} E_{i\perp} \\ E_{r\perp} \\ E_{i//} \\ E_{r//} \end{bmatrix} = [U]\begin{bmatrix} E_{t\perp} \\ E_{t//} \end{bmatrix} = \begin{bmatrix} u_{11} \ u_{12} \\ u_{21} \ u_{22} \\ u_{31} \ u_{32} \\ u_{41} \ u_{42} \end{bmatrix}\begin{bmatrix} E_{t\perp} \\ E_{t//} \end{bmatrix} \tag{5.6}$$

where $[U] = [A] [B_1] [B_2] [B_3]\cdots[B_m]\cdots[B_{N-1}] [C]$. Note that, $[A]$ and $[B_m]$ are both square matrices of order 4, $[C]$ is a 4×2 matrix and $[U]$ is in the form of 4×2 matrix. The elements of $[A]$, $[B_m]$, and $[C]$ are expressed as a function of the incidence angle, the structure parameters, the thickness of each DNG stack, and the frequency. Then, according to Equation (5.6), we can write the reflected and the transmitted electric fields in terms of the incident electric field as:

$$E_{r\perp} = \frac{(u_{21}\,u_{32} - u_{22}\,u_{31})E_{i\perp} + (u_{11}\,u_{22} - u_{12}\,u_{21})E_{i//}}{(u_{11}\,u_{32} - u_{12}\,u_{31})} \qquad (5.7)$$

$$E_{r//} = \frac{(u_{32}\,u_{41} - u_{31}\,u_{42})E_{i\perp} + (u_{11}\,u_{42} - u_{12}\,u_{41})E_{i//}}{(u_{11}\,u_{32} - u_{12}\,u_{31})} \qquad (5.8)$$

$$E_{t\perp} = \frac{(u_{32})E_{i\perp} - (u_{12})E_{i//}}{(u_{11}\,u_{32} - u_{12}\,u_{31})} \qquad (5.9)$$

$$E_{t//} = \frac{-[(u_{31})E_{i\perp} - (u_{11})E_{i//}]}{(u_{11}\,u_{32} - u_{12}\,u_{31})} \qquad (5.10)$$

where u_{ab} (a = 1, 2, 3, 4; b = 1, 2) are the elements of the 4×2 transfer matrix $[U]$.

Now, the z-component of the incident, reflected, and transmitted powers can be represented as follows:

$$\left| \boldsymbol{P}_{iz} \right| = \left| \frac{k_{iz}}{2\mu_i}(E_{i\perp}^2 + E_{i//}^2) \right| \;,\; \left| \boldsymbol{P}_{rz} \right| = \left| \frac{k_{iz}}{2\mu_i}(E_{r\perp}^2 + E_{r//}^2) \right| \;,\; \text{and } \left| \boldsymbol{P}_{tz} \right| = \left| \frac{k_{tz}}{2\mu_t}(E_{t\perp}^2 + E_{t//}^2) \right| \quad (5.11)$$

The conservation of the power without loss for any arbitrary polarization is expressed as:

$$\frac{k_{iz}}{\mu_i} \cdot \left| (E_{i\perp}^2 + E_{i//}^2) \right| = \frac{k_{iz}}{\mu_i} \cdot \left| (E_{r\perp}^2 + E_{r//}^2) \right| + \frac{k_{tz}}{\mu_t} \cdot \left| (E_{t\perp}^2 + E_{t//}^2) \right| \qquad (5.12)$$

If one of the stacks is the lossy stack, Equation (5.12) has to be modified as:

$$\frac{k_{iz}}{\mu_i} \cdot \left| (E_{i\perp}^2 + E_{i//}^2) \right| - P_{loss} = \frac{k_{iz}}{\mu_i} \cdot \left| (E_{r\perp}^2 + E_{r//}^2) \right| + \frac{k_{tz}}{\mu_t} \cdot \left| (E_{t\perp}^2 + E_{t//}^2) \right| \qquad (5.13)$$

All formulations found above have to be modified when the stratified structure is the paired DNG-DPS layers embedded between two dielectric media. The multilayer structure is composed by alternating DNG and DPS layers with different material properties and thicknesses forming an N-tier structure as shown in Figure 5.2.
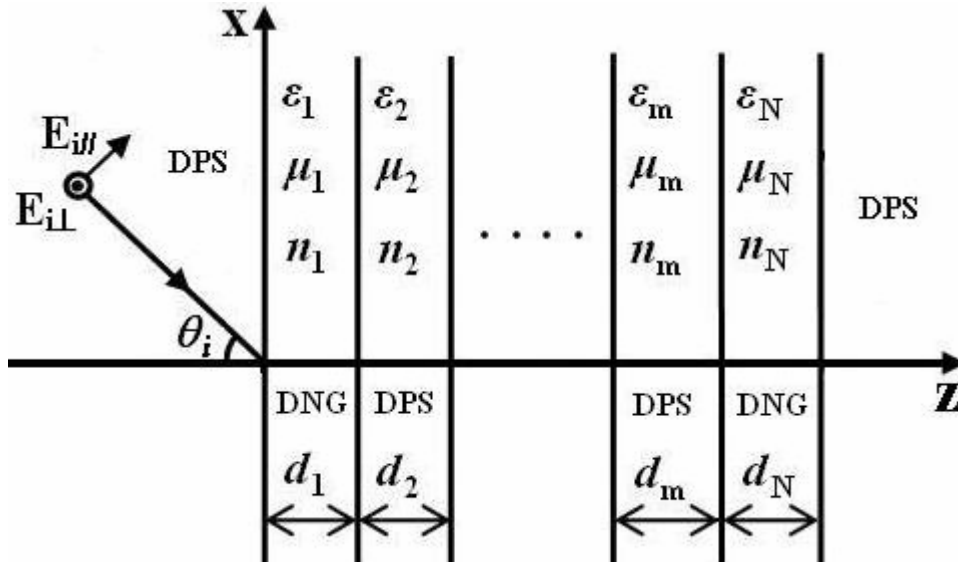
Figure 5.2: The geometry of the stratified DNG and DPS layers.

If the mth layer is DPS medium, the wave number k_m must be positive. On the other hand, the mth layer is DNG medium, the wave number k_m must be negative. Thus, the wave number k_m can be given as:

$$k_m = a\omega\sqrt{\mu_m\varepsilon_m}$$ (5.14)

where $a = +1$ for DPS layer, $a = -1$ for DNG layer. In addition, if the mth layer is DPS medium, the fields must be re-shaped using right-hand rule with Maxwell's equations. Thus, the equations from (5.6) to (5.10) must be revised using suitable sign for the phase of the fields with the help of Equation (5.14) and the theory clarified in Chapter 4. After that, some applications of stratified DNG layers and the combination of DNG-DPS layers will be provided in the subsequent sections.

5.3 Mirrors with DNG Slabs

Mirrors with DNG slabs are the special case of the DNG multilayer media. It is formed from DNG layers similar to dielectric or chiral mirrors. Here, we intend to construct the left-handed mirrors to observe their physical characteristics in the millimeter wave band. The DNG mirrors, shown in Figure 5.3, are comprised of an array of alternating DNG layers with two different refraction indices (n_A and n_B) and thicknesses (d_A and d_B) sandwiched between free spaces. The computations for the reflectance and transmittance have been presented to observe their characteristics in the millimeter wave band using the results obtained in Section 5.2, when the incident electric field is normalized to unity. Two mirrors are considered in the numerical results as: (ABA) and $(AB)^7A$. The mirror I has three DNG layers and the mirror II has fifteen DNG layers. In all figures, the solid lines correspond to mirror I and the dotted lines to mirror II. Furthermore, to verify the computations, the conservation of power, as a first method, is satisfied for all examples. As a second method, a transmission line equivalent is obtained for the structure given in Figure 5.3 [89].

Details of this method are given in Appendix. Both methods give the same numerical values for all computations. Thus, the results are verified by means of two methods.
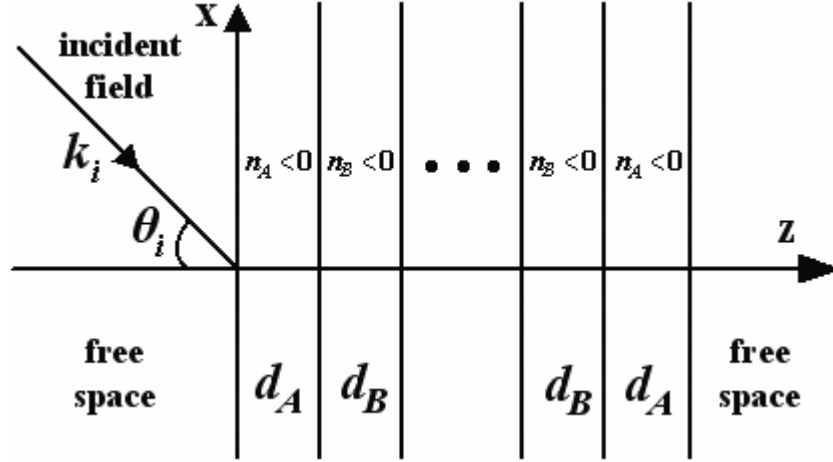
Figure 5.3: The geometry of the DNG mirrors.

In the first example, the reflectance and transmittance are calculated as a function of the frequency and the incidence angle when the incident electric field is a plane electromagnetic wave with the s-polarization ($E_{//} = 0$). The operation frequency is selected to be $f_o = 60$ GHz. The thicknesses d_A and d_B are arranged from $|n_A d_A| = \lambda_o/2$ and $|n_B d_B| = \lambda_o/4$ where λ_o is the wavelength in free-space at the operation frequency. The permittivity and permeability of the left-handed medium A and left-handed medium B are given as in [53]: $\varepsilon_A = -2\varepsilon_o$, $\mu_A = -3\mu_o$, $\varepsilon_B = -5\varepsilon_o$, and $\mu_B = -2\mu_o$.

Figure 5.4 points out the reflectance and transmittance as a function of the frequency at normal incidence. As it is seen, the frequency response of the reflectance and transmittance is periodic and symmetric according to the operation frequency. From Figure 5.4 (a), the mirror I transmits the most of the incident wave, because the transmittance is greater than the reflectance when the frequency changes. For the mirror II, reflectance and transmittance reach to unity at different frequency bands. Also, the mirror II acts as a full-reflection (band-pass) filter and a full-transmission (anti-reflection) filter at these frequency bands. At this point, it can be

said that, the mirror shows both filter characteristics at some frequency bands for increasing the layer numbers.
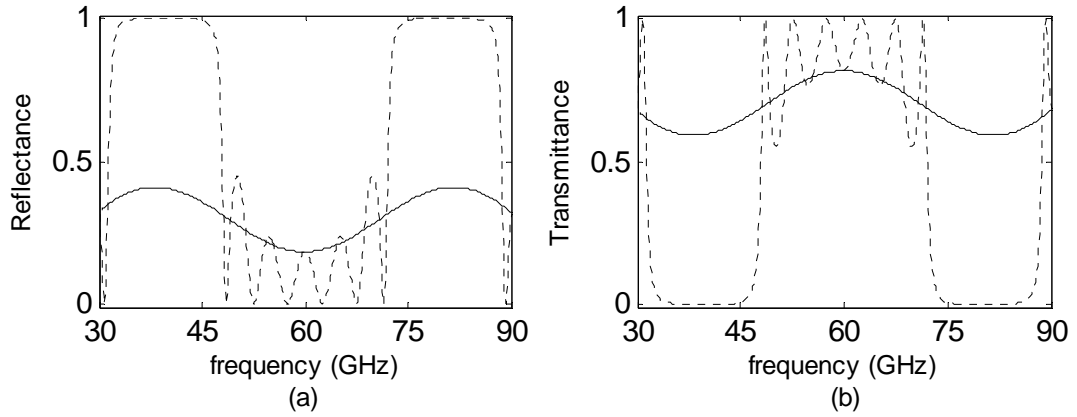
Figure 5.4: Reflectance and transmittance for the mirror I and mirror II as a function of the frequency at normal incidence. Solid lines correspond to mirror I and dotted lines to mirror II.

Figure 5.5 presents the reflectance and transmittance versus the incidence angle at the operation frequency. The transmittance is dominant between 0° and $\sim 50^o$ for the mirror I and between 0° and $\sim 60^o$ for the mirror II. The reflectance and transmittance for the mirror I show the monotonically increasing and decreasing behaviors with the incidence angle, respectively. Brewster angle occurs at the incidence angle of 47° for the mirror II which means there is no reflection at this angle. In addition, full reflection occurs at the incidence angle of 90°.

In the second example, mirror I and mirror II are again considered to calculate the reflectance and transmittance as a function of the frequency and the incidence angle for the s-polarization. The structure parameters and the operation frequency are the same with the first example except for the thicknesses of the left-handed layers. Here, the thicknesses d_A and d_B are assumed as $d_A = \lambda_o/2$ and $d_B = \lambda_o/4$, respectively.
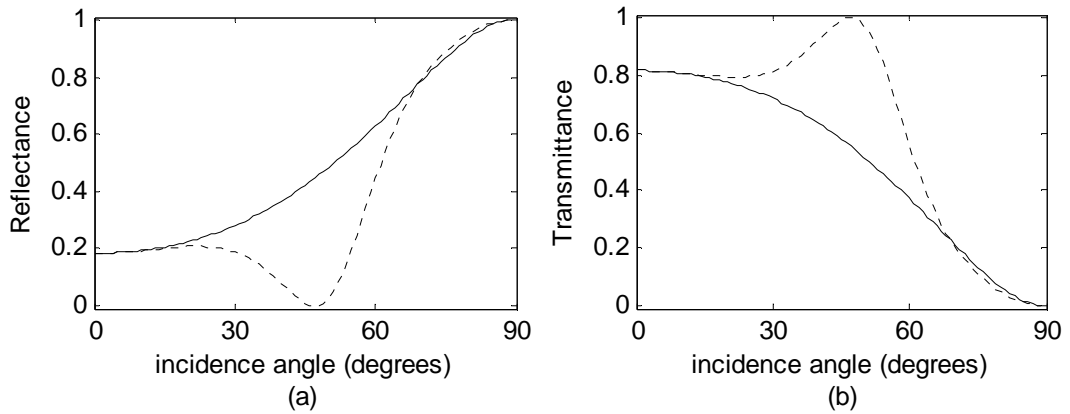
Figure 5.5: Reflectance and transmittance for the mirror I and mirror II versus the incidence angle at the operation frequency. Solid lines correspond to mirror I and dotted lines to mirror II.

Figure 5.6 displays the reflectance and transmittance against the frequency at normal incidence. As it is seen, the frequency response of $|R|$ and $|T|$ is not periodic and not symmetric according to the operation frequency. The mirror I again transmits the most of the incident wave as in the previous example. For the mirror II, $|R|$ and $|T|$ reach to unity at some frequency bands. Comparing Figure 5.4 and Figure 5.6, the frequency bands where $|R|$ becomes unity are not wide as in the first example, but they are more than two here. Also, the frequency bands where $|T|$ reaches to unity are more than one in this configuration. Thus, it can be said that, the mirror has more frequency bands where it shows a band-pass reflection filter and an anti-reflection filter behavior at the narrow ranges.

Figure 5.7 illustrates $|R|$ and $|T|$ against the incidence angle at the operation frequency. $|T|$ for the mirror I is dominant over a wide range of the incidence angle. But in the mirror II, $|R|$ is more dominant. In addition, $|R|$ is the unity and $|T|$ is zero up to 60°. After this angle, $|T|$ has a sharp peak and it reaches to unity at 77°. In turn, $|R|$ has a reverse sharp peak and it becomes zero at 77°. This means that Brewster angle occurs at the incidence angle of 77°.

98
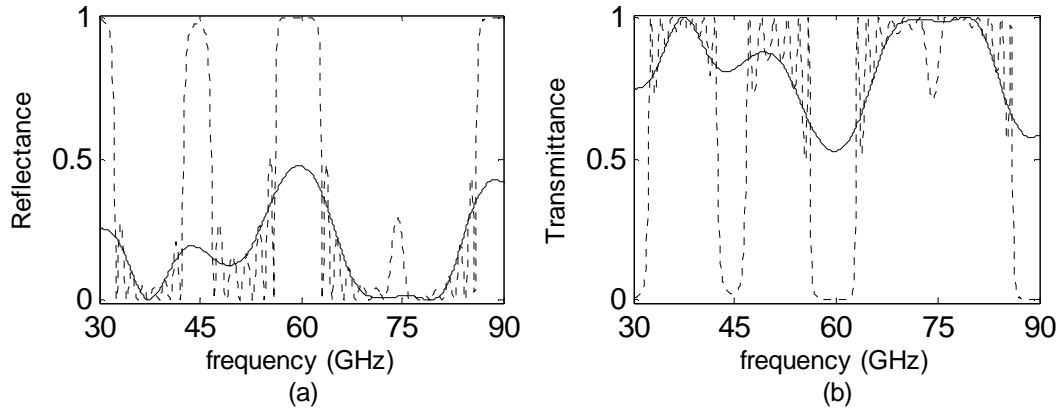
Figure 5.6: Reflectance and transmittance for the mirror I and mirror II against the frequency at normal incidence. Solid lines represent for mirror I and dotted lines for mirror II.
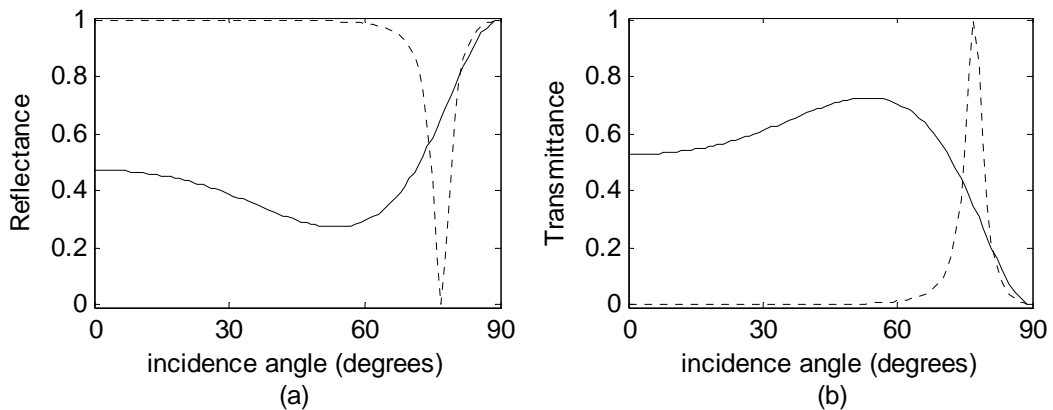
Figure 5.7: Reflectance and transmittance for the mirror I and mirror II against the incidence angle at the operation frequency. Solid lines represent for mirror I and dotted lines for mirror II.

It is confirmed that, similar numerical results given in Figure 5.4 – Figure 5.7 can easily be obtained for the incident wave with the p-polarization. Also, from the numerical results, we can say that high magnitude reflectance and transmittance in wide ranges can be obtained by arranging the layer numbers and thicknesses of the DNG mirrors. The DNG mirrors show the band-pass filter and the anti-reflection filter characteristics at some frequency regions within the millimeter wave band. The

results obtained here can be applied to design of the both filters at the millimeter wave, optical, and microwave regimes. Moreover, this study will make a foundation for future works and provide some insight into the filter application of LH materials.

5.4 High Reflection Coatings

In the previous section, the scattering characteristic of stratified structure formed by DNG metamaterials in the base of the low and high reflection coatings is investigated. Reflection and transmission filters applications are also shown in the millimeter wave frequency range. In this section, we intend to create a stratified structure comprised of DNG and DPS layer to obtain high reflection. High reflection coatings and all computations are based upon the theory explained in section 5.2. Generally quarter wave length thicknesses of alternately high and low refractive index materials are applied to the substrate to form a DNG-DPS multilayer stacks, as shown in Figure 5.2. By choosing materials of appropriate refractive indexes, the various reflected wave fronts can be made to interfere constructively to produce a highly efficient reflector. The peak reflectance value is dependent upon the ratio of the refractive indexes of the two materials, as well as the number of layer pairs. Increasing either increases the reflectance. The larger the ratio is, the wider the high reflectance region will be. Furthermore, the coatings are effective for both parallel and perpendicular polarization components, and can be designed for a wide angle of incidence range.

Propagation properties in multilayered structures consisting of metamaterial and dielectric layers are studied in [90]. A structure containing several identical pairs of alternating dielectric and metamaterial slabs is demonstrated to maximize the reflection for the high frequency range. It is found that for these metamaterial dielectric high reflection structures the pass band is larger and the effects of angle of incidence and polarization is less dominant as compared to the all dielectric structures. Moreover, these structures show no ripples and a monotonous quasi

symmetric rise in their transmittance to the left and to the right of central frequency is observed.

These structures are further studied to decrease the frequency range and to reduce the number of layers. In the computations, the incident electric field is assumed as the plane electromagnetic wave with the perpendicular polarization ($E_{//} = 0$). The operation frequency is selected to be $f_o = 10$ GHz. The thicknesses are arranged to become quarter wave length long at the operation frequency. In our configuration, seven DNG and DPS layers embedded in air are considered.

First of all, the frequency response of all dielectric structure with the high and low refractive indexes is shown. The permittivity and permeability of are selected 12.2500 and 1.0 (silicon-Si) for high index layers and 1.8225 and 1.0 (cryolite-Na_3AlF_6) for low index layers [91]. Figure 5.8 presents the reflectance and transmittance for all dielectric layers as a function of the frequency for the incidence angles of 0°, 20°, and 40°. Solid lines correspond to 0°, dotted lines to 20°, and dashed lines to 40°. As it is seen from the figure, the reflectance becomes unity and the transmittance becomes zero at and around the central frequency. The symmetry shifts in frequency to the right side when the incident angle increased. The reflectance region is wider than the coating investigated in [90]. In addition, there are more ripples in the frequency behavior of the reflectance and transmittance.
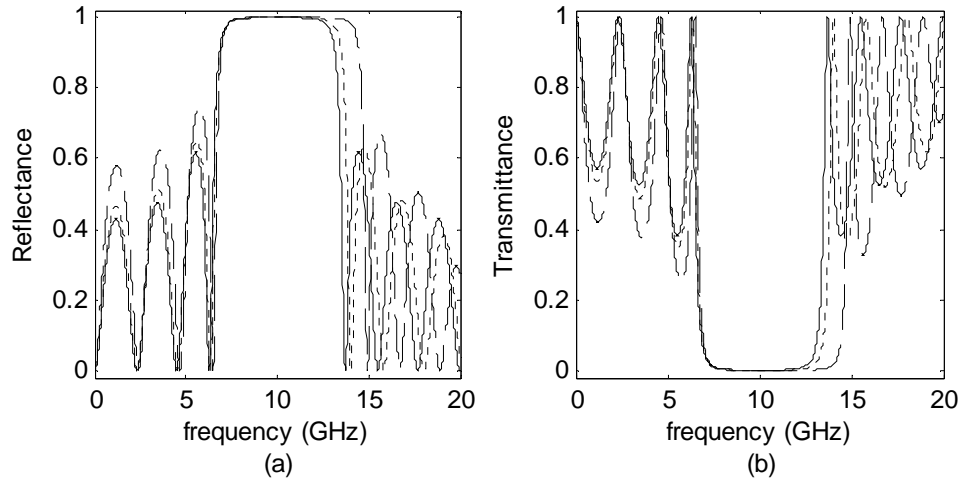
Figure 5.8: Reflectance and transmittance for all dielectric layers as a function of the frequency for the incidence angles of 0°, 20°, and 40°. Solid lines correspond to 0°, dotted lines to 20°, and dashed lines to 40°.

Secondly, the frequency response of seven DNG and DPS layers is presented. The permittivity and permeability are -12.2500 and -1.0 for DNG layers and 1.8225 and 1.0 for DPS layers, respectively. Figure 5.9 shows the reflectance and transmittance for the combination of DNG and DPS layers versus frequency for the incidence angles of 0°, 20°, and 40°. Solid lines correspond to 0°, dotted lines to 20°, and dashed lines to 40°. It is found that, for these DNG-DPS high reflection structures the pass band is larger and the effect of the incident angle is less dominant as compared to the all dielectric structures. In addition, these structures have no ripples and no sharp shifts and therefore they can be used as high reflection coatings. Furthermore, the reflectance band achieved here is wider than the region obtained for the coating investigated in [90].
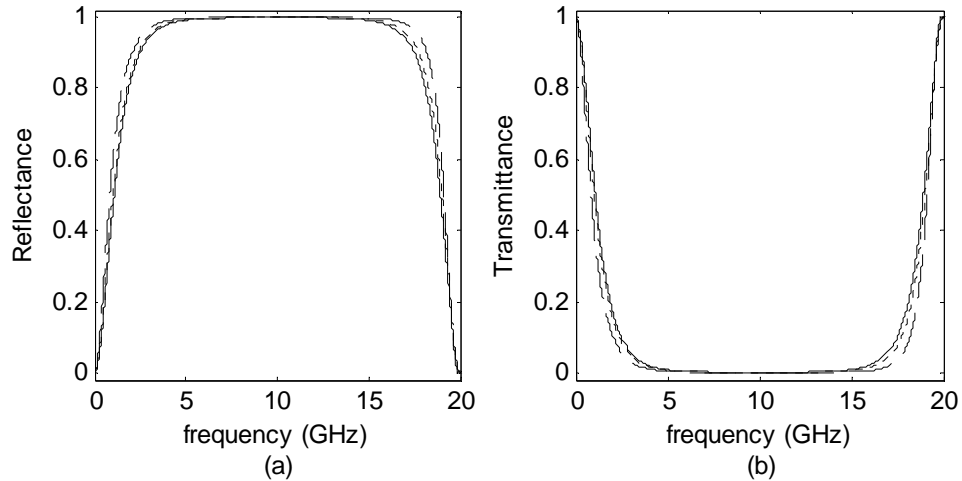
Figure 5.9: Reflectance and transmittance for DNG and DPS layers versus frequency for the incidence angles of 0°, 20°, and 40°. Solid lines correspond to 0°, dotted lines to 20°, and dashed lines to 40°.

The reflectance and transmittance for stratified structures consisting of half wavelength long DNG and DPS layers are also computed to show the effect of the layer thickness. The same parameters are used as in the previous example except the thicknesses. The computed results are presented in Figure 5.10. From the figure, the frequency band for high reflectance is narrow and split into two parts in this example. Also, there is high transmission at the operation frequency. Figure 5.10 recommends creating high transmission coatings using DNG and DPS layers.

Using the results of the previous example, we tried to create high transmission coatings using DNG and DPS layers. After proper combination of seven DNG and DPS layers, a high transmission coating created. To do this, DNG layers is selected to be a quarter wavelengths long while DPS layers are a half wavelengths long. The permittivity and permeability of are selected -5.0625 and -1.0 for high index layers and 2.1025 and 1.0 for low index layers. The results are shown in Figure 5.11. According to the figure, high transmission occurs in many frequency bands. At this band, transmittance sometimes becomes unity while the reflectance vanishes. At some bands shown in the figure, the reflectance becomes greater than the

transmittance. Thus, the structure can be utilized as high and partially transmission coatings. Note that, the numerical computations obtained here can easily be extended for the incident wave with the parallel polarization.
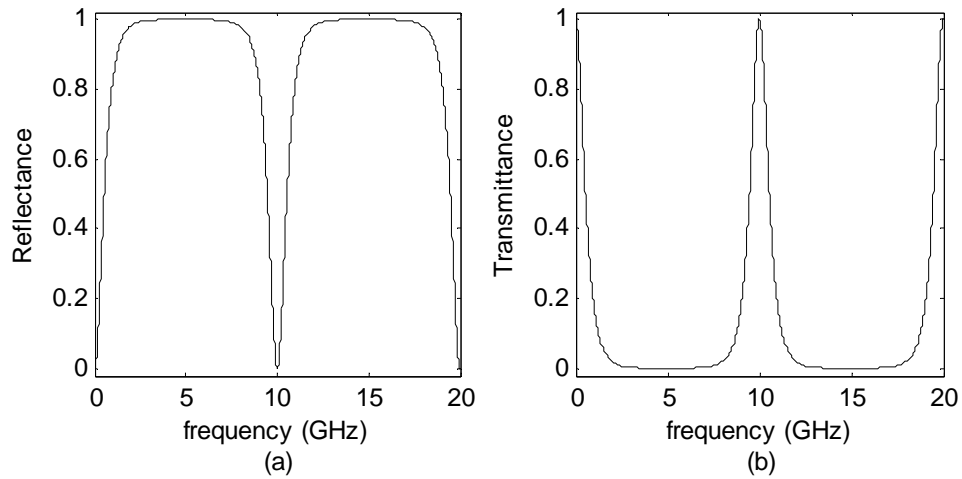
Figure 5.10: Reflectance and transmittance for half wavelength long seven DNG and DPS layers against the frequency.
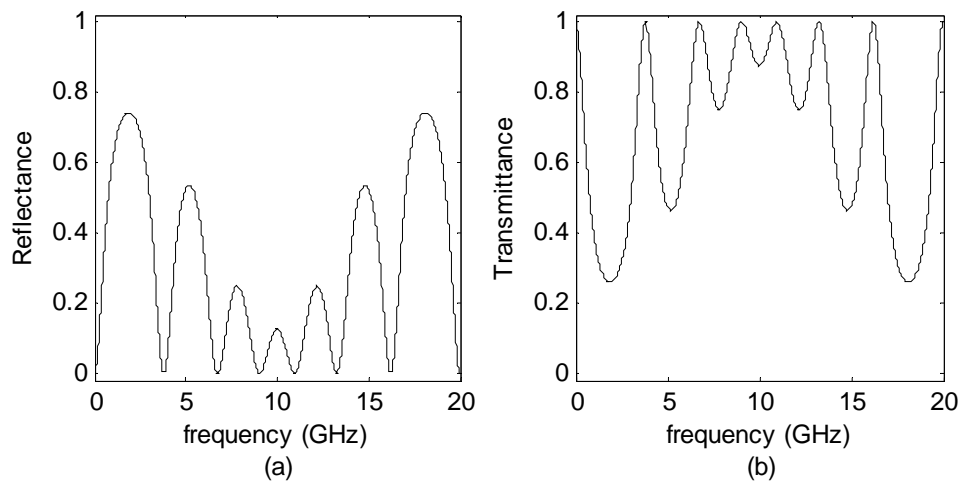
Figure 5.11: Reflectance and transmittance for half wavelength long DNG and quarter wavelength long DPS layers versus the frequency.

5.5 Distributed Bragg Reflectors

A stratified Distributed Bragg reflector (DBR) is a slab of layers of two alternating materials with different permittivities and permeabilities exhibiting very high reflectance in the Bragg regime. In a plot of reflectance versus wavelength of the normally incident plane wave on the DBR, the Bragg regime can be clearly observed due to the rectangular feature with an almost flat top and two vertical sides. The Bragg regime gets shifted when conventional materials in a DBR are replaced by DNG metamaterial. This property of DNG metamaterials can be used for their characterization [92]. The geometry of the stratified DBR consisting of DNG and DPS layers is the same with the geometry given in Figure 5.2. For the analysis, normally incident plane wave with the operation frequency of 10 GHz on a stratified DBR with 16 DNG and DPS layers is considered. We used 16 layers (instead of 20 layers as in [92]) for the purpose of the size reduction in the number of layers. The total thickness of two adjacent DNG and DPS layers is denoted by P. The thickness of DNG layer is equal to qP. The loss tangent of DNG layer is $\tan\delta = 0.001$ and then the permittivity and permeability of it is selected to become $4(-1+j0.001)$ and $1.02(-1+j0.001)$, respectively [92]. DPS layers are selected to be air. Plots of reflectance versus wavelength for three values of q are shown in Figure 5.12. The left side of the figure shows the reflectance when DNG layers is DPS layers with the permittivity and permeability of $4(1+j0.001)$ and $1.02(1+j0.001)$ for the comparison purpose. It can be seen that the width of Bragg regime is nearly same for each values of q for DBR with all DPS layers. Also, in this type of DBR, Bragg regime shifts to the longer wavelength. On the other hand, DBR with the combination of DNG and DPS layers has wider regime when q = 0.6 and q = 0.7. In this type, Bragg regime becomes wider when q increases. In addition, this regime gets shifted to the longer wavelength when q increases as in the previous one. But this shift is large enough when the conventional DPS layers are replaced by DNG metamaterial. Thus it can be said that the results obtained here can be utilized to construct high efficient reflectors.
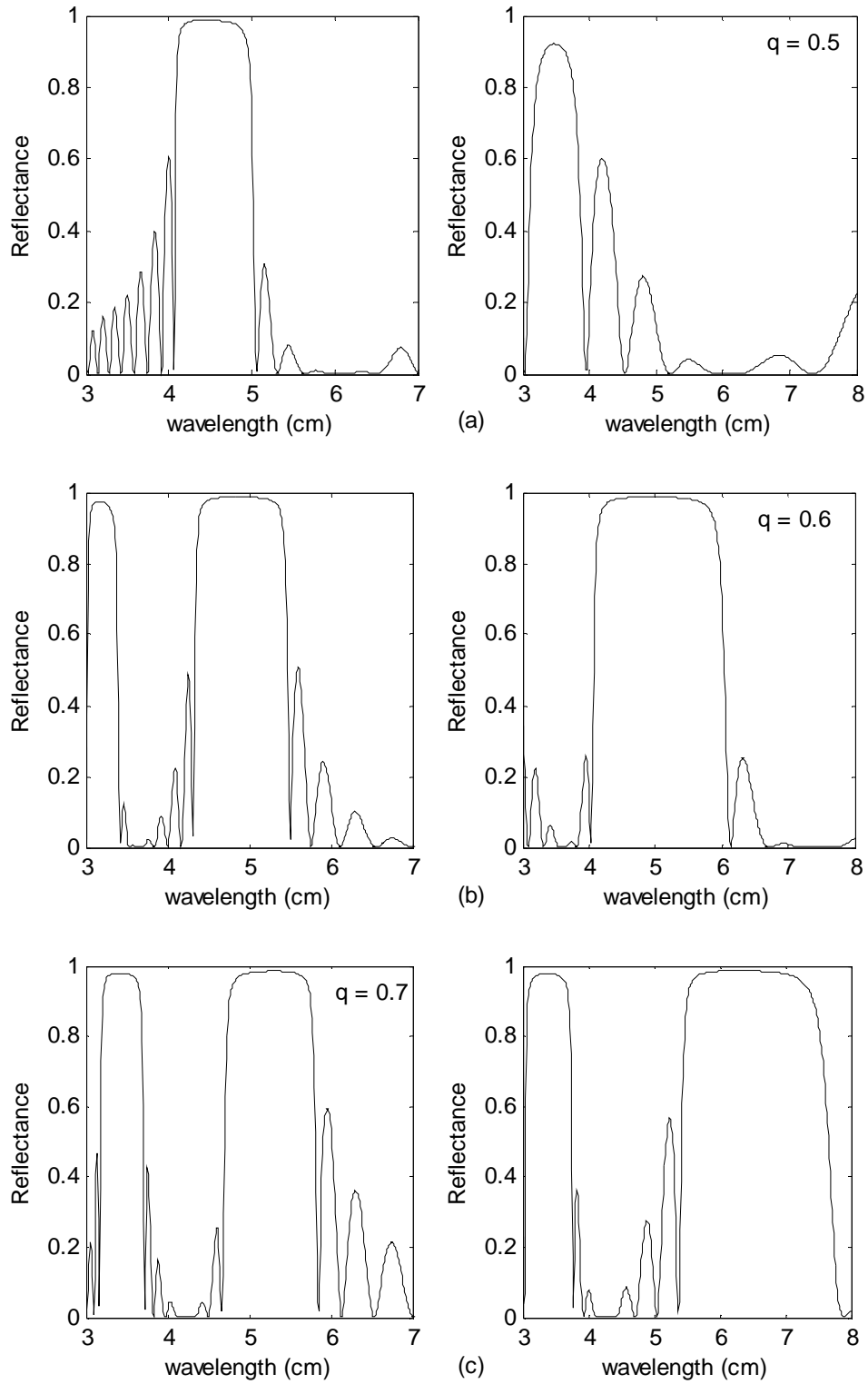
Figure 5.12: Reflectance versus wavelength for stratified DBR. The right side of the figure corresponds to all DPS layers and the left side to combination of DNG and DPS layers.

5.6 Stratified Double Negative Stacks of Cold Plasma Medium

The stratified DNG stacks considered in this section is composed of N frequency dispersive cold plasma layers with different material properties and thicknesses as shown in Figure 5.1. We have carried out the computations for the powers to observe the characteristics of them using the theoretical formulations obtained in Section 5.2, when the incident power is normalized to unity. The computations are verified using the transmission line equivalent method as explained in Appendix.

Example I: Here, we intend to find the characteristic of the non-dispersive DNG stacks. It is also worth mentioning that although the cold plasma medium has the frequency dependent parameters given in Equation (3.5) and Equation (3.6), both parameters are assumed to be constant over a frequency band in this example. To do this, f_{mp} and f_{ep} must be expressed as a function of the frequency f like $f_{mp} = c_1 f$ and $f_{ep} = c_2 f$. Note that, c_1 and c_2 must be real constant and greater than one to get negative permittivity and permeability for the DNG stacks. This is the hypothetical approximation which allows making a comment on the effect of the frequency for the non-dispersive DNG stacks characteristic. Note that, the non-dispersive and negative permittivity and permeability were used in many studies as in [42–45], [49], [53], [57], [62], [65], [88], [90], and [92].

The reflected (P_r) and transmitted (P_t) powers for the seven non-dispersive DNG stacks are calculated as a function of the frequency and the incidence angle when the incident electric field is a plane electromagnetic wave with the perpendicular polarization ($E_{//} = 0$). The incident and the transmitted media are assumed to become free-space and Germanium with $\mu_i = \mu_t = \mu_o$, $\varepsilon_i = \varepsilon_o$ and $\varepsilon_t = 16\,\varepsilon_o$. The operation frequency is selected to be $f_o = 1.0$ GHz. The seven non-dispersive DNG stacks are composed of two media H and L as (HL)^{3}H where $\mu_H = \mu_L = -\mu_o$, $\varepsilon_H = -9\varepsilon_o$ and $\varepsilon_L = -\varepsilon_o$ in which $f_{mp} = \sqrt{2}f$ and $f_{ep} = \sqrt{10}f$ for the H medium, and $f_{mp} = f_{ep} = \sqrt{2}f$ for the L medium. The thicknesses d_H and d_L are arranged from $|n_H d_H| = |n_L d_L| = \lambda_o/2$

where n_H and n_L are the refractive indices, and λ_o is the wavelength in free-space at the operation frequency.

Figure 5.13 points out the reflected and transmitted powers as a function of the frequency at normal incidence. P_r shows a band-pass filter characteristic between the frequency regions 0.28–0.72 GHz and 1.28–1.72 GHz. On the other hand, P_t reaches to unity between the ranges of 0–0.28 GHz, 0.72–1.28 GHz, and 1.72–2 GHz and shows a saw-comb filter characteristic. It is said that, the frequency response of the non-dispersive DNG stacks acts as the band-pass and anti-reflection filters at some frequency regions for the given configuration.

Figure 5.14 displays the reflected and transmitted powers versus the incidence angle at the operation frequency. The reflected power is nearly constant between 0° and 30°, and then it increases up to unity. The transmitted power is dominant between 0° and 50°, after that it decreases and becomes nearly zero after 70°. We can say that, after 70° there is no transmission, there is only reflection for the given example.

Figure 5.13: Reflected and transmitted powers for the seven non-dispersive DNG stacks as a function of the frequency at normal incidence.

Figure 5.14: Reflected and transmitted powers for the seven non-dispersive DNG stacks versus the incidence angle at the operation frequency.

Example II: In this example, we desire to find out the characteristics of the frequency dispersive double-negative stacks. The seven frequency dispersive DNG stacks are again considered as in the previous example to compute the reflected and transmitted powers as a function of the frequency and the incidence angle for the perpendicular polarization. The structure parameters for the incident, the DNG stacks, and the transmitted media are the same with the former one except for the permeability and permittivity of the DNG stacks. Here, they are calculated using Equation (3.5) and Equation (3.6) with the appropriate plasma frequencies. In addition, the effect of the plasma frequencies is emphasized in this computation. In our calculation, there are four plasma frequencies, two for the H medium and other two for the L medium. For emphasizing the effect of the plasma frequencies, three frequencies are fixed and the fourth one is varied.

Figure 5.15 corresponds to P_r and P_t against the frequency at normal incidence with f_{epH}=5 GHz, f_{epL}=4 GHz, and f_{mpH}=f_{mpL}=3 GHz. It is seen that from this figure, P_r and P_t show an oscillatory behavior at some frequency band. Furthermore, the given structure transmits the most of the incident wave, because P_t is greater than P_r in a wide range of the frequency.

Figure 5.16 depicts the reflected and transmitted powers against the frequency at normal incidence with f_{epH}=10 GHz, f_{epL}=4 GHz, and f_{mpH}=f_{mpL}=3 GHz. Here, f_{epH} is increased from 5 GHz to 10 GHz, to observe the effect of the plasma frequency. As it is observed from Figure 5.16, the frequency response of P_r and P_t is similar with Figure 5.13. P_r acts as a band-pass filter between the frequency bands 0.3–0.7 GHz and 1.3–1.7 GHz. In turn, P_t closes to unity between the ranges of 0–0.3 GHz, 0.7–1.3 GHz, and 1.7–2 GHz and it acts as a saw-comb filter. Comparing Figure 5.13 and Figure 5.16, one can see that, there is a small difference between the frequency bands and it can be neglected. Thus, the frequency dispersive DNG stacks have not fixed scattering characteristics due to the variable plasma frequencies. In addition, the same scattering characteristics as in the hypothetical non-dispersive DNG stacks can be obtained by arranging the plasma frequencies of the frequency dispersive DNG stacks.

Figure 5.15: Reflected and transmitted powers for the seven frequency dispersive DNG stacks against the frequency at normal incidence with f_{epH}=5GHz, f_{epL}=4 GHz, and f_{mpH}=f_{mpL}=3 GHz.

Figure 5.17 illustrates the reflected and transmitted powers versus the incidence angle at the operation frequency. The solid line refers to P_r and P_t with f_{epH}=10 GHz, f_{epL}=4 GHz, and f_{mpH}=f_{mpL}=3 GHz and the dotted line with $f_{epL} = f_{mpL} = f_{mpH} = \sqrt{2}$ GHz and $f_{epH} = \sqrt{10}$ GHz. As it is seen from solid lines, P_r

is monotonically increases and P_t is monotonically decreases with the angle of incidence. The transmitted power is dominant up to 45° and full reflection occurs at 90°. Note that, the same response as in Figure 5.14 is obtained when the plasma frequencies are arranged as $f_{epL} = f_{mpL} = f_{mpH} = \sqrt{2}$ GHz and $f_{epH} = \sqrt{10}$ GHz, as seen from the dotted lines.

(a)   (b)
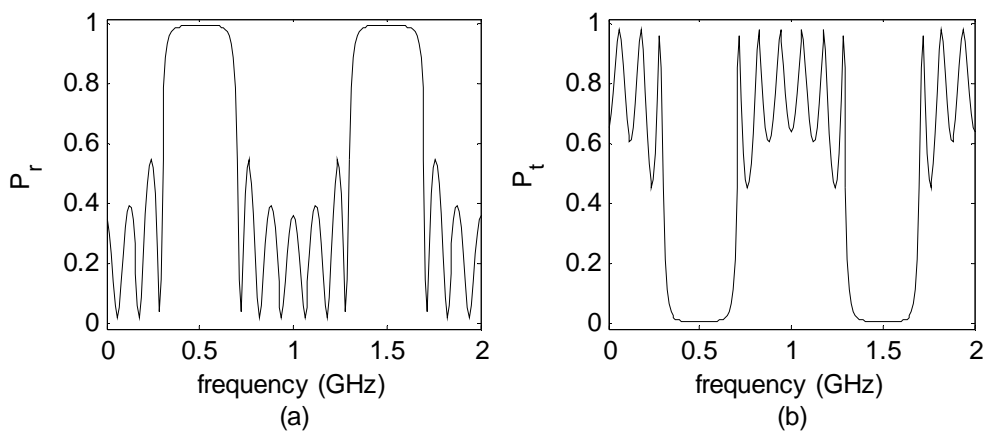
Figure 5.16: Reflected and transmitted powers for the seven frequency dispersive DNG stacks against the frequency at normal incidence with f_{epH}=10 GHz, f_{epL}=4 GHz, and f_{mpH}=f_{mpL}=3 GHz.

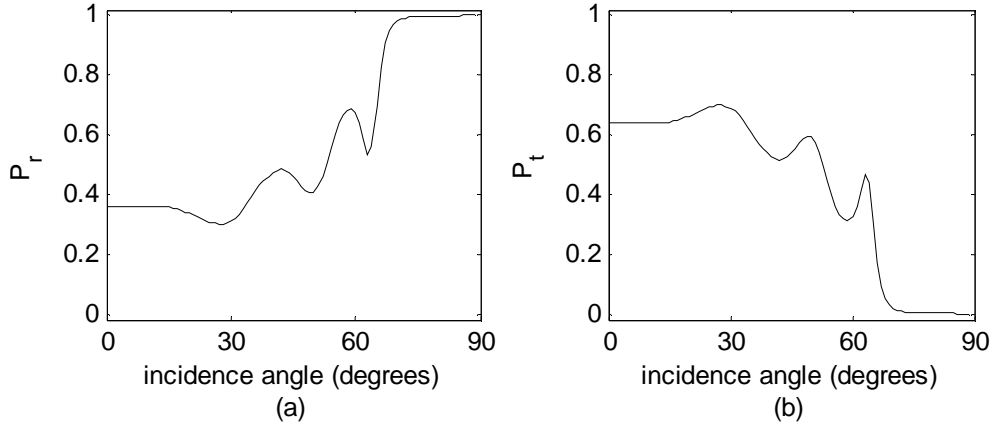(a)   (b)
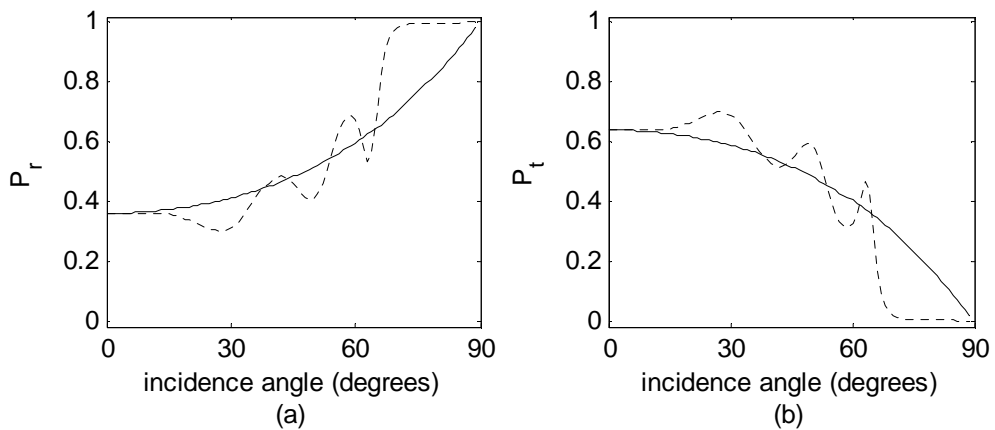
Figure 5.17: Reflected and transmitted powers for the seven frequency dispersive DNG stacks versus the incidence angle at the operation frequency.

Example III: In the last example, the effects of the plasma frequencies on the reflected and transmitted powers are presented. The seven DNG stacks are again considered with the same parameters as in the previous example except for the plasma frequencies. Here, the plasma frequencies are arranged as f_{epH}=19 GHz, f_{epL}=8 GHz, and f_{mpH}=f_{mpL}=7 GHz.

Figure 5.18 shows the reflected and transmitted powers as a function of the frequency at normal incidence with f_{epH}=19 GHz, f_{epL}=8 GHz, and f_{mpH}=f_{mpL}=7 GHz. There are multiple bandwidths in which the reflected power acts as a band-pass filter. There are also multiple frequency bands for the transmitted power which shows a saw-comb filter characteristic. It can be said that, the structure can be utilized as a multi band-pass and multi saw-comb filters. Furthermore, stop band regions in Figure 5.13(b) can be narrowed by arranging the structure parameters and plasma frequencies. Thus, the structure can be used as a multi notch filter.
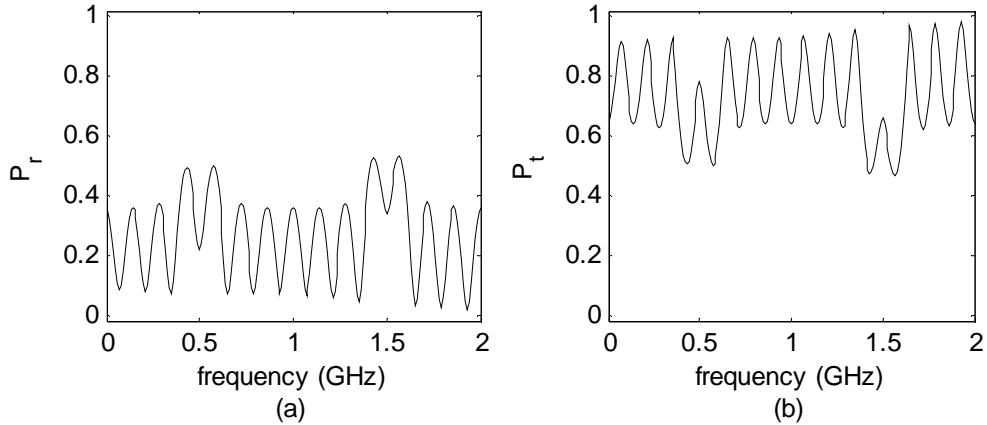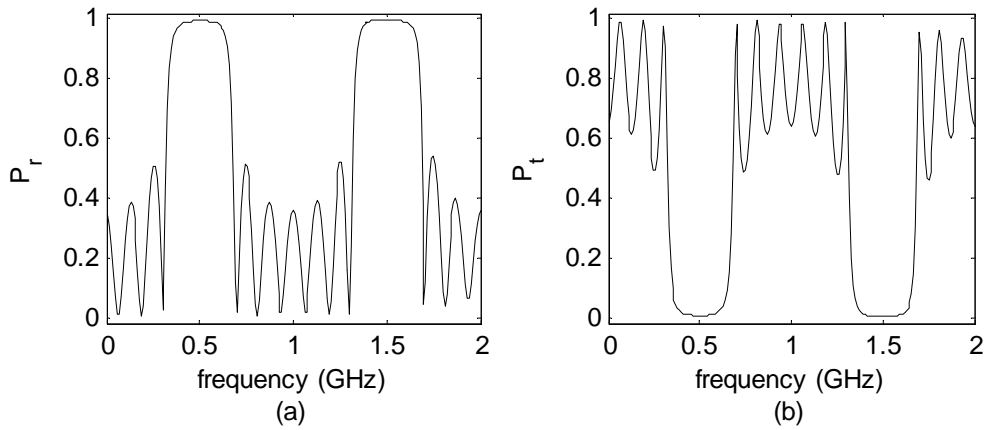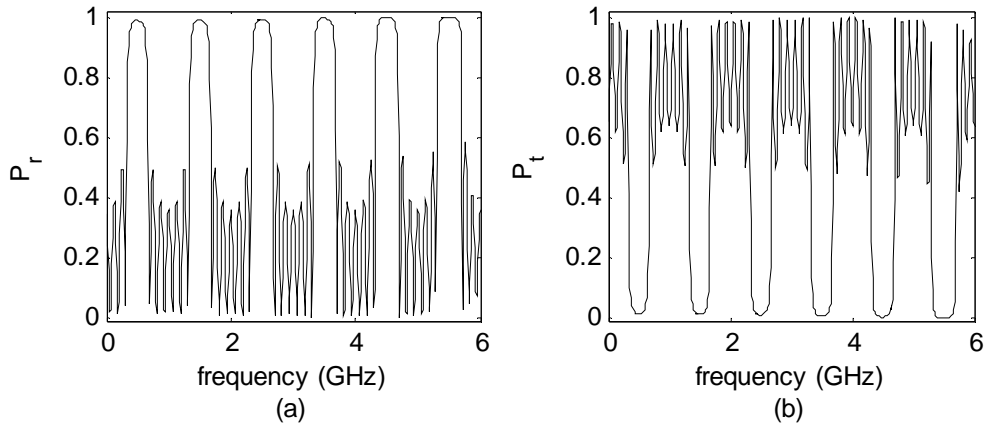

Figure 5.18: Reflected and transmitted powers for the seven frequency dispersive DNG stacks against the frequency at normal incidence with f_{epH}=19 GHz, f_{epL}=8 GHz, and f_{mpH}=f_{mpL}=7 GHz.

It is confirmed that, similar numerical results given in this study can easily be obtained for the incident wave with the parallel polarization. Also, as a conclusion,

electromagnetic filter applications of DNG materials using cold plasma medium are examined in this study. It can be said that from the numerical results, the hypothetical non-dispersive DNG stacks acts as the band-pass and saw-comb filters at some frequency regions for the given example. In turn, the frequency dispersive DNG stacks have not stable scattering characteristics due to the variable plasma frequencies and frequency dependent parameters. But, the same scattering characteristics as in the hypothetical non-dispersive DNG stacks can be provided by re-arranging the plasma frequencies. Furthermore, the frequency dispersive DNG stacks can be arranged to show the multi band-pass, multi saw-comb, and multi notch filters characteristics. Thus, the structure can be used as electromagnetic filters at some frequency bands. Design of these filters can be performed using the numerical results obtained here.

5.7 Multilayer Media Comprised of Double Negative Cold Plasma and Double Positive Slabs

In the previous section, scattering characteristics of the DNG stacks of cold plasma medium is studied. Here, the combination of DNG cold plasma and conventional DPS layers are analyzed in base of the geometry given in Figure 5.2. The magnitude of the reflectance ($|R|$) and transmittance ($|T|$) for the nine slabs are calculated as a function of the frequency. The first and the last DPS media are assumed to become free space and glass. The DPS slabs are selected to be mica. The operation frequency is f_o=1.0 GHz. The thicknesses for DNG slabs are arranged from $|nd|=\lambda_o/2$ and for DPS slabs from $|nd|=\lambda_o/4$ where n is the refractive index of the related medium, and λ_o is the wavelength in free-space at the operation frequency. The permittivity and permeability of the DNG slabs are calculated using Equation (3.5) and Equation (3.6).

Figure 5.19 points out the magnitude of reflectance and transmittance against the frequency at normal incidence with f_{ep}=10 GHz and f_{mp}=4 GHz. It is seen that from

this figure, |R| and |T| show an oscillatory behavior with the frequency. Furthermore, the given structure transmits the most of the incident wave, because |T| is greater than |R| in a wide range of the frequency.

Figure 5.20 depicts |R| and |T| versus the frequency at normal incidence with f_{ep}=22 GHz and f_{mp}=4 GHz. Here, f_{ep} is increased from 10 GHz to 22 GHz, to see the effect of the plasma frequency. Note that, when the plasma frequencies increase or decrease, the refractive index n changes. In turn, to keep $|nd|=\lambda_o/2$, the thickness d must be also changed. As it is observed from Figure 3, the frequency response of |R| acts as a band-pass filter between the frequency bands 0.25−0.7 GHz and 1.25−1.7 GHz. In turn, |T| closes to unity and acts as an anti-reflection filter between 0.7−1.25 GHz. At this point, it is said that, the given structure have not fixed frequency response due to the variable plasma frequencies and frequency dependent parameters. In addition, this structure can be used as band-pass filter and an anti-reflection filter in some frequency band by arranging the plasma frequencies.
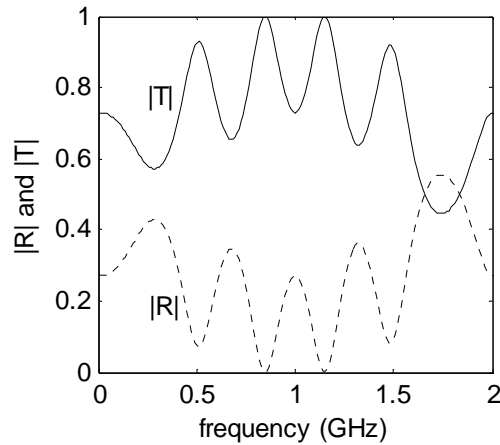
Figure 5.19: Reflectance and transmittance against the frequency with f_{ep}=10 GHz and f_{mp}=4 GHz.
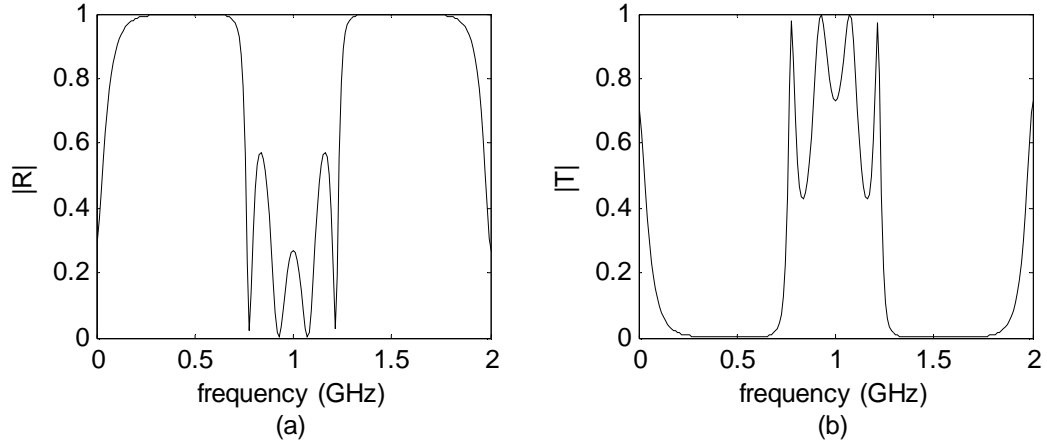
Figure 5.20: Reflectance and transmittance versus the frequency with f_{ep}=22 GHz and f_{mp}=4 GHz.

In conclusion, frequency response of the multilayer media comprised of DNG and DPS slabs are investigated with the emphasis on the plasma frequencies. It can be said that from the numerical results, the given structure have not stable frequency response due to the variable plasma frequencies and it acts as the band-pass and anti-reflection filters at some frequency bands. The results can be applied to design of the both filters at the optical, millimeter-wave, and microwave regimes.

5.8 Multilayer Structure of Lorentz type Double Negative Metamaterial with Double Positive Slabs

Numerical analysis of paired DNG-DPS layers as a multilayer structure embedded between two dielectric media is presented with the use of the transfer matrix method given in Section 5.2. The multilayer structure considered in this analysis is composed of N pieces DNG and DPS slabs with different material properties and thicknesses as shown in Figure 5.2. Once again, to verify the computations, firstly the conservation of power given in (5.13) is satisfied for all examples. Secondly, a transmission line equivalent is obtained for the structure as explained in Appendix. Both approaches give the same numerical values for all computations.

Two structures are considered in numerical results, Structure I (with three layers, N=3) and Structure II (with fifteen layers, N=15). Structure I is in the form of DNG-DPS-DNG and Structure II is (DNG-DPS)[7]DNG. Furthermore, the incident electric field is assumed a monochromatic plane wave with the perpendicular polarization ($E_{//} = 0$) when the incident angle is zero in all examples.

Example I: The reflected (P_r), and transmitted (P_t) powers are calculated as a function of the frequency. The incident and transmitted media are assumed to be free space and glass respectively with $\mu_i = \mu_t = \mu_o$, $\varepsilon_i = \varepsilon_o$, and $\varepsilon_t = 6\varepsilon_o$. The DPS layers are selected to become silicon dioxide (SiO$_2$) with $\mu_{DPS} = \mu_o$ and $\varepsilon_i = 2.1316\varepsilon_o$. The DNG layers are realized using Lorentz medium parameters given in (3.1) and (3.2). In the calculations, the following parameters are used as in [36] and [38]: $f_{mp}= 8.50$ GHz, $f_{mo}= 12.05$ GHz, $f_{ep}= 12.80$ GHz, and $f_{eo}= 10.30$ GHz. The electronic and magnetic damping frequencies are selected to be equal each other and zero ($\delta_e= \delta_m= \Gamma= 0$) as in [93]. This means that the structure is lossless. Note that, lossy and lossless Lorentz types of DNG metamaterials are characterized theoretically, used in several experiments, and fabricated for new devices in these studies. For example, wave propagation through the double negative Lorentz slab embedded between two different dielectric media is studied in [41], [49], [63], and [93−96]. Lorentz types of DNG metamaterials have frequency dispersive parameters and they can be fabricated using a mixture of conductive spirals or omega particles on a printed circuit boards. In addition, they can be manufactured using split ring resonators and wire strips on a circuit board materials. Numerous forms of DNG Lorentz metamaterials can also be found in the literature. The operation frequency is selected to be f_o=11 GHz within the frequency band (10.31−12.04 GHz) whereas the permittivity and permeability of DNG medium are simultaneously negative. The thicknesses are arranged from |n_{DNG} d_{DNG}|=c$_1\lambda_o$ and |n_{DPS} d_{DPS}|=c$_2\lambda_o$ where n_{DNG} and n_{DPS} are the refractive indices of the related medium, c$_1$ and c$_2$ are positive real constant, and λ_o is the wavelength in free-space at the operation frequency.

Figure 5.21 points out the reflected and transmitted powers as a function of the frequency for Structure I. From this plot, when $c_1=c_2=1/4$, the bandwidth extends from 10.31 to 11.5 GHz and the transmitted power has a sharp peak at 10.86 GHz. At this specific frequency, the structure can be utilized as a transmission (anti-reflection) filter in which the transmitted power becomes unity and the reflected power becomes zero. Also, from 11.5 to 12.04 GHz, it can be used as a reflection (anti-transmission) filter in which the reflected power becomes unity and the transmitted power becomes zero. When $c_1=1/2$ and $c_2=1/4$, it is seen from the dashed lines, the structure behaves like an all pass filter in a wide range of frequency since the transmitted power is almost constant around one and the reflected power is zero. When $c_1=1/4$ and $c_2=1/2$, it appears that the reflected and transmitted powers show similar behavior as in dashed lines. But in this case, the frequency range is narrower than the previous one, and the transmitted power is around 0.8 and the reflected power is around 0.2 at that range.

Figure 5.21: Reflected and transmitted powers as a function of the frequency for Structure I. Solid lines stand for $c_1=c_2=1/4$, dashed lines for $c_1=1/2$ and $c_2=1/4$, and dotted lines for $c_1=1/4$ and $c_2=1/2$.

Figure 5.22 shows the reflected and transmitted powers as a function of the frequency for Structure II. From this figure, the structure can be used a reflection filter between 10.31–12.04 GHz except for the range 10.7–11.1 GHz when $c_1=c_2=1/4$. Comparing Figure 5.21 and Figure 5.22, one can see that the bandwidth where transmitted power has a sharp peak is narrower than as in the Structure I. The transmitted power is dominant over a wide range of frequency for $c_1=1/2$ and $c_2=1/4$. But it is only dominant between the 10.6–11.2 GHz for $c_1=1/4$ and $c_2=1/2$.

Figure 5.22: Reflected and transmitted powers as a function of the frequency for Structure II. Solid lines stand for $c_1=c_2=1/4$, dashed lines for $c_1=1/2$ and $c_2=1/4$, and dotted lines for $c_1=1/4$ and $c_2=1/2$.

Example II: In this example, we intend to investigate the effect of layer thicknesses on the characteristics of the reflected and transmitted powers. All parameters are the same with example I except for the thicknesses. Here, the thicknesses are $d_{\mathrm{DNG}}=c_3\lambda_o$ and $d_{\mathrm{DPS}}=c_4\lambda_o$ where c_3 and c_4 are positive real constant.

Figure 5.23 displays the frequency response of the reflected and transmitted powers for Structure I. From solid, dashed, and dotted lines, it is said that, the

characteristics of the powers are not smooth here. For all values of c_3 and c_4, the transmitted power has sharp peaks. Also, it closes to unity at 10.46 GHz when $c_3=1/4$ and $c_4=1/2$. On the other hand, the reflected power reaches to unity at many frequencies for all cases. In addition, the transmitted power has the wide pass band and narrow stop band regions throughout the frequency spectrum for all cases of c_3 and c_4. In contrast, the reflected power has the narrow pass band and wide stop band regions.

Figure 5.24 presents the reflected and transmitted powers versus the frequency for Structure II. As it is seen from this plot, the reflected and transmitted powers are again not smooth as in Figure 5.23. Pass band region for the transmitted power is not wide as in the previous figure for all cases of c_3 and c_4. Also, it has more stop band regions. In return, the reflected power has more pass band and stop band regions for all cases.

Figure 5.23: Reflected and transmitted powers versus the frequency for Structure I. Solid lines correspond to $c_3=c_4=1/4$, dashed lines to $c_3=1/2$ and $c_4=1/4$, and dotted lines to $c_3=1/4$ and $c_4=1/2$.
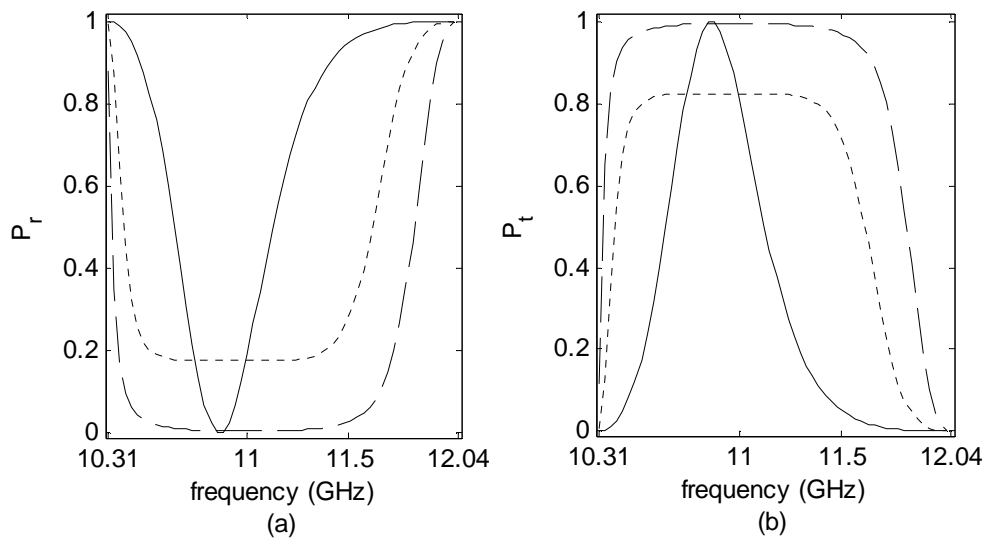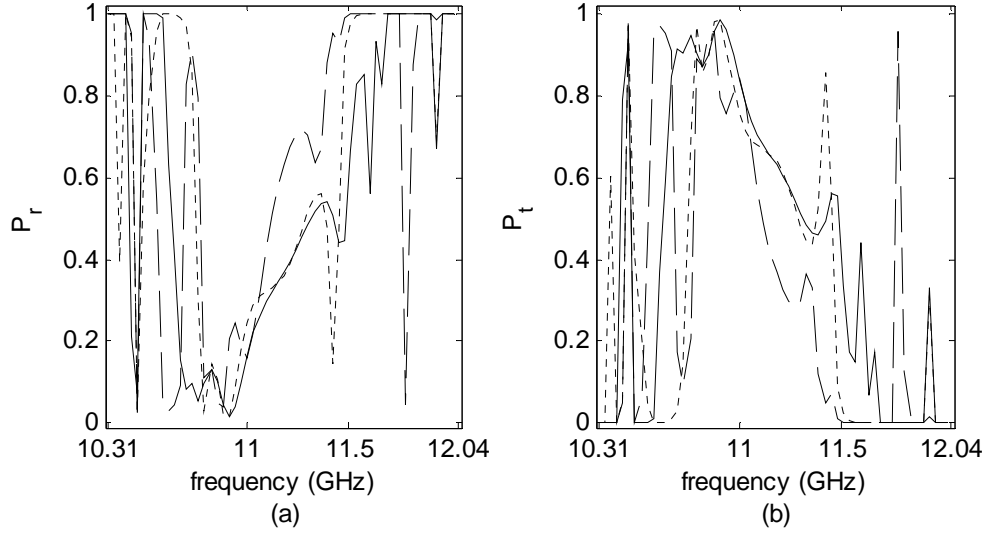
Figure 5.24: Reflected and transmitted powers versus the frequency for Structure II. Solid lines correspond to $c_3=c_4=1/4$, dashed lines to $c_3=1/2$ and $c_4=1/4$, and dotted lines to $c_3=1/4$ and $c_4=1/2$.

According to Figure 5.23 and Figure 5.24, two structures act as the band pass and stop band filters at some frequency regions. Design of efficient filters can be considered using numerical results obtained here by arranging the structure parameters, layer numbers and thicknesses.

5.9 Multilayer Structure of Double Negative Drude Medium with Double Positive Slabs

In this section, the same analysis is provided for the paired DNG-DPS layers. Here, the DNG layers are realized using the Drude medium parameters given in Equation (3.3) and Equation (3.4). In our calculations, the following parameters are used as in [36] and [38]: $f_{mp}=$ 10.95 GHz and $f_{ep}=$ 14.50 GHz. The electronic and magnetic damping frequencies are zero as in [93]. The operation frequency is $f_o=6$ GHz within the frequency band (2−10 GHz) where the permittivity and permeability of DNG medium are simultaneously negative. The frequency range is wider than the range of

the Lorentz medium. At this point, we can say that, the simultaneously negative permittivity and permeability can be realized in the wide frequency band for the Drude medium more easily than for the Lorentz medium. Once more, two structures are considered in numerical results as in the previous section with the thicknesses of $|n_{DNG}\, d_{DNG}|=c_1\lambda_o$ and $|n_{DPS}\, d_{DPS}|=c_2\lambda_o$. The other parameters are assumed to be same as in the previous section.

Figure 5.25 depicts P_r and P_t against the frequency for Structure I. As it is observed from this plot, P_r (P_t) power shows monotonically decreasing (increasing) up to 6.5 GHz and then it increases (decreases) with the frequency when $c_1=c_2=1/4$. Full transmission occurs around 6.5 GHz for this case. When $c_1=1/2$ and $c_2=1/4$, the powers behaves like an oscillatory function up to ~8 GHz. Also, they are constant up to this frequency when $c_1=1/4$ and $c_2=1/2$.
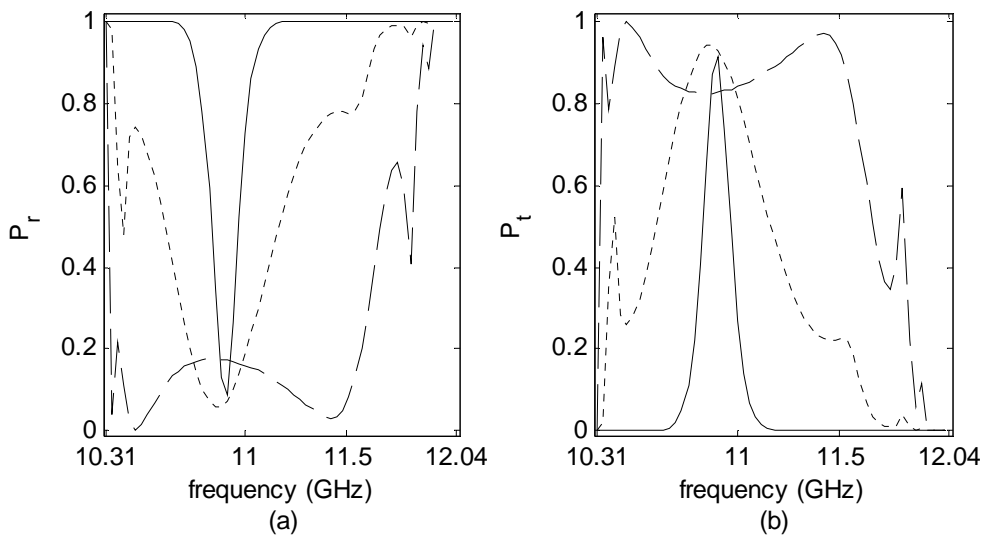

Figure 5.25: Reflected and transmitted powers against the frequency for Structure I. Solid lines represent $c_1=c_2=1/4$, dashed lines $c_1=1/2$ and $c_2=1/4$, and dotted lines $c_1=1/4$ and $c_2=1/2$.

Figure 5.26 demonstrates P_r and P_t against the frequency for Structure II. The powers do not show monotonically characteristics as in Figure 6 when $c_1=c_2=1/4$. P_t is dominant up to 8.5 GHz in this case. P_r and P_t changes periodically between 2–8 GHz when $c_1=1/2$ and $c_2=1/4$. The powers show slightly periodic behavior when $c_1=1/4$ and $c_2=1/2$. In the last two cases, P_t is dominant in all frequencies studied here.
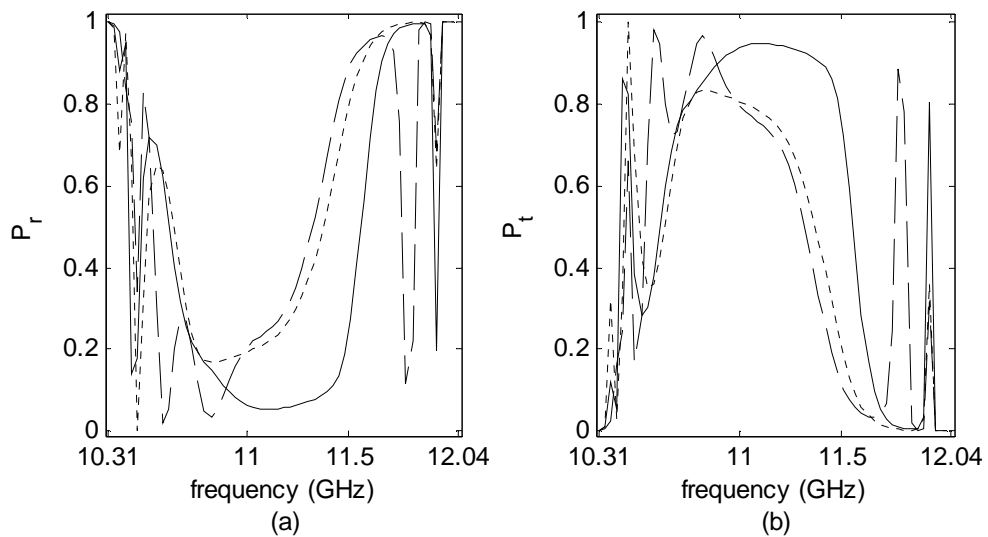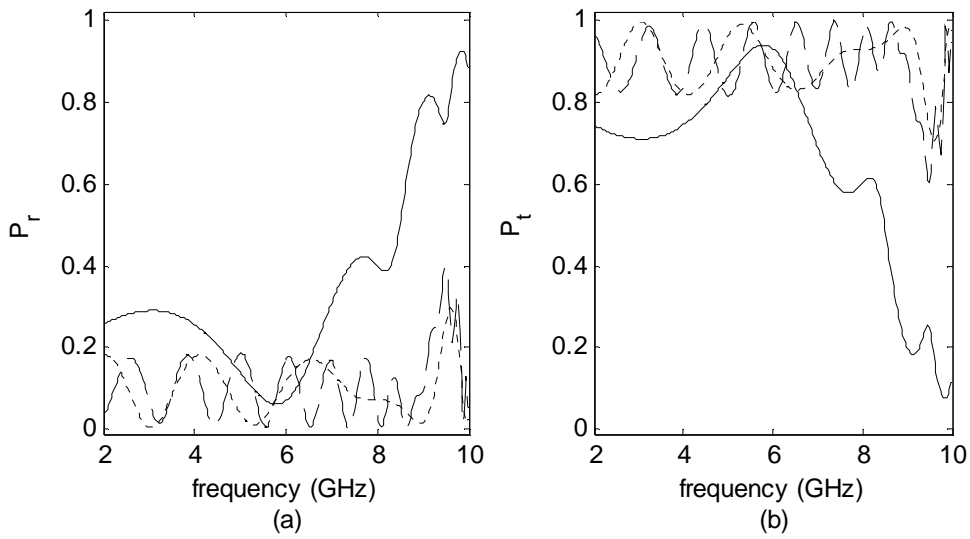

Figure 5.26: Reflected and transmitted powers against the frequency for Structure II. Solid lines represent $c_1=c_2=1/4$, dashed lines $c_1=1/2$ and $c_2=1/4$, and dotted lines $c_1=1/4$ and $c_2=1/2$.

From Figure 5.25 and Figure 5.26, it can be concluded that, the structure parameters, layer numbers and thicknesses can be arranged to design high efficiency transmission filter.

In the second example, we present the effect of layer thicknesses on the characteristics of P_r and P_t. All parameters are the same with example III except for the thicknesses. Here, the thicknesses are $d_{DNG}=c_3\lambda_o$ and $d_{DPS}=c_4\lambda_o$ where c_3 and c_4 are positive real constant.

Figure 5.27 corresponds to P_r and P_t against the frequency for Structure I. It is seen that, P_r oscillates between zero and 0.2 in all cases of c_3 and c_4. In turn, P_t oscillates between 0.8 and one. P_t is dominant over a wide frequency band in all cases of c_3 and c_4.

Figure 5.28 indicate P_r and P_t against the frequency for Structure II. Only $c_3=c_4=1/4$ case is illustrated in this figure. The other cases skipped here since P_r and P_t have high oscillating behavior. When $c_3=c_4=1/4$ P_r and P_t show frequent oscillating behavior up to 9.6 GHz. After this frequency P_r increases and it become unity at 10 GHz. On the other hand, P_t decreases and it become zero at 10 GHz.

From Figure 5.27 and Figure 5.28, it can be said that, high efficiency oscillating filters for the transmitted wave can be designed by arranging the structure parameters, layer numbers and thicknesses.
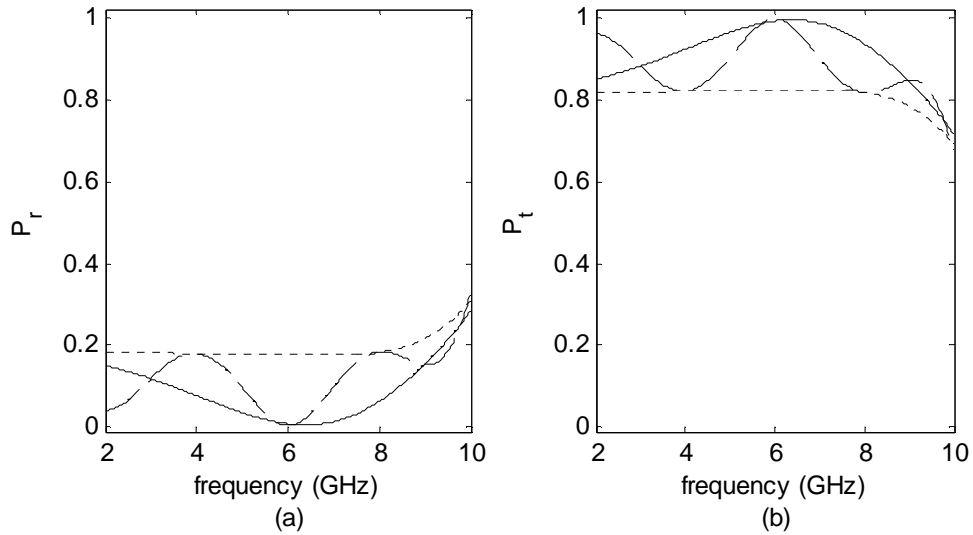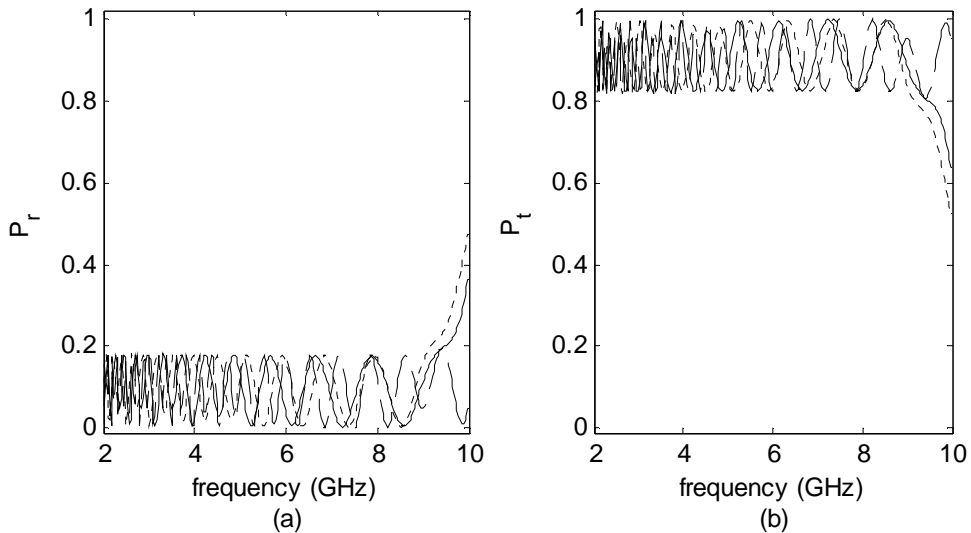

Figure 5.27: Reflected and transmitted powers against the frequency for Structure I. Solid lines represent $c_3=c_4=1/4$, dashed lines $c_3=1/2$ and $c_4=1/4$, and dotted lines $c_3=1/4$ and $c_4=1/2$.
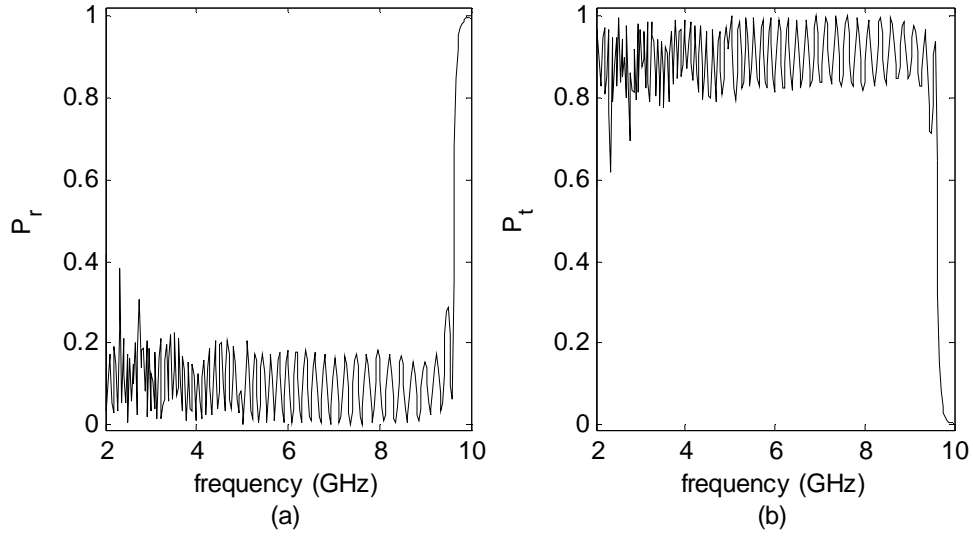
Figure 5.28: Reflected and transmitted powers against the frequency for Structure II when $c_3=c_4=1/4$.

In the last two sections, the DNG layers are realized using the Lorentz and Drude media parameters in which their properties are examined in Chapter 3. It can be said that from the numerical results, the structures given in this study can be utilized as reflection and transmission filters at some frequency band. Specifically, pass band, stop band, all pass and oscillating filters can be designed by arranging the structure parameters, layer numbers and thicknesses. Furthermore, the structure transmits the most of the incident wave because the transmitted power is dominant over a wide frequency range in some cases. Thus, the transmission filters with high efficiency can be designed in a wide range.

5.10 Summary and Discussion

In conclusion, we have successfully demonstrated the stratified structures comprised of pure DNG metamaterials and mixed DNG metamaterials and DPS layers. First, the stratified DNG stacks and the paired DNG-DPS layers are constructed and then they are analyzed theoretically. In the analysis, transfer matrix method is used. After that, several numerical examples and applications of DNG multilayer metamaterials are presented. Mirrors with DNG slabs, high reflection coatings consisted of DNG and DPS layers, distributed Bragg reflector (DBR) based on DNG and DPS slabs, stratified DNG stacks of cold plasma medium, multilayer media comprised of DNG stacks of cold plasma and conventional DPS layers, and multilayer structure of DNG Lorentz/Drude Medium with DPS slabs are studied and their scattering characteristics are shown in this chapter. According to the results obtained here, the studied stratified structures show distributed Bragg reflector behavior, high reflection and transmission coatings characteristics, band pass, stop band, anti-reflection, multi band-pass, multi saw-comb, oscillating, and multi notch filters characteristics at some frequency regions. High efficiency reflectors, coatings, and filters for electromagnetic wave with any polarization can be designed by arranging the structure parameters, layer numbers and thicknesses. This work will cover the absence in the literature and make a foundation for the future application of the DNG medium. Moreover, it will provide to realize and manufacture high efficiency reflectors, coatings, and filters at the millimeter wave, optical, and microwave regimes.

CHAPTER 6

NOVEL METAMATERIALS: TRIANGULAR SPLIT RING RESONATOR AND WIRE STRIP

6.1 Introduction

The purpose of this chapter is to realize novel metamaterials based on the shape and geometry. Several theoretical and experimental works have been studied by researchers to create new metamaterials [13], [35−76], [78−88], [90], [92−105]. The design of metamaterial based on shape and geometry is the most interesting work among the others [97−105]. Especially, the design of split rings which provide the negative permeability is very important to construct new types of metamaterials. Numerous types of different ring and ring-like structures such as circular, square, Ω-shaped, U-shaped, S-shaped and others are used to create new metamaterials (see [49] and [88] for a brief history). In the light of the known structures, we will construct new metamaterials using triangular shaped ring which has not been studied yet. Thus, we will build and analyze a new metamaterials that contains triangular split ring resonator (TSRR) and wire strip (WS). In the analysis, S parameters and retrieved effective material parameters (wave impedance, refractive index, permittivity, and permeability) will be computed and presented. We will also show that the novel metamaterials are well designed and they can be manufactured for several potential applications in the microwave, millimeter wave and optical frequency bands. Furthermore, novel metamaterial slabs will be manufactured to construct multilayer structures and to make some transmission experiments.

6.2 Analysis and Simulations

As it is well known, the combination of split ring resonator (SRR) and WS structures are commonly used to engineer artificial metamaterials showing unconventional properties not found in nature. In literature, several types of SRR are proposed for construction purposes. TSRR is one of them and firstly studied in this work. Figure 6.1 illustrates the geometry of the unit cells comprised of TSRR and WS for three different structures. In this figure, MTM represents the metamaterial.
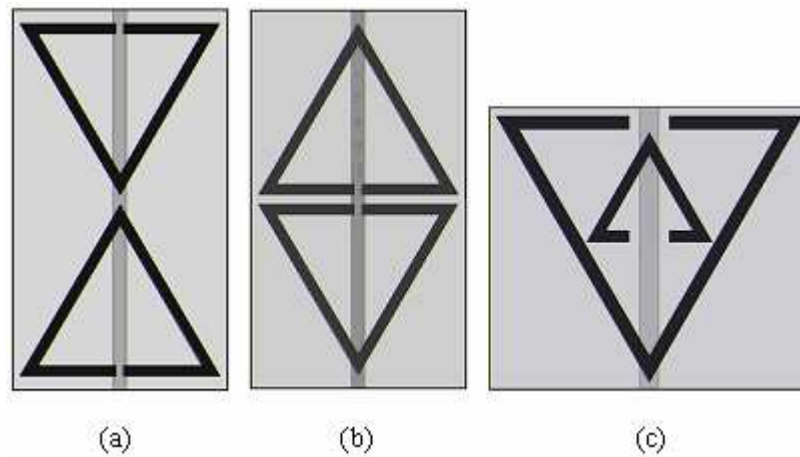
Figure 6.1: Three different types of metamaterial unit cells (a) MTM1 (b) MTM2 (c) MTM3.

An FR4 of 0.25 mm thickness (with relative permittivity $\varepsilon_r = 4.4$ and loss tangent $\delta = 0.02$) is used as a substrate for each configuration. TSRR and WS are made of copper with conductivity of 5.8×10^7 S/m and thickness of 0.017 mm. The width of all TSRR is 0.4 mm. TSRR is located on one face of FR4 and WS is etched on its opposite face. WS is continuous along the whole of FR4 substrate in all structures, as shown in Figure 6.1. Metamaterial unit cells are designed and simulated using the commercial software package, ANSOFT's High Frequency Structure Simulator (HFSS), based on finite-element method (FEM). Open, electric, magnetic and periodic boundary conditions are used in the simulation. Each configuration is placed

in a two-port waveguide formed by a pair of both perfect electric conductor (PEC) and perfect magnetic conductor (PMC) walls. All FR4 substrates with TSRR and WS are centered in the waveguide.

To show the physical properties of the designed structures, S parameters for a single unit cell is calculated with the mentioned boundaries along the wave propagation. Next, the effective material parameters can be extracted from the S parameters as [97], [98], [100]

$$z = \sqrt{\frac{(1+S_{11})^2 - S_{21}^2}{(1-S_{11})^2 - S_{21}^2}}$$

(6.1)

$$n = \frac{1}{kd} \cos^{-1}\left[\frac{1}{2S_{21}}(1 - S_{11}^2 + S_{21}^2)\right]$$

(6.2)

where z and n indicate the wave impedance and refractive index, respectively. Then, the electric permittivity and magnetic permeability can be computed from the equations of $\varepsilon = n/z$ and $\mu = nz$.

6.2.1. Simulation of MTM1

In the first simulation, we simulated the MTM1 which is shown in Figure 6.1(a). The simulated structure in a waveguide configuration with open (OB), electric (EB) and magnetic (MB) boundaries is presented in Figure 6.2. The width of WS is 0.5 mm. The base and the height of TSRR are 7.794 mm and 6.75 mm, respectively. The gap in each TSRR is 0.3 mm and the separation between TSRR is 0.4 mm.
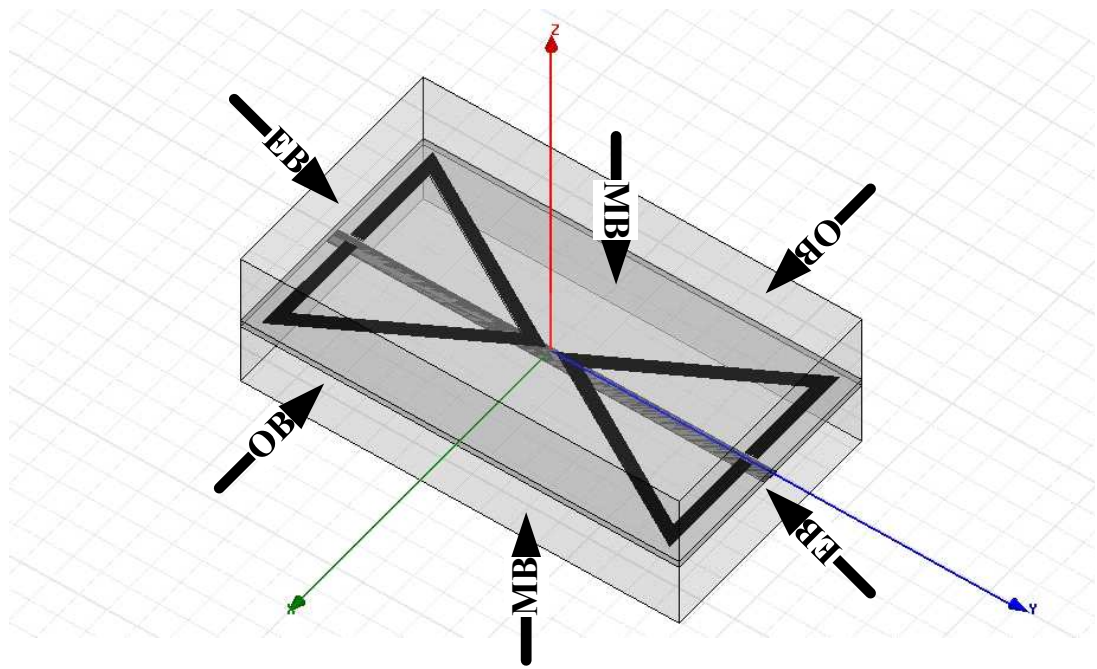
Figure 6.2: The simulated unit cell in a waveguide configuration with open (OB), electric (EB) and magnetic (MB) boundaries for MTM1.

The S parameters for the MTM1 are computed and the effective material parameters are extracted by means of S parameters using HFSS which are given in Figure 6.3. In this figure, the magnitude and the phase of S parameters, real and imaginary parts of wave impedance, refractive index, permittivity and permeability are illustrated. S parameters and wave impedance are plotted in the range of 0−8 GHz. But, the refractive index, permittivity and permeability are plotted between 2.5 GHz and 5.5 GHz to see the negative region easily (for the zooming purpose). As it is seen, all parameters are frequency dependent complex functions which satisfy certain requirements of causality. The dip in the phase of S_{21} indicates the presence of negative region which is observed at 4.33 GHz. For passive materials, real part of the wave impedance and imaginary part of the refractive index must be greater than zero. The wave impedance and refractive index satisfy this condition for our configuration. According to the refractive index, the negative band approximately lies between 3.5 GHz and 5 GHz. In the theory of metamaterials, the real parts of the permittivity and permeability must be negative. Negative real parts of the permittivity and permeability lies in the negative band (3.5−5 GHz). Also, the

permittivity and permeability show Drude and Lorentz response behavior in the studied frequency region, respectively. While negative permittivity occurs between the region of 2.5 GHz and 5.5 GHz, negative permeability occurs over the range of ~ 4.4 GHz to ~ 5 GHz. Thus, it can be said that negative permittivity has wider frequency band than the permeability.

Figure 6.3: Magnitude and phase of S parameters, real and imaginary parts of the wave impedance, refractive index, permittivity and permeability for MTM1.

In Figure 6.4, we present the electric field and surface current density for MTM1. The color map shows the electric field amplitude, and the arrows indicate the direction and size of the surface current density. The electric field is strong at the apex and at the gaps as it is desired. The induced surface current density is in the circular form and it is weak at the gaps. Thus, around the apex and the gaps of TSRR and around the center and ends of WS, the electric field is resonantly enhanced. In addition, the contribution of WS to the induced surface current density is very weak in this type of metamaterial.

Note that, some parts of this study are accepted for publication in the Proceedings of XXIX General Assembly of the International Union of Radio Science [106].
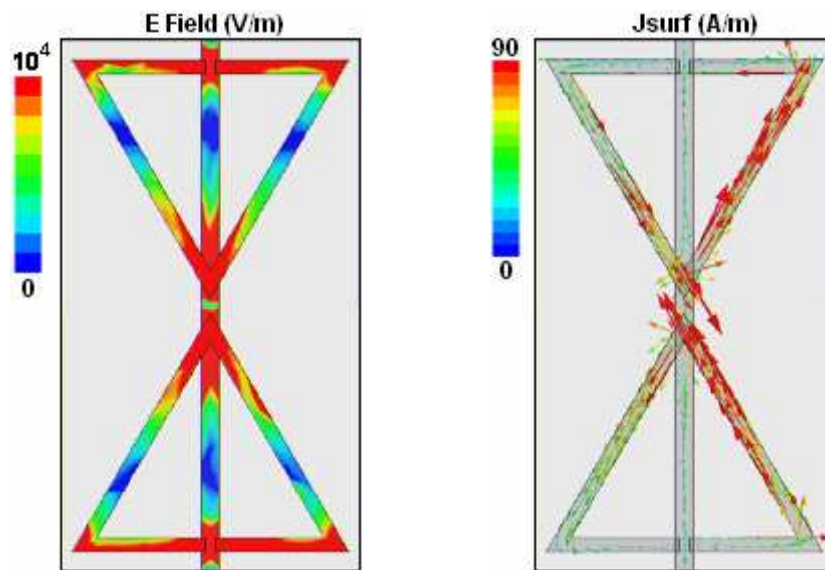
Figure 6.4: Electric field and surface current density for MTM1.

6.2.2. Simulation of MTM2

As the second simulation, MTM2, shown in Figure 6.1(b), is simulated. The width of WS, the base and the height of TSRR, the gap in each TSRR, and the separation between TSRR are the same with the previous example. The only difference between MTM1 and MTM2 is the position of TSRR. In the first one, TSRR is located apex to apex while in the second one base to base. S parameters and the effective material parameters (real and imaginary parts of wave impedance, refractive index, permittivity and permeability) for the MTM2 are presented in Figure 6.5. The same frequency range as in the first simulation is used. The dip which shows the negative region in the phase of S_{21} is at 3.63 GHz. The negative region approximately lies between 3 GHz and 4.5 GHz. Comparing Figure 6.5 and Figure 6.3, the data clearly shows that negative region shifts toward the left side of 4 GHz. Also, all computed parameters shift to the left side in this simulation. Here, the wave impedance changes from -2.75 to 2.75. But in the previous one, it changes from -2.5 to 2.5. Similar variations can be observed for the other computed parameters. As it is seen from the figures, negative permittivity occurs between 2.5 GHz and 5.5 GHz which is the same with MTM1. The only difference is magnitude. Negative permeability occurs over the range of ~ 3.75 GHz to ~ 4.25 GHz.

Figure 6.6 shows the electric field amplitude and surface current density for MTM2. The electric field for MTM2 is stronger than the electric field for MTM1. But, the surface current density is weaker here. Also, the electric field is strong at the apex, the base and the gaps. The surface current density is again in the circular form and it is weak according to the first structure. Thus, the electric field is generally around the apex, the base and the gaps of TSRR and around the center and ends of WS. Again, the contribution of WS to the induced surface current density is very weak.
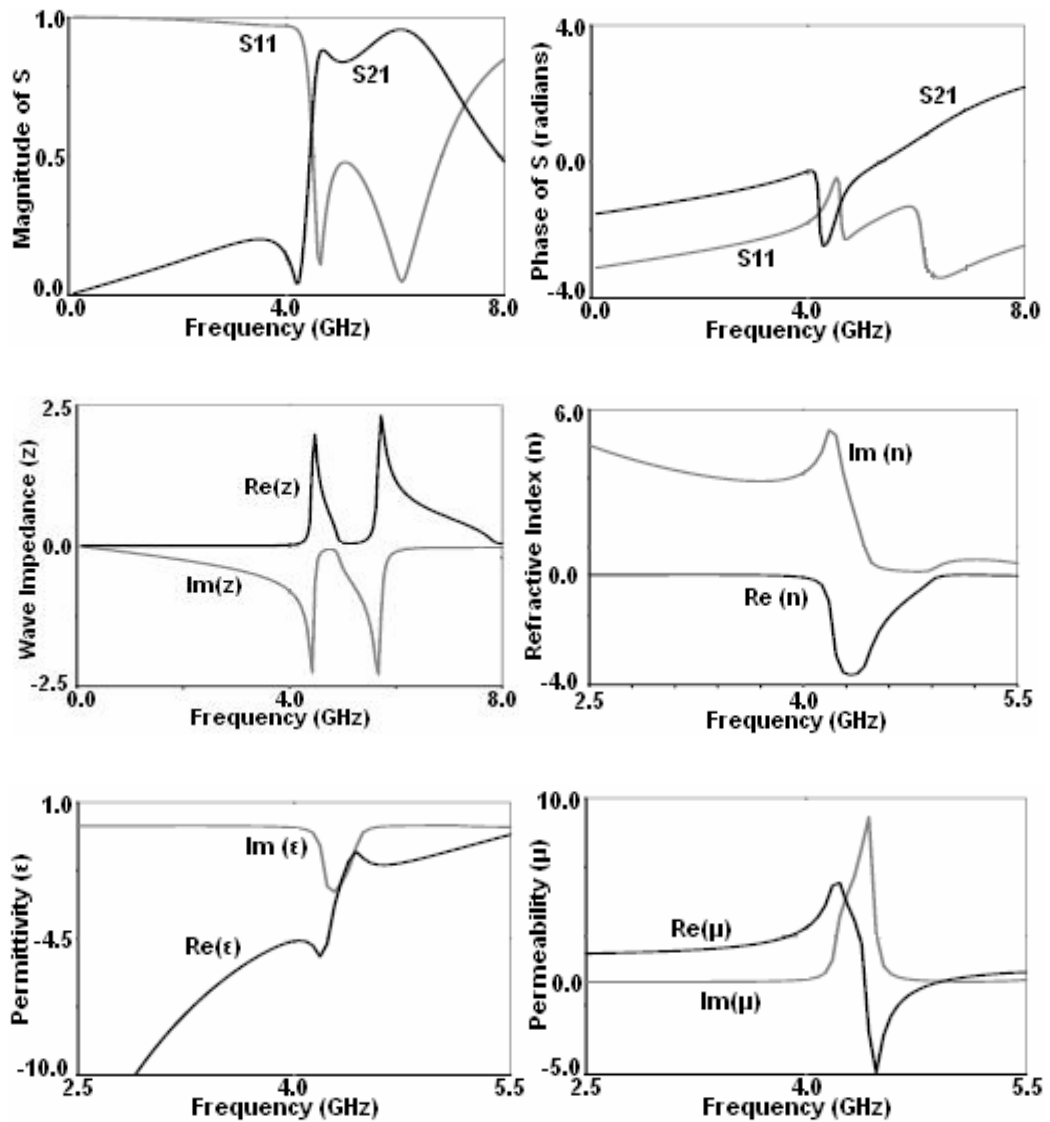
Figure 6.5: Magnitude and phase of S parameters, real and imaginary parts of the wave impedance, refractive index, permittivity and permeability for MTM2.

Figure 6.6: Electric field and surface current density for MTM2.

6.2.3. Simulation of MTM3

In the last simulation, we present the simulation of MTM3 which is shown in Figure 6.1(c). The dimensions of WS are 0.3 mm x 7.3 mm x 0.017 mm, respectively. The base and the height of TSRRs are given as: 7.98 mm and 6.91 mm for outer TSRR; 2.942 mm and 2.548 mm for inner TSRR. The gap in each TSRR is 0.5 mm and the separation between TSRR is 3.603 mm from the apex of outer TSRR to the base of inner TSRR. Figure 6.7 indicate the S parameters and the effective material parameters for the MTM3. Here, the dip in the phase of S_{21} is observed at 3.80 GHz. The negative band approximately lies between 3.2 GHz and 4.6 GHz. Negative real parts of the permittivity occurs in the region of 2.5–5.5 GHz, but negative real parts of the permeability lies between 3.85 GHz and 4.35 GHz.

For MTM3, the electric field and surface current density which are shown with the color map and the arrows are presented in Figure 6.8. In this configuration, the electric field is not strong at the apex and at the gaps as in the previous structures. Here, it is strong at the legs of TSRR and at the WS except the ends. The induced

surface current density is again in the circular form and it is too weak at the TSRRs on the contrary of the other two structures. In this geometry, the surface current density is very strong at WS especially across the apex of TSRRs. The electric field is again enhanced in almost all of WS and some parts of the legs of TSRR in this configuration. Here, the surface charge density is induced by the strong contribution of WS on the contrary of the previous structures.
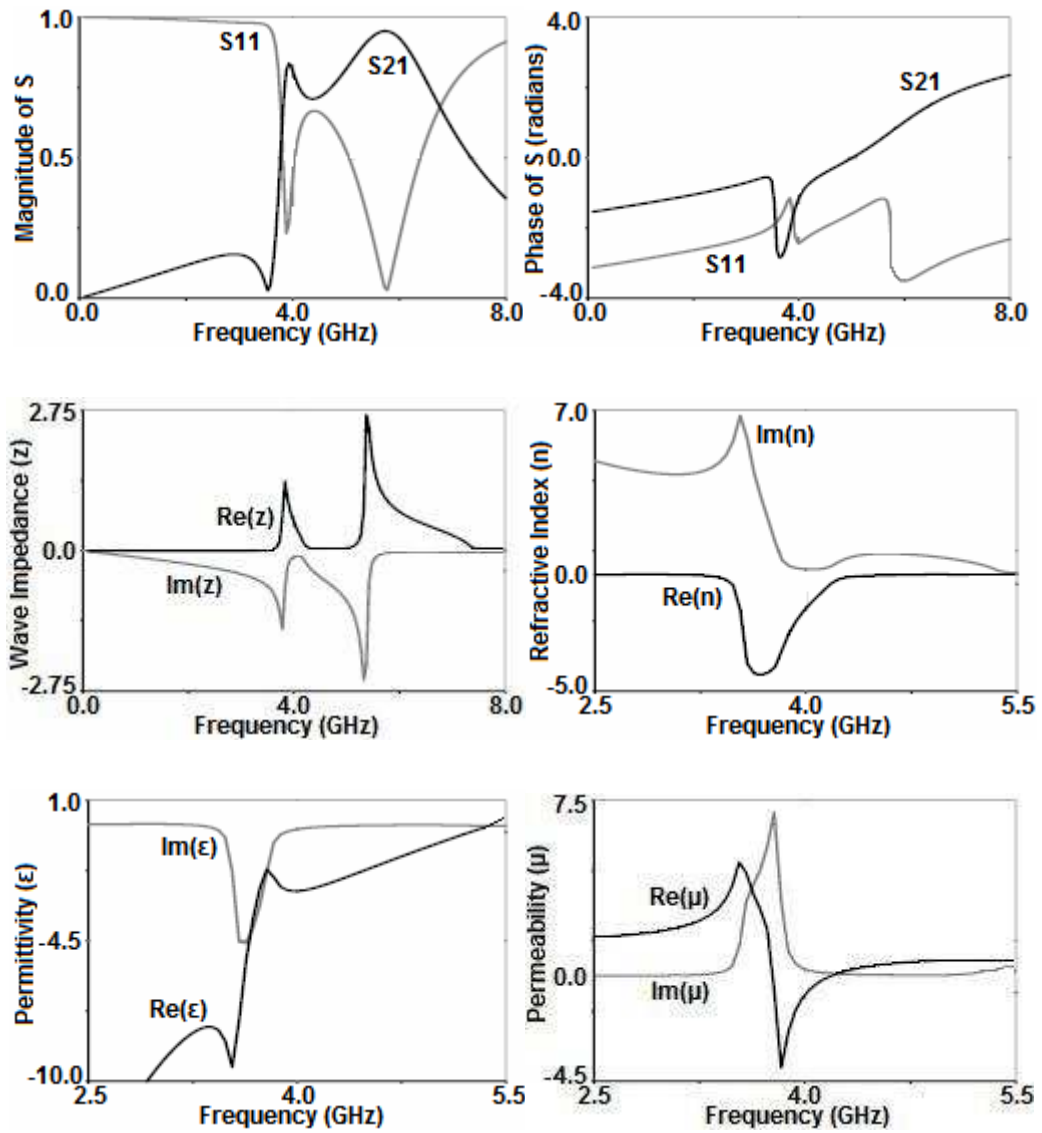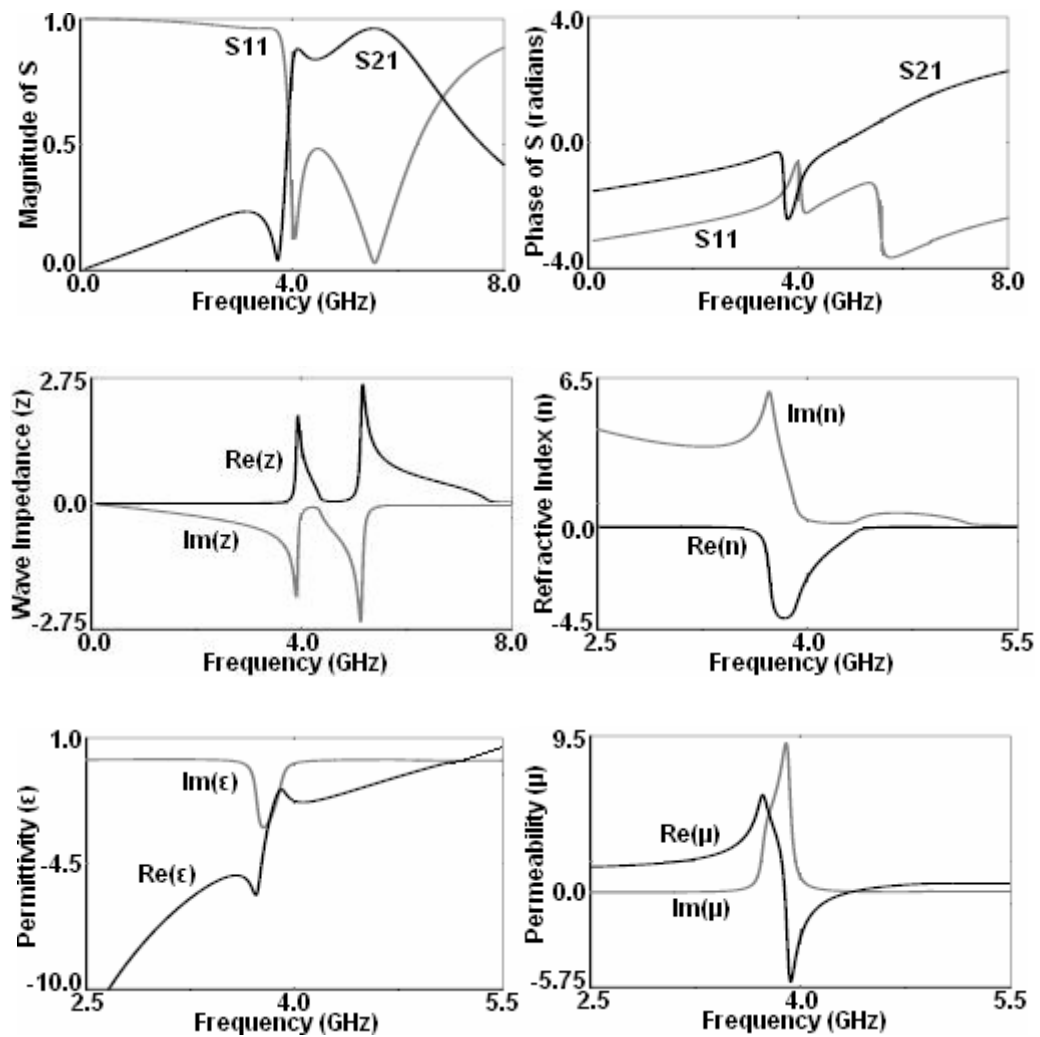

Figure 6.7: Magnitude and phase of S parameters, real and imaginary parts of the wave impedance, refractive index, permittivity and permeability for MTM3.
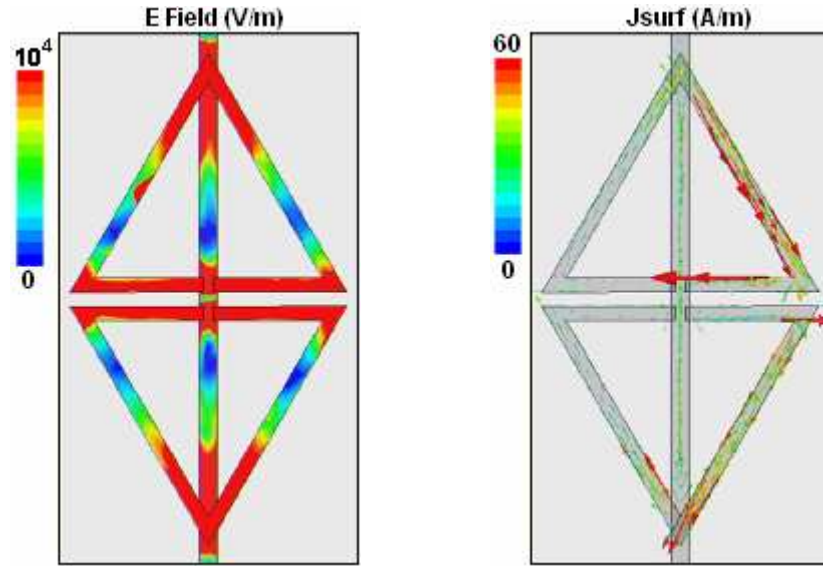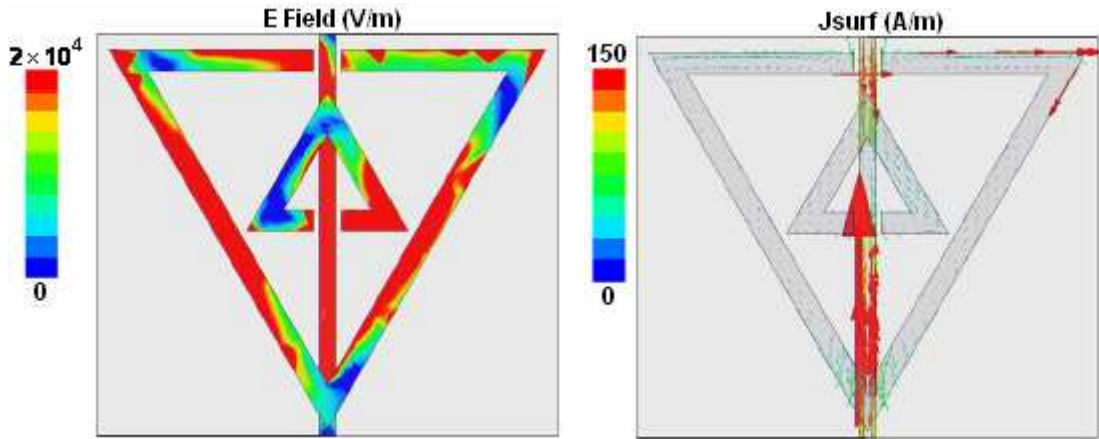
Figure 6.8: Electric field and surface current density for MTM3.

6.3 Construction of Physical Metamaterial Unit Cell

In the previous section, three types of new DNG metamaterials using TSRR and WS are created by means of the known DNG metamaterials studied in the literature. Here, it will be used the actual size to create the new DNG metamaterial using TSRR and WS. MTM1 shown in Figure 6.1(a) is used in the construction. The shape, geometry, and all dimensions are the same as in MTM1 given in Section 6.2.1 except the thicknesses. The thicknesses of FR4, TSRR, and WS are 1.0 mm, 0.125 mm, and 0.125 mm, respectively. This kind of FR4 substrate is used because it is found only such class of substrate in the market. The simulation result of the refractive index for this DNG metamaterial (MTM4) is shown in Figure 6.9. It can be observed that the refractive index of this physical metamaterials (MTM4) shows the mixed Lorentz-Drude response as explained in Chapter 3. According to the simulation, the negative region for the real part of the refractive index stands between the 3.23 GHz and 4.43 GHz. In addition, from the simulation, it can be found that the magnetic plasma frequency f_{mp} = 4 GHz, the electric plasma frequency f_{ep} = 5.1 GHz, the magnetic resonance frequency f_{mo} = 3.7 GHz, and the electric and magnetic damping frequencies $\delta_e = \delta_m = \delta$ = 0.23 GHz according to the theory given in the same chapter. These frequencies are used to calculate the refractive index analytically for MTM4 using the formulation of Chapter 3. Calculated refractive index for MTM4 is given in Figure 6.10. As it can be seen from Figure 6.9 and Figure 6.10, although the

simulated and calculated frequency responses of the refractive index are similar, there are some differences between them. In the calculations, the refractive index is computed based on the assumption explained in Chapter 3 (mixed Lorentz-Drude combination). These differences are caused by this assumption. However, this calculated example gives some aspect that the behavior of the refractive index is analogous in the calculations, simulations, and measurements.
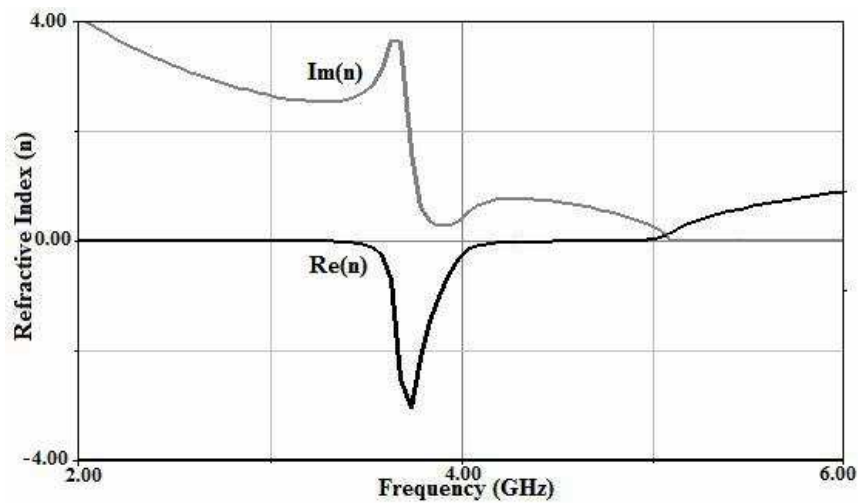
Figure 6.9: Real and imaginary parts of the refractive index for simulated MTM4.
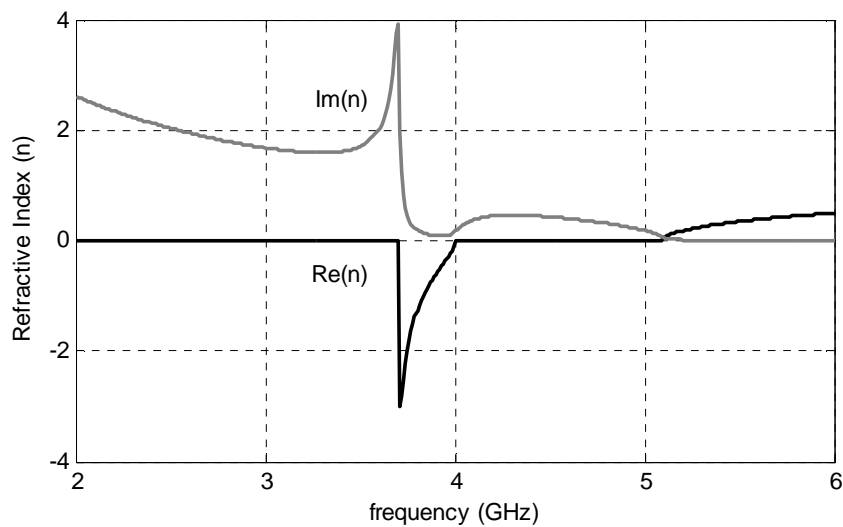
Figure 6.10: Calculated refractive index for MTM4 with $f_{mp} = 4$ GHz, $f_{ep} = 5.1$ GHz, $f_{mo} = 3.7$ GHz, and $\delta_e = \delta_m = \delta = 0.23$ GHz.

6.4 Manufacturing of New Metamaterial consist of TSRR and WS

In this part, the production of new metamaterial are given with the use of the results obtained in the previous section. FR4 substrate can be processed to create single and double faced metamaterials. Here, it is struggled with the double faced metamaterial. In this form, the TSRRs are located on one face of FR4 substrate and WSs are situated on the opposite face. In the industry, there are lots of techniques to produce metamaterials such as positive-20, serigraphy, drawing with the printed circuit pen, hot-press, and etc. The most preferred method is the hot-press technique among them. The hot-press technique is used to produce the novel metamaterial slabs in this thesis. The stages of the production are given in the following form:

- Drawing of the printed circuit scheme in the computer

- Print out the drawing to the transfer film papers using laser printer

- Transferring the printed drawing to FR4

- Melting the copper using the chemical operation

Drawing in the computer, the first step, forms the most important stage of the production. Recently, several types of programs are used for the drawing purpose. The printed circuit scheme can be obtained automatically by using one of them. Besides these programs, this scheme can also be achieved by hand drawing if the scheme is easy to draw and the drawer is professional. At the end of drawing, the pattern of the conductor ways which provide the connection between the components and the location plan of the components on FR4 are appeared. The sample figure for the printed circuit scheme of designed metamaterial can be seen in Figure 6.11. Note that, the TSRRs are placed on the front face and WSs are placed on the back face.

After completing the printed circuit scheme, the print out which include only conductor ways has to be taken. The aim of the hot-press technique is to transfer the toner to the selected paper. Due to this reason, the type of the paper is very important in this technique. There are special transfer papers in the market for such works. The PnP transfer films are used as a special transfer papers in this work. In addition, photograph, glossy, and acetate papers can be used to take the print out the scheme. However, to obtain well metamaterials, the used transfer papers have to be in a good quality. The PnP transfer films are the best quality papers in the market. Furthermore, the resolution of the laser printer has to be 1200 dpi to get good print out. Figure 6.12 shows the front and back views of printed scheme using 1200 dpi laser printer. In the print out, the ways of the components are covered with toner and other parts are completely empty. The scheme in the printed papers has to be the mirror image of the real scheme. Note that, multi-pieces of metamaterial shown in Figure 6.12 can be printed on a transfer paper in one print out process.
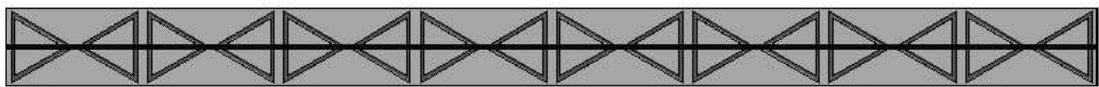
Figure 6.11: Printed circuit scheme of the designed metamaterial.

(a)

(b)
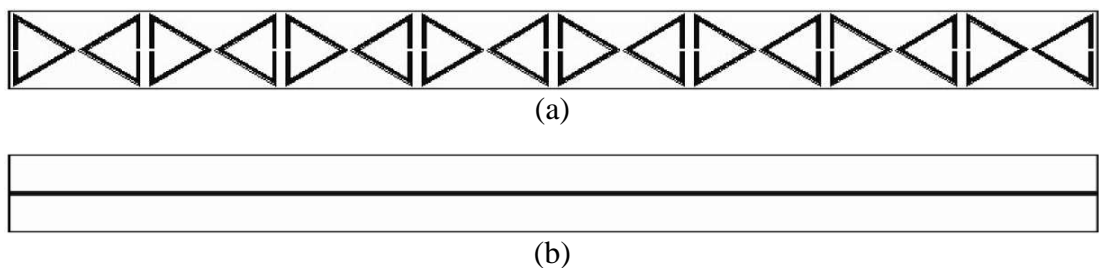
Figure 6.12: Print out of the metamaterial scheme, a) front view, b) back view.

In the third step, transferring process is happened by the interaction of heat with toner. To provide the required heat, it is necessary to use the old model flatiron with no heat. Before the hot-press, FR4 substrate must be cleaned with water and then

copper faces must be rubbed with thin sandpaper (emery paper). A cleaned and rubbed FR4 substrate is illustrated in Figure 6.13. To start to the transferring process, PnP transfer films are positioned on the copper faces of FR4 substrate and they are glued with the sticker at the edged. The flatiron is arranged to provide required heat. The best arrangement is turning the screw to the high level. Then, the transfer papers are ironed with the circular movements. Thus, the heat is distributed uniformly on FR4. Transfer papers can be removed after enough ironing. It takes at least 3 or 5 minutes. Removing process can be done slowly during the ironing or it can be done after FR4 and transfer papers cooled. Figure 6.14 shows the pictures of the front and back views of new metamaterial after completing the transferring process. If toner is not transferred so good to the FR4 substrate and there are broken ways, the necessary corrections can be made by using the printed circuit pens.
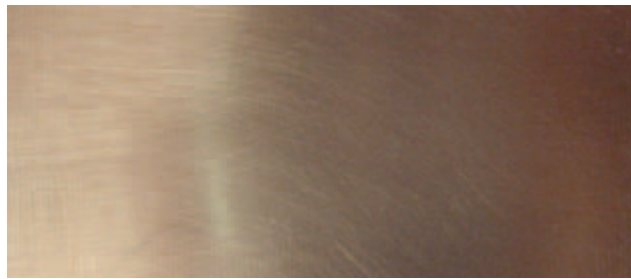
Figure 6.13: A cleaned and rubbed FR4 substrate.
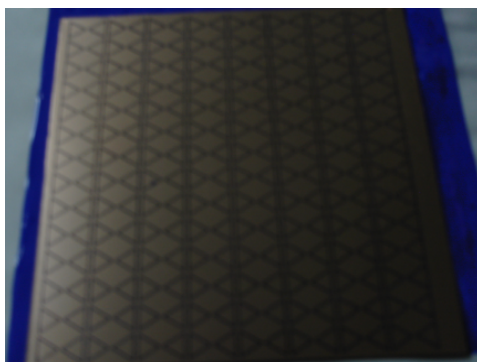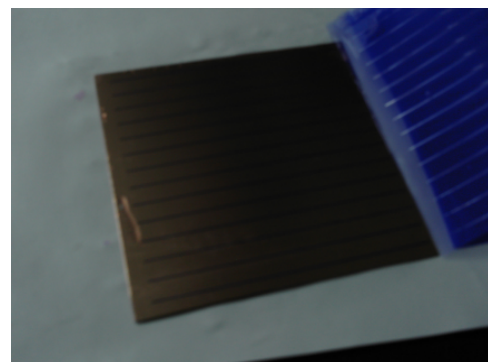
Front   Back

Figure 6.14: Front and back views of new metamaterial after transferring process.

In the last step, the copper without toner (empty part) is melted using chemical process. To do this, the mixture of hydrochloric acid and diluted hydrogen peroxide (perhydrol) is used. The ratio of the hydrochloric acid to the perhydrol must be 4/1. The mixture is prepared in the plastic container and FR4 substrate is left into the container. The container can be swung slowly from left to right to speed up the solubility. The melting process can be seen from Figure 6.15. The gas appeared during the chemical reaction must not be breathed. In addition, it is necessary to not touch to the mixture by hand or metal things. The chemical process has to be done with wearing gloves in open air or out door. After a few minutes, the substrate is removed from the container and cleaned with water using a sponge. Figure 6.16 presents new metamaterial after the chemical and cleaning processes. As it is seen from this figure, the conductor ways with toner is not affected from the chemical mixture. So that, the printed circuit scheme of new metamaterial which is drawn in the computer is transferred to FR4 substrate by using the chemical process. Finally, the produced substrate can be sliced according to the desired size.
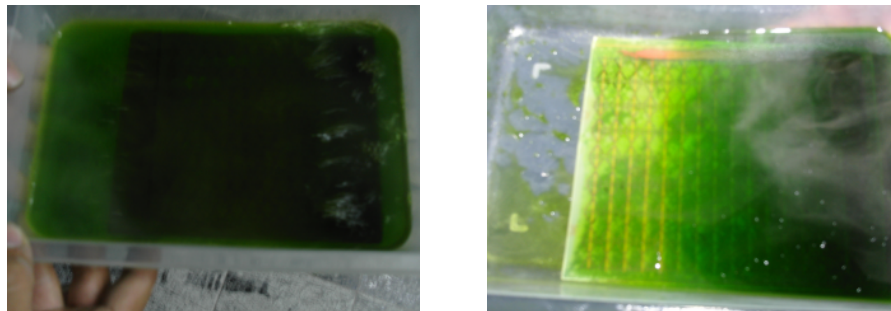
Figure 6.15: Melting process with the use of chemical mixture.
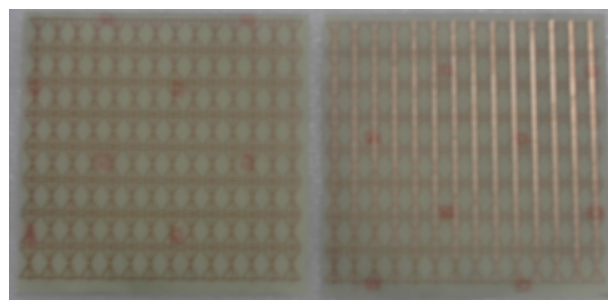
Figure 6.16: New metamaterial after the chemical and cleaning processes.

6.5 Transmission Experiments

In this section, some transmission experiments of new metamaterial are provided. All experiments were done in Nanotechnology Research Center (NANOTAM) at Bilkent University. The transmission spectra of manufactured novel metamaterial are performed in free space by using an Agilent Technology N5230A network analyzer. Two monopole antennas were used in the experiments to transmit and detect the electromagnetic waves through the metamaterial sample. The monopole antennas had been constructed by removing the shield around one end of a microwave coaxial cable. The exposed centre conductor, which is also acted as the transmitter and receiver, was 2 mm long. This length is on the order of $\lambda/2$, arranged to work at a frequency range covering resonance frequencies. Monopole antennas were then connected to the network analyzer to measure the transmission characteristic of the novel metamaterial. The schematic representation of experimental setup is shown in Figure 6.17. For all measurements, electromagnetic wave propagates along the x direction. The electric field polarization is kept along the y axis, and magnetic field polarization is kept along z axis. Shortly, the incident field has wave-vector k, electric field E, and magnetic field H, along x, y, and z directions, respectively.
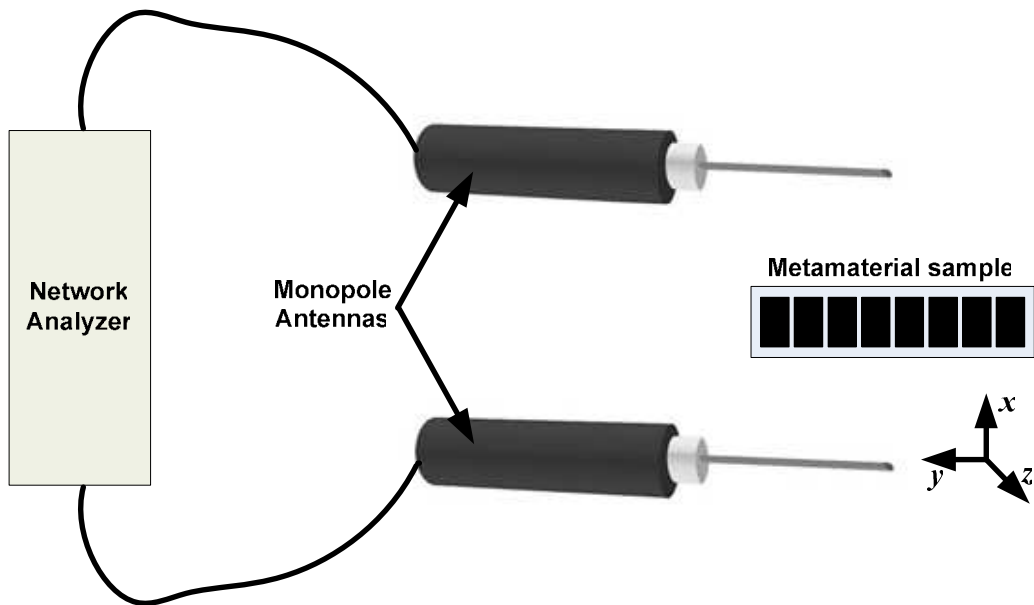
Figure 6.17: Schematic drawing of the experimental setup.

The absorber units were used during the experiments to get rid of unwanted reflections. All measurements were performed in free space (air) rather than a waveguide environment. In our experiments, we first measured the transmission spectra in free space without metamaterial sample. These data was used as the calibration data for the network analyzer. Then, novel metamaterial samples were inserted between monopole antennas, and we performed the transmission measurements by maintaining the distance between the transmitter and receiver monopole antennas fixed as shown in the figure given below. Note that, all transmission measurements are normalized to unity.

In the first experiment, we measured the transmission spectrum of one metamaterial slab comprised of 8 unit cells as shown in Figure 6.11. There are 16 TSRRs and one WS in this slab. The measured transmission characteristic of one metamaterial slab is displayed in Figure 6.18. The frequency response of the transmission for one metamaterial slab shows similar behavior as in Figure 4.11(b). The frequency response of the transmission has a non-fixed characteristic as in the numerical results of Lorentz medium slab. Thus, it can be said that the experimental result for one metamaterial slab comprised of TSRRs and WS agrees with the numerical results obtained for Lorentz medium slab in Chapter 4. Here, the main important point is that the high transmission band is in the negative region or not. According to the simulation results given in Figure 6.9, the negative band stands between 3.23 GHz and 4.43 GHz. The negative band for one metamaterial slab consists of 8 unit cells lies approximately in the same region of the simulation result given in Figure 6.9. Consequently, it can be said that the high transmission occurs in the negative region where our novel periodic structure works as a DNG metamaterial. Note that, the measured high transmission peak is not in the calculated negative region (3.7 GHz – 4 GHz) shown in Figure 6.10. In the calculation, the permittivity and permeability are computed using mathematical formulations given in Chapter 3. Thus, the negative region is calculated using these mathematical approximations. In the real case, the permittivity and permeability are not exactly equal to the approximated parameters. Also, there are not accurate mathematical functions to express the permittivity and permeability of real metamaterials in the literature. As a result, the measured transmission spectrum can not be involved in the

calculated negative region. But, it must be in negative region obtained from the simulation results.
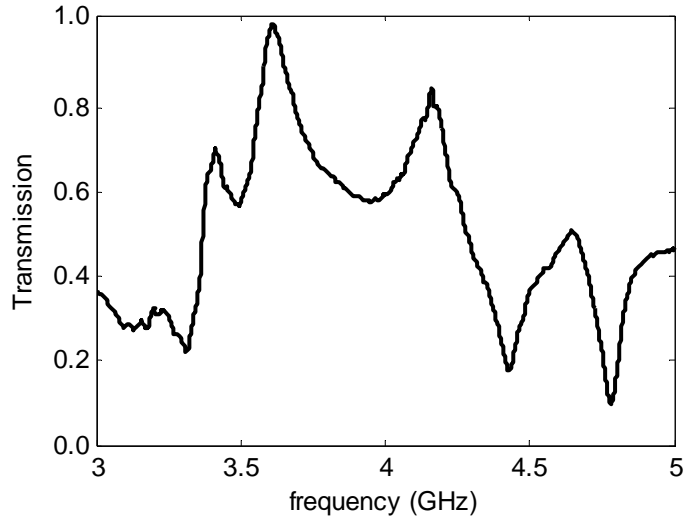
Figure 6.18: Measured transmission spectrum of one metamaterial slab comprised of 8 unit cells.

In the second experiment, the transmission spectrum of one metamaterial slab with two columns is measured. This metamaterial slab with two columns consists of 16 unit cells is shown in Figure 6.19. For this metamaterial slab, the measured transmission characteristic versus the frequency is illustrated in Figure 6.20. In this measurement, a transmission band is observed between 3.23 GHz and 4.43 GHz which is agree with the negative region obtained from simulation. The transmission peak is measured to be nearly unity at 3.796 GHz. This peak stands in the negative region obtained from calculated and simulated results. Therefore, it can be said that the calculated and simulated results agree with each other for the one metamaterial slab with two columns consists of 16 unit cells.
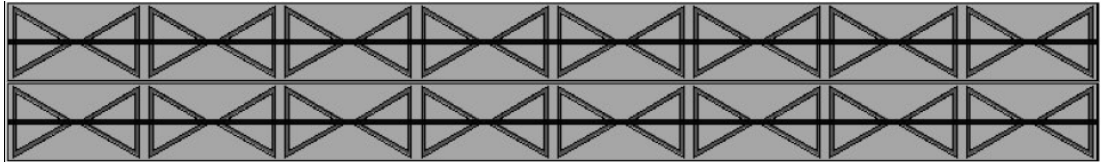
Figure 6.19: Schematic representation of one metamaterial slab with two columns consists of 16 unit cells.
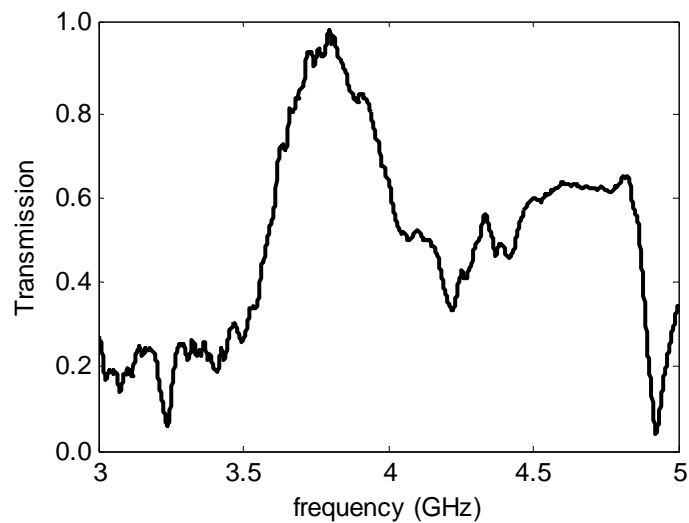
Figure 6.20: Measured transmission characteristic versus the frequency for one metamaterial slab with two columns consists of 16 unit cells.

Figure 6.21 shows the measured transmission spectra for one metamaterial slab with 8 unit cells (one column) and 16 unit cells (two columns), respectively. Gray line corresponds to 8 unit cells and black line corresponds to 16 unit cells. As it is clearly observed from the figure, the measured transmission peak shifts to the right from 3.614 GHz to 3.796 GHz when metamaterial slab has 16 unit cells. In addition, the high transmission band is wider in the 16 unit cell metamaterial slab.
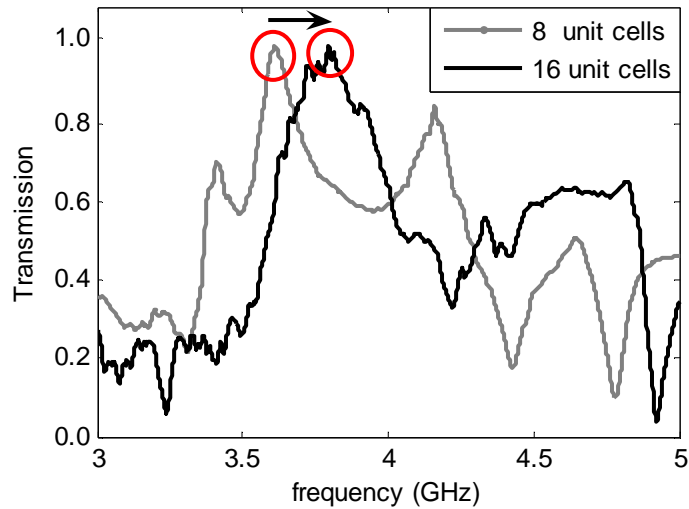
Figure 6.21: Measured transmission spectra for one metamaterial slab with 8 unit cells (one column) and 16 unit cells (two columns). Gray line corresponds to 8 unit cells and black line corresponds to 16 unit cells.

As the third experiment, the transmission measurement for multilayer metamaterial slabs is considered. To do this, two new metamaterial slabs is arranged consecutively with 2 mm spacing between them. It means that there are 3 layers in the environment consisted of two metamaterial slabs and one dielectric (air) slab. The dielectric slab is embedded between two metamaterial slabs. The measured transmission spectrum for this three layered structure is presented in Figure 6.22. The high transmission band stands in the negative region as it is expected. The measured spectrum is in agreement with the numerical results obtained in Chapter 5. The measured result offers to design a high transmission filters as in the numerical results obtained in Chapter 5. All pass filters for the negative region and/or band pass filter for the desired frequency region can be designed and manufactured using the measured results obtained here.
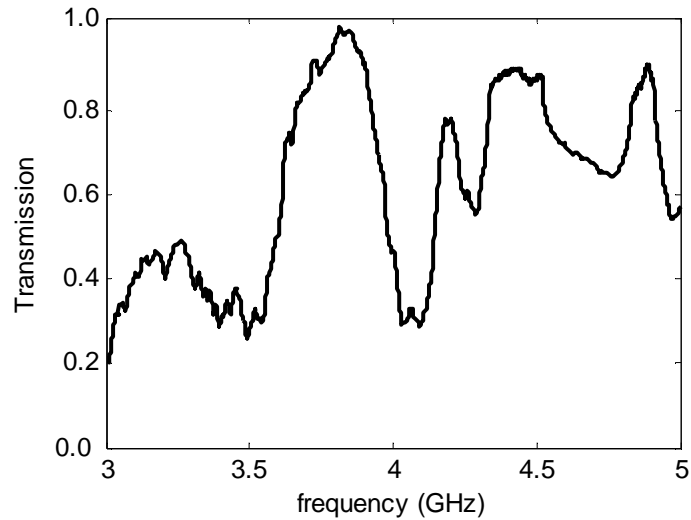
Figure 6.22: Measured transmission spectrum for two consecutive metamaterial slabs with 2 mm spacing.

Our forth experiment was arranged to study the effect of the spacing between the layered structure used in the previous experiment. All arrangements are the same with the previous experiment except the spacing. Here, it is increased from 2mm to 4 mm. The measured transmission spectrum for this structure is displayed in Figure 6.23. The high transmission band again stands in the negative region and the measurement agrees with results obtained in Chapter 5. This result suggests to construct the high transmission filters using the new metamaterial as recommended in the numerical results obtained in Chapter 5. The results of this and previous experiments are plotted together and they are illustrated in Figure 6.24 for comparison purpose. Gray line corresponds to the structure arranged with 2 mm spacing and black line corresponds to the structure arranged with 4 mm spacing. As it is observed from this figure, the high transmission interval is wider in the 4 mm spacing experiment. Thus, it can be concluded that if suitable dielectric slab thickness between the two metamaterials is arranged the widest transmission band can be obtained. Then, more efficient transmission filters can be designed and fabricated.
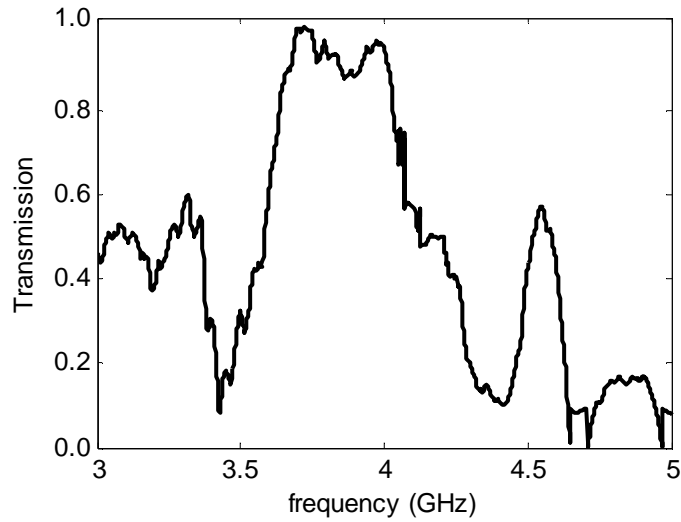
Figure 6.23: Measured transmission spectrum for two consecutive metamaterial slabs with 4 mm spacing.
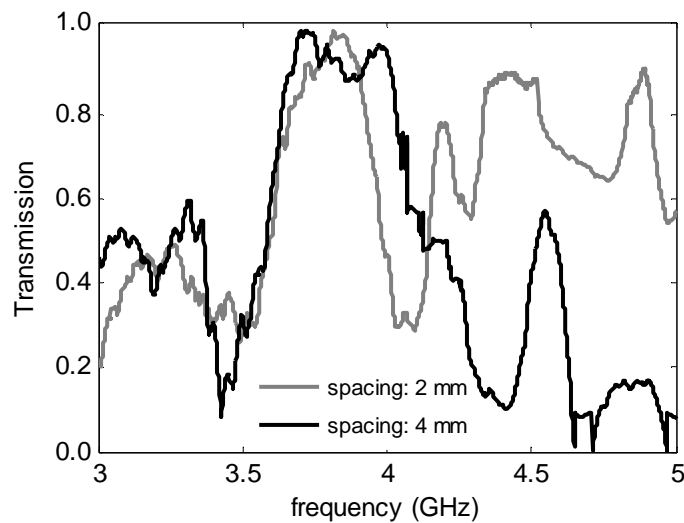
Figure 6.24: Measured transmission spectra for two consecutive metamaterial slabs with 2 mm and 4 mm spacing. Gray line corresponds to 2 mm spacing and black line corresponds to 4 mm spacing.

In the fifth experiment, we tried to construct five layered configuration to observe the transmission characteristic. For this reason, we combined three metamaterial slabs with 2 mm spacing. The measured transmission spectrum for this

structure is demonstrated in Figure 6.25. Once again, the high transmission peak is observed in the negative region at 3.717 GHz. The transmission bandwidth of the negative region is narrower than the transmission bandwidth achieved in the previous experiment.
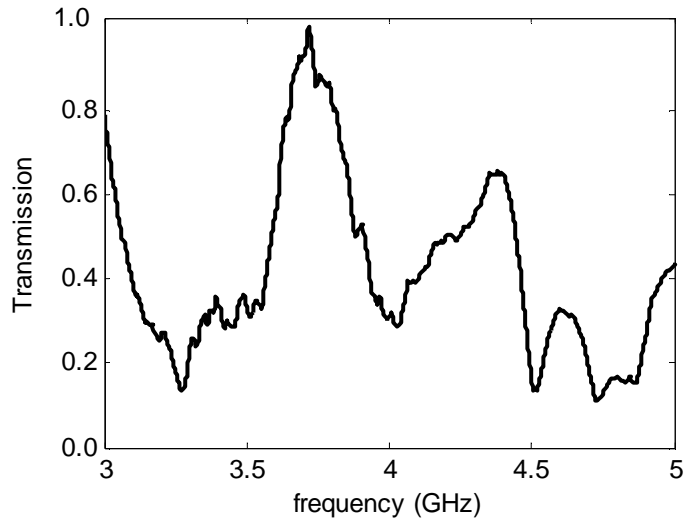
Figure 6.25: Measured transmission spectrum for five layered configuration comprised of three metamaterial slabs and two dielectric (air) layers.

In the last experiment, seven layered structure was constructed for measuring the transmission spectrum. To do this, four metamaterial slabs with 2 mm spacing are combined together. Figure 6.26 presents the transmission spectrum for this seven layered structure. The transmission peak is achieved in the negative region at 3.717 GHz. This is the same frequency observed in the previous experiment. In addition, the transmission bandwidth obtained here is narrower than the previous experiment. Therefore, according to the measurements, the transmission bandwidth in the negative region is narrower when the number of layers is increased. It means that the transmission bandwidth is inversely proportional with the number of layers.
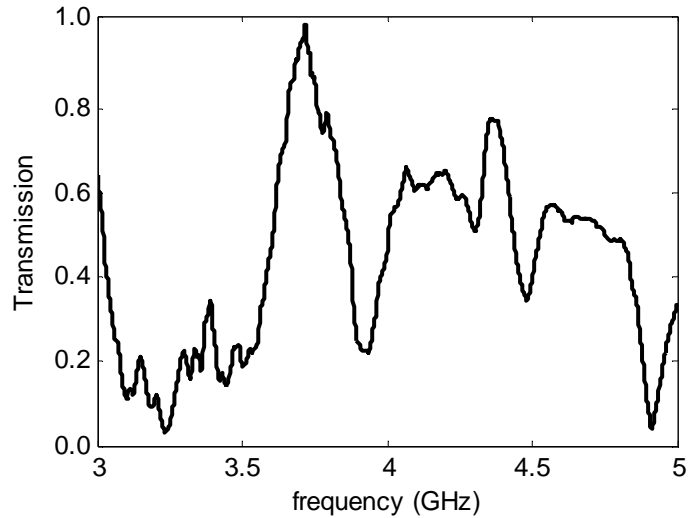
Figure 6.26: Measured transmission spectrum for seven layered configuration comprised of four metamaterial slabs and three dielectric (air) layers.

6.6 Summary and Discussion

In summary, this chapter has discussed the design, realization and manufacturing processes of the novel metamaterials consist of triangular split ring resonator (TSRR) and wire strip (WS). Three different types of new metamaterials were designed and simulated. According to the results obtained in this chapter, the designed metamaterials exhibited double negative properties in the frequency band of interest. It means that the modeled structures were well designed and successfully worked around the operation frequency. The metamaterial structures were designed to display double negative characteristics around 4 GHz. Note that, the negative frequency band can be retailored by rearranging the size and dimensions of the structures. Therefore, our novel metamaterials can provide new ways to design, characterize, and manufacture new metamaterials in the microwave, millimeter wave, and optical frequency regions. Then, the fabrication processes to manufacture new metamaterial slabs were explained in detail. Finally, some transmission experiments were provided using the manufactured slabs to observe the transmission

characteristics of the multilayer structure comprised of new metamaterial slabs and dielectric (air) layers. In the transmission spectra, high transmission peak was achieved in the negative region as it was expected. The incident waves were nearly transmitted through the constructed structures without being reflected at the metamaterial – air interface at the negative region. The low reflection from the surface can be attributed to either matched impedance at the interface or the thickness of the slabs. In addition, the transmission bandwidth in the negative region narrowed when the number of layers along the propagation direction is increased. This was expected due to the losses. As it is known that the losses increases if the number of layers is increased. The measured transmission spectra were also compared with the numerical results obtained in the previous chapters. It is observed that the experimental results agree with the numerical results. It means that the characteristics of the experimental and numerical results are approximately the same with each other. Furthermore, the results of this chapter propose to design, realize, and manufacture transmission coatings and filters with high efficiency at the millimeter wave, optical, and microwave regimes as it is recommended in the numerical results acquired in previous chapters.

CHAPTER 7

CONCLUSION

In this thesis, analysis, some applications, and a novel design of double negative metamaterials have been investigated. In this chapter, a brief summary of the investigation and the results of thesis work are presented. In addition, some future directions are mentioned in the base of the results found.

The first two chapters concerned with the basic information of the double negative metamaterials. In Chapter 1, some definitions of double negative metamaterials, historical background, and thesis motivation were given. The detail literature search was presented and some terminologies about double negative metamaterials are explained. In the second chapter, main electromagnetic properties of double negative metamaterials were explicated and discussed. Dispersion characteristics and plane waves in such medium were described. In addition, the concept of negative refraction was clarified and some examples from the literature were shown.

In the third chapter, classification and realization of double negative metamaterials were given to understand the characteristic features of them. Both the analytical and physical models were presented to identify how double negative metamaterials can be constructed. These were very important because the design and manufacturing processes were based on these aspects. Also, the theoretical and numerical analyses which were explained in the following chapters constructed in the base of the subject constructed in the third chapter.

Chapter 4 presented the wave propagation in the presence of double negative metamaterials. First of all, two adjacent semi infinite conventional and double negative media are examined. The case of normal, TE wave, and TM wave incidences are investigated. Then, double negative metamaterial slab embedded between two dielectric media was studied. This slab was characterized by using the concept explained in Chapter 3. The results obtained in this chapter showed that the manufacturing of anti-reflection and/or total-transmission coatings and/or filters was achievable by using the suitable design process. Furthermore, the combination of conventional dielectric and double negative media are simulated to illustrate the perfect lens and the parabolic wave refractor applications. It can be said that these combinations can be used to manufacture the new lenses and refractors. Finally, these results can be used to analyze, fabricate, and integrate the metamaterials in various structures.

Chapter 5 demonstrated the design and analysis of stratified structures containing double negative metamaterials. First, the theory of stratified structure consists of pure double negative metamaterials and the combinations of such materials with conventional dielectric materials are constructed. Then, several applications of stratified structure were presented. According to the results obtained here, distributed Bragg reflectors, high reflection and transmission coatings, band pass, stop band, anti-reflection, multi band-pass, multi saw-comb, oscillating, and multi notch filters can be constructed with high efficiency at the frequency regions where double negative metamaterial works.

In the last chapter, novel metamaterials are designed and manufactured using triangular split ring resonators and wire strips. Three new metamaterials are designed and simulated. The designed new metamaterials were successfully worked at the operation frequency. Then, the manufacturing processes were explained to construct new metamaterial slabs to make some experiments. After that, some transmission experiments were provided and the transmission characteristics of the new metamaterial slabs were illustrated. It is observed that the experimental agreed with

the numerical results. Moreover, the design and fabrication of high transmission coatings and filters using these novel metamaterials remain new topics for further study and it can be suggested as a future work.

The studies on the double negative metamaterials have been continuing to become a hot topic in the scientific and engineering communities due to the various potential applications of them. In the near future, the studies on the double negative metamaterials will be more commonplace by means of the modern engineering applications and technologies. However, several studies on the double negative metamaterials can be suggested for the present time. One of them can be the design and production of the highly efficient electromagnetic filters with the use of our novel double negative metamaterials as it is mentioned throughout the thesis work. Also, some multilayer structures consist of double negative metamaterials can be determined and arranged to obtain well-organized devices and apparatus. For example, tunable cold plasma layers can be constructed physically to obtain high transmission. In addition, new metamaterials can be created by playing with the shape and geometry of triangular split ring resonator. At present, our novel metamaterials can open a way to design, characterize, and manufacture new double negative metamaterials. Complementary triangular split ring resonators can be proposed as an example to create new types of metamaterials and the examples can be increased. Additionally, our novel metamaterials can be retailored to work at optical and millimeter frequency bands. Furthermore, perfect lenses and parabolic wave refractors can be realized and constructed since the verification of them were successfully provided in the simulation results. Moreover, there are no exact formulations for the permittivity and permeability of the physical metamaterials in the literature. There are only some approximations to define of them. The research to describe the new formulations or approximations for the permittivity and permeability of the physical metamaterials can also be suggested for the future work.

LIST OF PUBLICATIONS

1) Sabah C., Ögücü G., and Uckun S. (2006). Reflected and transmitted powers of electromagnetic wave through a double-negative slab. *Journal of Optoelectronics and Advanced Materials* (*JOAM*), **8**, 1925–1930.

2) Sabah C. and Uckun S. (2007). Electromagnetic wave propagation through the frequency-dispersive and lossy double-negative slab. *Opto-Electronics Review*, **15**, 133–143.

3) Sabah C. and Uckun S. (2007). Frequency response of multilayer media comprised of double-negative and double-positive slabs. *Chinese Physics Letters*, **24** (5), 1242–1244.

4) Sabah C. and Uckun S. (2007). Physical features of left-handed mirrors in millimeter wave band. *Journal of Optoelectronics and Advanced Materials* (*JOAM*), **9**, 2480–2484.

5) Sabah C. and Uckun S. (2007). Scattering characteristics of the stratified double-negative stacks using the frequency dispersive cold plasma medium. *Zeitschrift für Naturforschung A* (*A Journal of Physical Sciences*), **62a** (5), 247–253.

6) Sabah C. and Uckun S. (2008). Triangular split ring resonator and wire strip to form new metamaterial. Accepted for publication in the *Proceedings of XXIX General Assembly of the International Union of Radio Science*, Chicago, Illinois, USA, August 07-16, 2008.

In addition to these scientific articles, there are more papers submitted to the SCI journals and international conferences publications and they are under review right now.

APPENDIX

TRANSMISSION LINE MODELING METHOD FOR STRUCTURES CONTAINING DOUBLE NEGATIVE METAMATAERIALS

In this appendix, the transmission line modeling method (TLM) for DNG structures is examined. In Chapter 2, the reflection and transmission coefficients were determined by enforcing continuity of the tangential components of the electric and magnetic fields across the boundaries. Here the transmission line circuit components are derived to obtain the reflection and transmission coefficients. Note that, the transmission line circuit components are functions of the thickness of the dielectric layers, its electric and magnetic parameters and wave propagation factor inside the layers.

The boundary conditions at the junctions of the transmission lines specify that both the voltage and current be continuous across each junction. The boundary conditions for the plane wave interfaces force the tangential components of **E** and **H** to be continuous, and since $\mathbf{E} \cdot \boldsymbol{a}_N \leftrightarrow V$ and $\mathbf{H} \cdot \boldsymbol{a}_N \leftrightarrow I$, these two sets of boundary conditions are also equivalent. Note that, $\boldsymbol{a}_N$ ($N = x, y, z$) are the unit vectors tangential to the reflecting interface.

The transmission line equivalent circuit for two semi-infinite media formed from DPS and DNG materials shown in figures 4.1, 4.3, and 4.5 is very simple and it is shown in Figure A.1.
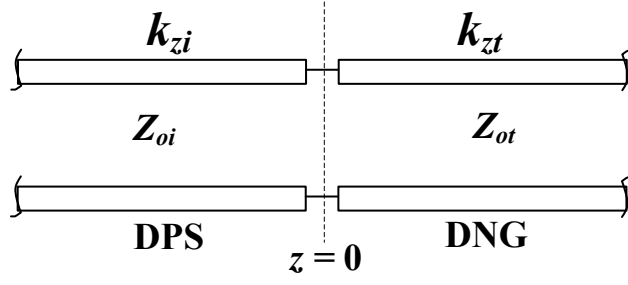
Figure A.1: Transmission line equivalent model of two semi-infinite media formed from DPS and DNG materials.

The reflection and transmission coefficients can easily be found as follows:

$$R = \frac{Z_{ot} - Z_{oi}}{Z_{ot} + Z_{oi}} \tag{A.1a}$$

$$T = 1 + R = \frac{2Z_{ot}}{Z_{ot} + Z_{oi}} \tag{A.1b}$$

where Z_{oi} and Z_{ot} are the characteristics impedances of the incident and transmitted media. The main important point is to write the characteristic impedances for normal and oblique (TE and TM) incidences. These are given in the following equations.

$$\left. \begin{array}{l} Z_{oi} = Z_i \\ \\ Z_{ot} = Z_t \end{array} \right\} \text{ for normal incidence} \tag{A.2a}$$

$$Z_{oi} = \frac{Z_i}{\cos\theta_i}$$
$$Z_{ot} = \frac{Z_t}{\cos\theta_t}$$
for TE wave incidence (A.2b)

$$Z_{oi} = Z_i \cos\theta_i$$
$$Z_{ot} = Z_t \cos\theta_t$$
for TM wave incidence (A.2c)

where $Z_i = \sqrt{\mu_i/\varepsilon_i}$ and $Z_t = \sqrt{\mu_t/\varepsilon_t}$ are the wave impedances of DPS and DNG media. At present, some numerical examples are illustrated in figures A.2, A.3, and A.4 to validate the results obtained in sections 4.2, 4.3, and 4.4. The results in these sections were obtained recursively as explained in the in Chapter 4. Here, the figures 4.2, 4.4, and 4.6 are reproduced using TLM and recursive method (RM). As it is seen from these figures, TLM and RM give the same numerical results. Thus, the results are verified and validated using two methods.
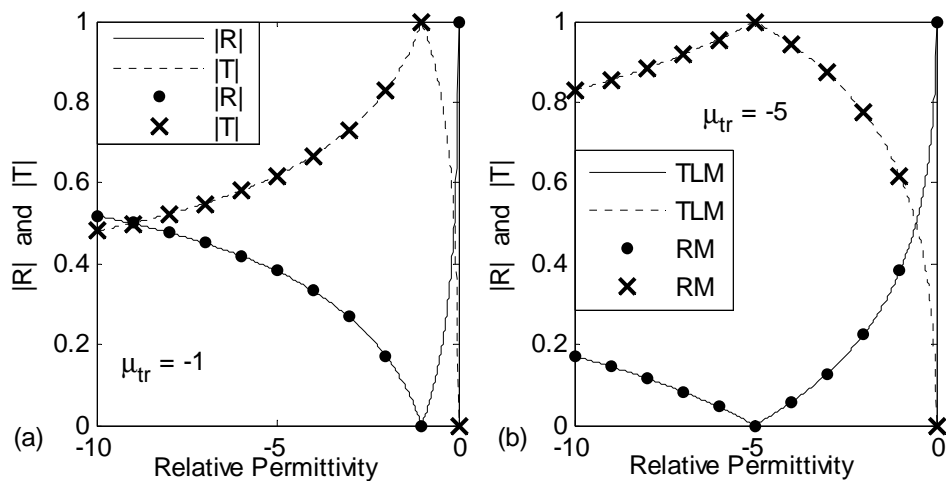
Figure A.2: Reproduction of Figure 4.2 using TLM and RM.
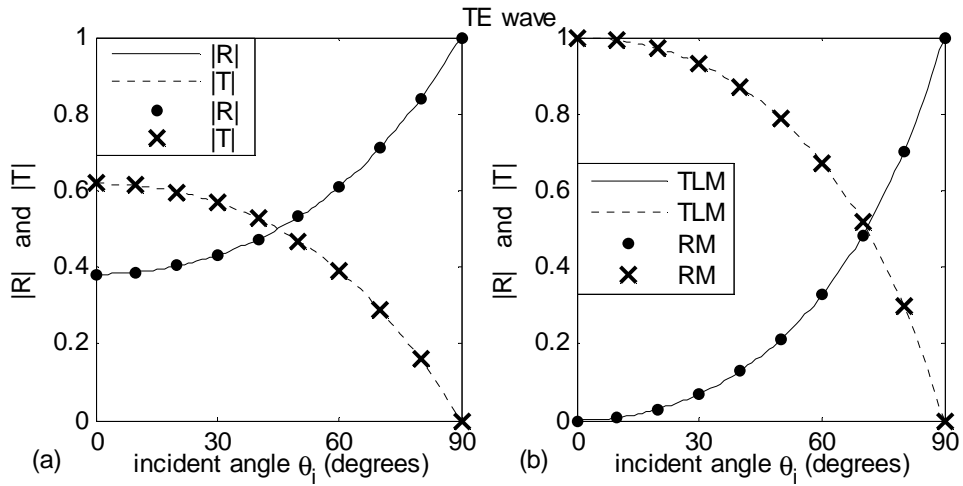
Figure A.3: Reproduction of Figure 4.4 using TLM and RM.
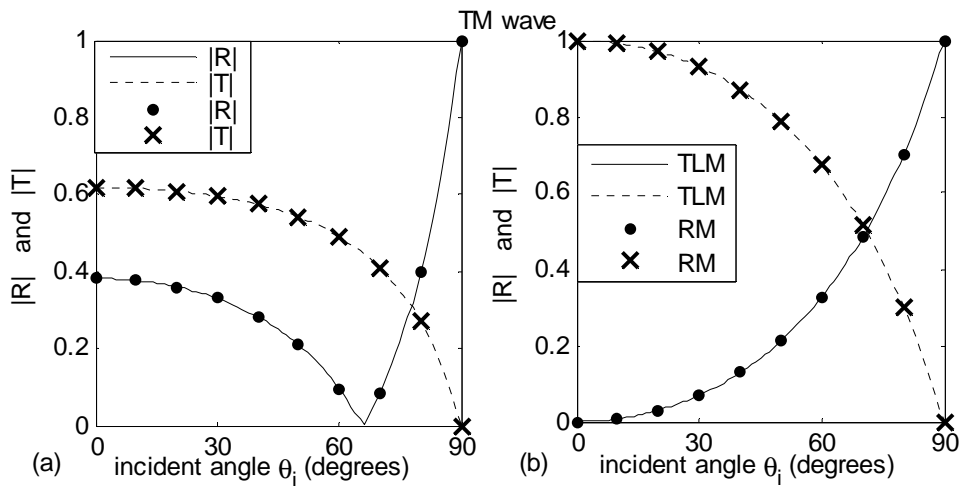
Figure A.4: Reproduction of Figure 4.6 using TLM and RM.

Now, the electromagnetic wave propagation through the DNS which was studied in section 4.5 is considered. Figure 4.7 shows the geometry of the problem. The theoretical formulations are achieved recursively and numerical results are specified using this recursive method in section 4.5. Now, these formulations and numerical results will be obtained using TLM. The transmission line equivalent of Figure 4.7 is shown in Figure A.5.
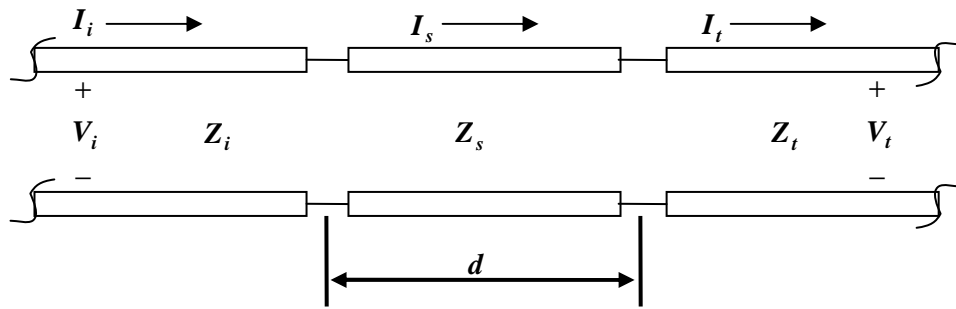
Figure A.5: Transmission line equivalent model of DNS between two different dielectric media.

If the input potential difference (V_i) indicated in the figure above is normalized to the value of one and Figure A.5 is rearranged, the simple form can be obtained. This form is illustrated in Figure A.6.
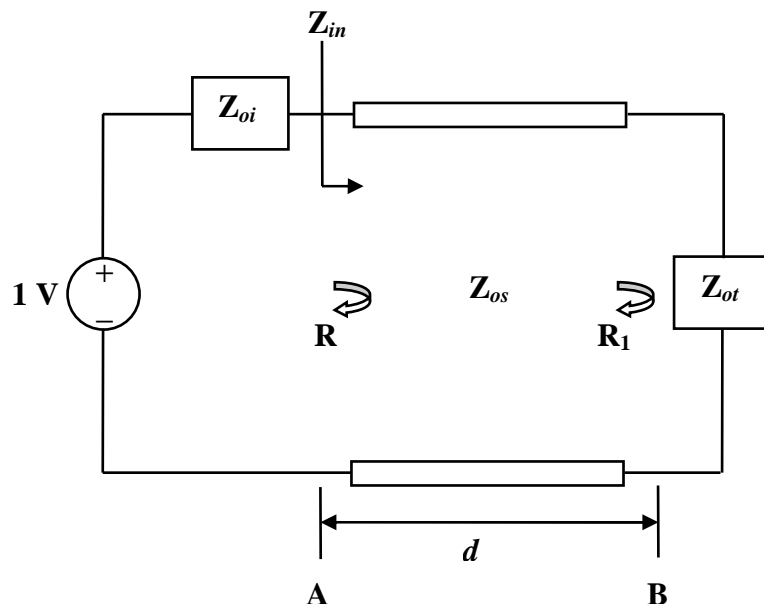
Figure A.6: Reorganized form of Figure A.5.

In Figure A.6, Z_{in} represents the input impedance at point A; Z_{oi}, Z_{os}, and Z_{ot} are the characteristics impedances of the incident, slab, and transmitted media; R is the total

reflection coefficient, and R_1 is the reflection coefficient at point B. If the transmission line given in Figure A.6 is analyzed and solved, the following equations can easily be obtained. First of all, the input impedance at point A can be given as:

$$Z_{in} = Z_{os} \frac{Z_{ot} + jZ_{os} \tan(k_{sz}d)}{Z_{os} + jZ_{ot} \tan(k_{sz}d)} .$$

(A.3)

Thus, the total reflection coefficient for the whole structure can be specified as follows:

$$R = \frac{Z_{in} - Z_{oi}}{Z_{in} + Z_{oi}} .$$

(A.4)

Then, the reflection coefficient at point B can be given as:

$$R_1 = \frac{Z_{ot} - Z_{os}}{Z_{ot} + Z_{os}} .$$

(A.5)

The potential difference and current between the points A and B can be written as follows:

$$V(z) = V^+ \left[\exp(-jk_{sz}z) + R_1 \exp(jk_{sz}z) \right]$$

(A.6a)

$$I(z) = \frac{V^+}{Z_{os}} \left[\exp(-jk_{sz}z) - R_1 \exp(jk_{sz}z) \right]$$ (A.6b)

where V^+ shows the amplitude of the forward wave. Afterward, the potential difference at the point A can be given as in Equation (A.7).

$$V_A = \frac{Z_{in}}{Z_{in} + Z_{oi}} = V^+ \left[\exp(jk_{sz}z) + R_1 \exp(-jk_{sz}z) \right]$$ (A.7)

Using above equation, the amplitude V^+ can be found as:

$$V^+ = \frac{Z_{in}}{Z_{in} + Z_{oi}} \frac{1}{\left[\exp(jk_{sz}z) + R_1 \exp(-jk_{sz}z) \right]}$$ (A.8)

Therefore, the potential difference and the current at the point B can be formulated as in Equation (A.9a) and Equation (A.9b).

$$V_B = V^+(1 + R_1) = \frac{Z_{in}}{Z_{in} + Z_{oi}} \frac{1}{\left[\exp(jk_{sz}z) + R_1 \exp(-jk_{sz}z) \right]} (1 + R_1)$$ (A.9a)

$$I_B = \frac{1 - R_1}{Z_{os}} \left\{ \frac{Z_{in}}{Z_{in} + Z_{oi}} \frac{1}{\left[\exp(jk_{sz}z) + R_1 \exp(-jk_{sz}z) \right]} \right\}.$$ (A.9b)

At this point, we can define the output impedance at point B as follows:

$$Z_{out} = \frac{1 - V_B}{I_B}.$$ (A.10)

At last the reflection coefficient at the output and the transmission coefficient for whole structure can be formulated as in Equation (A.11).

$$R_{out} = \frac{Z_{ot} - Z_{out}}{Z_{ot} + Z_{out}}$$ (A.11a)

$$T = 1 + R_{out} = \frac{2Z_{ot}}{Z_{ot} + Z_{out}}.$$ (A.11b)

Therefore, the total reflection and transmission coefficients for DNS embedded between two different DPS media were found and formulated as in Equation (A.4) and Equation (A.11b). Note that, the characteristic impedances for normal and oblique incidences are given in Equation (A.2) for Z_{oi} and Z_{ot}. The characteristic impedance Z_{os} for normal and oblique (TE and TM) incidences can be written as:

$$Z_{os} = Z_i \rightarrow \text{ for normal incidence}$$

$$Z_{os} = \frac{Z_s}{\cos\theta_s} \rightarrow \text{ for TE wave incidence} \quad .$$ (A.12)

$$Z_{os} = Z_s \cos\theta_s \rightarrow \text{ for TM wave incidence}$$

where $Z_s = \sqrt{\mu_s/\varepsilon_s}$ is the wave impedance of DNS. Now, reproduction of Figure 4.8(f), Figure 4.11(a), and Figure 4.11(b) are illustrated in figures A.7 and A.8. Here, the mentioned figures in Chapter 4 are reproduced using TLM and RM. As it is seen from reproduced figures, the same numerical results are achieved using TLM and RM. Thus, the results are verified and validated using two methods.
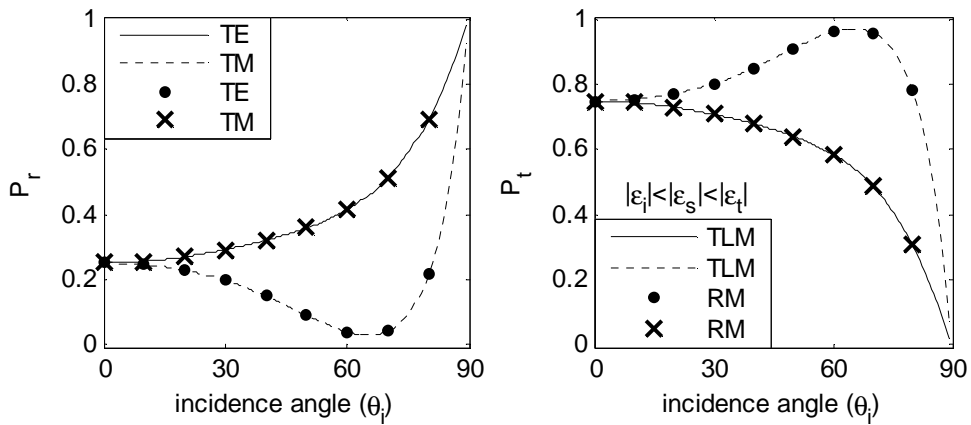
Figure A.7: Reproduction of Figure 4.8(f) using TLM and RM.
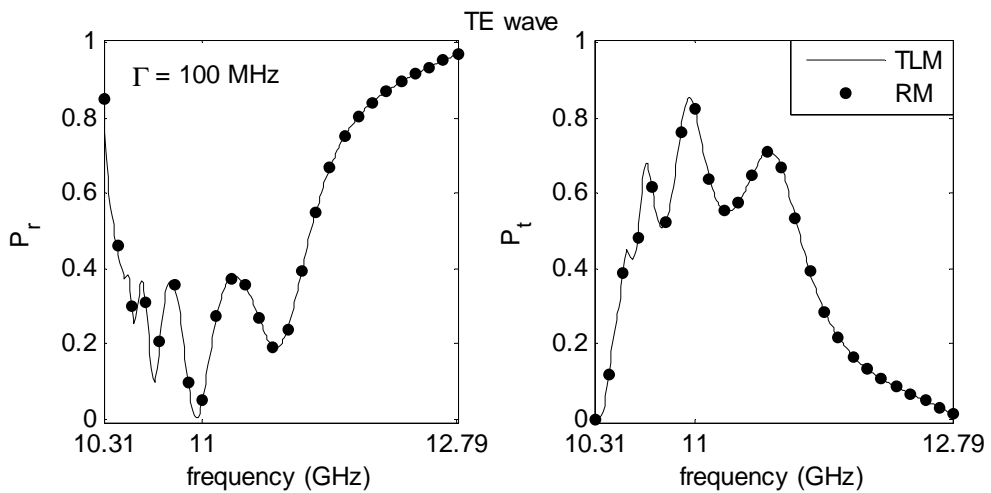
Figure A.8: Reproduction of Figure 4.11(a) and Figure 4.11(b) for TE wave when $\Gamma=100$ MHz using TLM and RM.

REFERENCES

[1] The web page of Prof. Dr. David R. Smith, University of California, San Diego. http://physics.ucsd.edu/~drs/

[2] Weiland T., Schuhmann R., Greegor R.P., Parazzoli C.G., Vetter A.M., Smith D.R., Vier D.C., and Schultz S. (2001). Ab initio numerical simulation of left-handed metamaterials: Comparison of calculations and experiments, *Journal of Applied Physics*, **90** (10), 5419–5424.

[3] Pendry J.B. (2001), Negative μ, negative ε, negative refractive index, and how to exploit them. *Electromagnetic Crystal Structures*, *Euroconference on Electromagnetic Confinement*, *from Basic Research to the Marketplace*, St. Andrews, Scotland, 9-14 June 2001.

[4] Metamaterials home page of the future projects of the Defense Advanced Research Projects Agency's (DARPA) Defense Sciences Office (DSO). http://www.darpa.mil/DSO/future/metamaterials/metamaterials.html

[5] Walser R.M. (2001). Electromagnetic metamaterials, Inaugural Lecture, *Proceedings of SPIE* (Complex Mediums II: Beyond Linear Isotropic Dielectrics; Lakhtakia A., Weiglhofer W.S., Hodgkinson I.J., Editors), **4467**, pp. 1–15.

[6] Caloz C. and Itoh T. (2005). Metamaterials for high-frequency electronics. *Proceedings of the IEEE*, **93** (10), 1744–1752.

[7] Sihvola A. (2003). Electromagnetic emergence in metamaterials. *Advances in Electromagnetics of Complex Media and Metamaterials* (Zouhdi S., Sihvola A., Arsalane M., Editors), Kluwer Academic Publishers, Dordrecht, (NATO Science Series II: Mathematics, Physics, and Chemistry), **89**, pp. 1–17.

[8] Bose J.C. (1898). On the rotation of plane of polarisation of electric waves by a twisted structure. *Proceedings of the Royal Society of London*, **63**, 146–152.

[9] Lindell I.V, Sihvola A.H., and Kurkijarvi J. (1992). Karl F. Lindman: The last Hertzian, and a Harbinger of electromagnetic chirality. *IEEE Antennas and Propagation Magazine*, **34** (3), 24–30.

[10] Kock W.E. (1948). Metallic delay lenses. *Bell System Technical Journal*, **27**, 58–82.

[11] Tinoco I.Jr. and Freeman P. (1957). The optical activity of oriented copper helices. I. Experimental. *Journal of Physical Chemistry*, **61**, 1196–1200.

[12] Harvey A.F. (1959). Optical Techniques at Microwave Frequencies. *Proceedings of the Institution of Electrical Engineers*, **106** (part B), 141–157.

[13] Veselago V.G. (1968). The electrodynamics of substances with simultaneously negative values of ε and μ. *Soviet Physics Uspekhi*, **10**, 509–514.

[14] Lamb H. (1904). On group – velocity. *Proceedings London Mathematical Society*, **s2-1** (1), 473–479.

[15] Schuster A. (1904). *An Introduction to the Theory of Optics*. London: Edward Arnold, pp. 313–318.

[16] Pocklington H.C. (1905). Growth of a wave-group when the group velocity is negative. *Nature*, **71**, 607–608.

[17] Mandel'shtam L.I. (1944). Lectures on certain problems in the theory of oscillations: Lecture 4. *Polnoe Sobraniye Trudov*, tom 5 (Leningrad: Izdat. Akademiya Nauk SSSR, 1950, pp. 461–467); *Lektsii po Optike*, Teorii Otnositel'nosti i Kvantovoi Mekhanike (Moscow: Nauka, 1972, pp. 431–437); in *Complete Collection of Works*, vol. 5, Moscow: Academy of Sciences, 1950, pp. 428–467; in English: http://ece-www.colorado.edu/~kuester/

[18] Mandel'shtam L.I. (1945). Group velocity in a crystal lattice. *Zhurnal Eksperimentalnoi i Teoreticheskoi Fiziki*, **15** (9), 475–478; Polnoe Sobraniye Trudov, tom 2 (Leningrad: Izdat. Akademiya Nauk SSSR, 1947, pp. 334–338);

English translation in *Sov. Phys. ZETF*, also in: http://ece-www.colorado.edu/~kuester/

[19] Malyuzhinets G.D. (1951). A note on the radiation principle. *Zhurnal Technicheskoi Fiziki*, **21**, 940–942.

[20] Sivukhin D.V. (1957). The energy of electromagnetic waves in dispersive media, *Opt. Spektrosk.*, **3**, 308–312.

[21] Pafomov V.E. (1956). *JETP*, **30** (4), 761–765.

[22] Pafomov V.E. (1957). *JETP*, **33** (4), 1074–1075.

[23] Pafomov V.E. (1959). *Soviet Physics-JETP*, **36** (6), 1853–1858.

[24] Silin R.A. (1959). Waveguiding properties of two-dimensional periodical slow-wave systems. *Voprosy Radioelektroniki, Elektronika*, **4**, 11–33.

[25] Silin R.A. (1972). Optical properties of artificial dielectrics. *Izv. VUZ Radiofiz.*, **15**, 809–820.

[26] Schneider H.J. and Dullenkopf P. (1977) Slotted tube resonator: A new NMR probe head at high observing frequencies. *Rev. Sci. Instrum.*, **48** (1), 68–73.

[27] Silin R.A. (1978). Possibility of creating plane-parallel lenses. *Opt. Spektrosk.*, **44**, 189–191. (English translation is available in OSA)

[28] Ulrich R. and Zengerle R. (1980). Optical Bloch waves in periodic planar waveguides. *Proceedings of the Topical Meeting on Integrated and Guided Wave Optics*, Incline Village, NV, USA, pp. TuB1/1–4.

[29] Hardy W.H. and Whitehead L.A. (1981). Split-ring resonator for use in magnetic resonance from 200-2000 MHz. *Rev. Sci. Instrum.*, **52** (2), 213–216.

[30] Camley R.E. and Mills D.L. (1982). Surface polaritons on uniaxial antiferromagnets. *Physical Review B*. **26**, 1280–1287.

[31] Zengerle R. (1987). Light propagation in singly and doubly periodic planar waveguides. *J. Mod. Optics*. **34**, 1589–1617.

[32] Khosravi H., Tilley D.R., and Loudon R. (1991). Surface polaritons in cylindrical optical fibers. *Journal of Optical Society of America A*, **8**, 112–122.

[33] Kostin M.V. and Shevchenko V.V. (1994). Artificial magnetics based on double circular elements. *Proceeding of Bianisotropics'94*, P´erigueux, France, pp. 49–56.

[34] Tretyakov S.A., Mariotte F., Simovski C.R., Kharina T.G., and Heliot J.-P. (1996). Analytical antenna model for chiral scatterers: Comparison with numerical and experimental data. *IEEE Transactions on Antennas Propagation*, **44** (7), 1006–1014.

[35] Pendry J.B., Holden A.J., Stewart W.J., and Youngs I. (1996). Extremely low frequency plasmons in metallic mesostructures. *Physical Review Letters*, **76**, 4773–4776.

[36] Pendry J.B., Holden A.J., Robbins D.J., and Stewart W.J. (1999). Magnetism from conductors and enhanced nonlinear phenomena. *IEEE Transactions on Microwave Theory and Techniques*, **47**, 2075–2084.

[37] Smith D.R., Padilla W.J., Vier D.C., Nemat-Nasser S.C., and Schultz S. (2000). Composite medium with simultaneously negative permeability and permittivity. *Physical Review Letters*, **84**, 4184–4187.

[38] Shelby R.A., Smith D.R., and Schultz S. (2001). Experimental verification of a negative index of refraction. *Science*, **292**, 77–79.

[39] Valanju P.M., Valser R.M., and Valanju A.P. (2002). Wave refraction in negative-index media: always positive and very inhomogeneous. *Physical Review Letters*, **88**, 187401.1–187401.4.

[40] Pendry J.B. and Smith D.R. (2003). Comment on wave refraction in negative-index media: always positive and very inhomogeneous. *Physical Review Letters*, **90**, 029703.1.

[41] Ziolkowsky R.W. and Heyman E. (2001). Wave propagation in media having negative permittivity and permeability. *Physical Review E*, **64**, 056625.1–056625.15.

[42] Kong J.A. (2002). Electromagnetic wave interaction with stratified negative isotropic media. *Progress in Electromagnetics Research* (*PIER*), **35**, 1–52.

[43] Engheta N. (2002). Ideas for potential application of metamaterials with negative permittivity and permeability. A chapter in the book entitled *Advances in Electromagnetics of Complex Media and Metamaterials*, NATO Science Series, the Proceedings of NATO Advanced Research Workshop in Marrakech (Bianisotropics'2002), (S. Zouhdi, A. H. Sihvola, and M. Arsalane, editors), Kluwer Academic Publishers, Inc., p. 19–37.

[44] Chew W.C. (2005). Some Reflections on Double Negative Materials, *Progress In Electromagnetics Research* (*PIER*), **51**, 1–26.

[45] Pendry J.B. (2000). Negative refraction makes a perfect lens. *Physical Review Letters*, **85**, 3966–3969.

[46] Tretyakov S.A. (2001). Meta-material with wideband negative permittivity and permeability. *Microwave and Optical Technology Letters*, **31**, 163–165.

[47] Caloz C., Chang C.C., and Itoh T. (2001). Full-wave verification of the fundamental properties of left-handed materials in waveguide configurations. *Journal of Applied Physics*, **90**, 5483–5486.

[48] Bayindir M., Aydin K., Ozbay E., Markos P., and Soukoulis C.M. (2002). Transmission properties of composite metamaterials in free space. *Applied Physics Letters*, **81** (1), 120–122.

[49] Special issue on metamaterials. (2003). *IEEE Transaction on Antennas Propagation*, **51**, 2545–3018.

[50] Ziolkowski R.W. (2003). Pulsed and CW Gaussian beam interactions with double negative metamaterial slabs. *Optics Express*, **11**, 662–681.

[51] Ozbay E., Aydin K., Cubukcu E., and Bayindir M. (2003). Transmission and Reflection Properties of Composite Double Negative Metamaterials in Free Space. *IEEE Transaction on Antennas Propagation*, **51** (10), 2592–2595.

[52] Smith D.R., Pendry J.B., and Wiltshire M.C.K. (2004). Metamaterials and negative refractive index. *Science*, **305**, 788–792.

[53] Alu A. and Engheta N. (2004). Guided Modes in a Waveguide Filled With a Pair of Single-Negative (SNG), Double-Negative (DNG), and/or Double-Positive (DPS) Layers. *IEEE Transaction on Microwave Theory and Techniques*, **52**, 199–210.

[54] Mahmoud S.F. and Viitanen A.J. (2005). Surface wave character on a slab of metamaterial with negative permittivity and permeability. *Progress in Electromagnetics Research* (*PIER*), **51**, 127–137.

[55] Shu W. and Song J.M. (2006). Wave propagation in grounded dielectric slabs with double negative metamaterials. *Progress in Electromagnetics Research Symposium 2006*, Cambridge, USA, pp. 246–250.

[56] Guven K. and Ozbay E. (2006). Near field imaging in microwave regime using double layer split-ring resonator based metamaterial. *Opto-Electronics Review*, **14**, 213–216.

[57] Sabah C., Ögücü G., and Uckun S. (2006). Power analysis of plane waves through a double-negative slab. *4th International Workshop on Electromagnetic Wave Scattering – EWS'2006*, Gebze Institute of Technology, Gebze, Kocaeli, Turkey, pp. 11.61–11.66.

[58] Shi Y., Li Y., and Liang C.-H. (2006). Perfectly matched layer absorbing boundary condition for truncating the boundary of the left-handed medium. *Microwave and Optical Technology Letters*, **48**, 57–63.

[59] Ergul O., Unal A., and Gürel L. (2006). Efficient and accurate analysis of large metamaterial structures with the multilevel fast multipole algorithm. *IV. International Workshop on Electromagnetic Wave Scattering (EWS)*, Gebze Institute of Technology, Gebze, Kocaeli, Turkey, pp. 8.15–8.20.

[60] Gokkavas M., Guven K., Bulu I., Aydın K., Penciu R.S., Kafesaki M., Soukoulis C. M., and Ozbay E. (2006). Experimental demonstration of a left-handed metamaterial operating at 100 GHz. *Physical Review B*, **73**, 193103.1–193103.4.

[61] Aydin K. and Ozbay E. (2007). Experimental investigation of reflection characteristics of left-handed metamaterials in free space. *IET Microwaves Antennas and Propagation*, **1** (1), 89–93.

[62] Sabah C., Ögücü G., and Uckun S. (2006). Reflected and transmitted powers of electromagnetic wave through a double-negative slab. *Journal of Optoelectronics and Advanced Materials* (*JOAM*), **8**, 1925–1930.

[63] Sabah C. and Uckun S. (2007). Electromagnetic wave propagation through the frequency-dispersive and lossy double-negative slab. *Opto-Electronics Review*, **15**, 133–143.

[64] Sabah C. and Uckun S. (2007). Frequency response of multilayer media comprised of double-negative and double-positive slabs. *Chinese Physics Letters*, **24** (5), 1242–1244.

[65] Sabah C. and Uckun S. (2007). Physical features of left-handed mirrors in millimeter wave band. *Journal of Optoelectronics and Advanced Materials* (*JOAM*), **9**, 2480–2484.

[66] Sabah C. and Uckun S. (2007). Scattering characteristics of the stratified double-negative stacks using the frequency dispersive cold plasma medium. *Zeitschrift für Naturforschung A* (*A Journal of Physical Sciences*), **62a** (5), 247–253.

[67] Szentpali B. (2003). Metamaterials: a new concept in the microwave technique. *Microwave Review* (*Mikrotalasna Revija*), **9** (2), 35–40.

[68] Jaksic Z., Dalarsson N., and Maksimovic M. (2006). Negative refractive index metamaterials: principles and applications. *Microwave Review* (*Mikrotalasna Revija*), **12** (1), 36–49.

[69] Pendry J.B. and Ramakrishna S.A. (2003). Refining the perfect lens. *Physica B*, **338**, 329–332.

[70] Fang N. and Zhang X. (2003), Imaging properties of a metamaterial superlens. *Applied Physics Letters*, **82**, 161–163.

[71] Grbic A. and Eleftheriades G.V. (2003). Subwavelength Focusing Using a Negative-Refractive-Index Transmission Line Lens. *IEEE Antennas and Wireless Propagation Letters*, **2**, 186–189.

[72] Bulu I., Caglayan H., and Ozbay E. (2006). Experimental demonstration of subwavelength focusing of electromagnetic waves by labyrinth-based two-dimensional metamaterials. *Optics Letters*, **31** (6), 814–816.

[73] Lindell I.V., Tretyakov S.A., Nikoskinen K.I., and Ilvonen S. (2001). BW media − media with negative parameters, capable of supporting backward waves. *Microwave and Optical Technology Letters*, **31**, 129–133.

[74] Shamonina E. and Solymar L. (2007). Metamaterials: how the subject started. *Metamaterials*, **1**, 12–18.

[75] Linden S., Enkrich C., Klein M., Dolling G., Feth N., and Wegener M. (2006). Metamaterials. http://www.aph.uni-karlsruhe.de/ag/wegener/meta/meta.html

[76] Dolling G., Wegener M., Linden S., and Hormann C. (2006). Photorealistic images of objects in effective negative-index materials. *Optics Express*, **14** (5), 1842–1849.

[77] Landau L.D. and Lifshitz E.M. (1984). *Electrodynamics of continuous media*. (Second edition revised and enlarged by Lifshitz E.M. and Pitaevskii L.P.) (Translated from the Russian by Sykes J.B., Bell J.S., and Kearsley M.J.) Oxford, New York, Beijing, Frankfurt: Pergamon Press. (Original work published in 1960).

[78] Pendry J.B. and Smith D.R. (2004). Reversing light with negative refraction. *Physics Today*, **57** (6), 37–43.

[79] Smith D.R., Schultz S., Markos P., and Soukoulis C.M. (2002). Determination of effective permittivity and permeability of metamaterials from reflection and transmission coefficients. *Physical Review B*, **65**, 195104.1–195104.5.

[80] Cui T.J. and Kong J.A. (2004). Time-domain electromagnetic energy in a frequency-dispersive left-handed medium. *Physical Review B*, 70, 205106.1–205106.7.

[81] Woodley J.F. and Mojahedi M. (2004). Negative group velocity and group delay in left-handed media. *Physical Review E*, **70**, 046603.1–046603.6.

[82] Lee J.-Y., Lee J.-H., Kim H.-S., Kang N.-W., and Jung H.-K. (2005). Effective Medium Approach of Left-Handed Material Using a Dispersive FDTD Method. *IEEE Transactions on Magnetics*, **41** (5), 1484–1487.

[83] Pendry J.B., Holden A.J., Robbins D.J., and Stewart W.J. (1998). Low frequency plasmons in thin-wire structures. *Journal of Physics: Condensed Matter*, **10**, 4785–4809.

[84] Tretyakov S. (2007). On geometrical scaling of split-ring and double-bar resonators at optical frequencies. *Metamaterials*, **1**, 40–43.

[85] Young J.L. and Nelson R.O. (2001). A summary and systematic analysis of FDTD algorithms for linearly dispersive media. *IEEE Antennas and Propagation Magazine*, **43** (1), 61–77.

[86] Hao Y., Lu L., and Parini C.G. (2003). Dispersive FDTD modeling on multi-layer left-handed meta-materials for near/far field imaging at microwave frequencies. *IEEE Antennas and Propagation Society International Symposium*, Columbus, Ohio, USA, vol. 4, pp. 639–642.

[87] Hoa Y. (2006). From electromagnetic bandgap to left-handed metamaterials: modelling and applications. *Journal of Zhejiang University SCIENCE A*, **7** (1), 34–40.

[88] Engheta N. and Ziolkowski R.W. (Editors). (2006). *Metamaterials − Physics and Engineering Explorations*. Piscataway, NJ: IEEE-Wiley Press.

[89] Staelin D.H., Morgenthaler A.W., and Kong J.A. (1994). *Electromagnetic Waves*. New Jersey: Prentice Hall International Editions.

[90] Cory H. and Zach C. (2004). Wave propagation in metamaterial multi-layered structures. *Microwave and Optical Technology Letters*, **40** (6), 460–465.

[91] Orfanidis S.J. (2004). *Electromagnetic Waves and Antennas*. Online text book. www.ece.rutgers.edu/~orfanidi/ewa.

[92] Gerardin J. and Lakhtakia A. (2002). Negative index of refraction and distributed Bragg reflectors. *Microwave and Optical Technology Letters*, **34** (6), 409–411.

[93] Ramadan O. (2006). An efficient state-space ADI-PML algorithm for truncating DNG metamaterial FDTD domains. *Microwave and Optical Technology Letters*, **49**, 494–498.

[94] Karkkainen M.K. (2003). *Numerical study of wave propagation in uniaxially anisotropic Lorentzian backward-wave slabs*. *Physical Review E*, **68**, 026602.1–026602.6.

[95] Engheta N. and Ziolkowski R.W. (2005). A positive future for double-negative metamaterials. *IEEE Transactions on Microwave Theory and Techniques*, **4**, 1535–1556.

[96] Sabah C. and Ögücü G. (2006). Reflection from and transmission through the double-negative slab. *Journal of Optoelectronics and Advanced Materials (JOAM)*, **9** (6), 1861–1864.

[97] Ziolkowski R.W. (2003). Design, fabrication, and testing of double negative metamaterials. *IEEE Transaction on Antennas and Propagation*, **51** (7), 1516–1529.

[98] Chen X., Grzegorczyk T.M., Wu B.-I., Pacheco J., and Kong J.A. (2004). Robust method to retrieve the constitutive effective parameters of metamaterials. *Physical Review E*, **70** (1), 016608.1–016608.7.

[99] Linden S., Enrich C., Wegener M., Zhou J., Koschny T., and Soukoulis C.M. (2004). Magnetic Response of Metamaterials at 100 Terahertz. *Science*, **306** (5700), 1351–1353.

[100] Smith D.R., Vier D.C., Koschny Th., and Soukoulis C.M. (2005). Electromagnetic parameter retrieval from inhomogeneous metamaterials. *Physical Review E*, **71** (3), 036617.1–036617.11.

[101] Aydin K., Guven K., Kafesaki M., Soukoulis C.M., and Ozbay E. (2005). Investigation of magnetic resonances for different split-ring resonator parameters and designs. *New Journal of Physics*, **7**, 168.1–168.15.

[102] Aydin K. and Ozbay E. (2006). Identifying magnetic response of split-ring resonators at microwave frequencies. *Opto-Electronics Review*, **14** (3), 193–199.

[103] Liu Y., Fang N., Wu D., Sun C., and Zhang X. (2007). Symmetric and antisymmetric modes of electromagnetic resonators. *Applied Physics A – Materials Science & Processing*, **87** (2), 171–174.

[104] Chen H.-T., O'Hara J.F., Taylor A.J., Averitt R.D., Highstrete C., Lee M., and Padilla W.J. (2007). Complementary planar terahertz metamaterials. *Optics Express*, **15** (3), 1084–1095.

[105] Gundogdu T.F, Gökkavvas M., Guven K., Kafesaki M., Soukoulis C.M., and Ozbay E. (2007). Simulation and micro-fabrication of optically switchable split ring resonators. *Photonics and Nanostructures – Fundamental and Applications*, **5**, 106–112.

[106] Sabah C. and Uckun S. (2008). Triangular split ring resonator and wire strip to form new metamaterial. Accepted for publication in the *Proceedings of XXIX General Assembly of the International Union of Radio Science*, Chicago, Illinois, USA, August 07-16, 2008.

<div align="center">**CIRRICULUM VITAE**</div>

PERSONAL INFORMATION

Surname, Name: SABAH, Cumali

Nationality: Turkish (TC)

Date and Place of Birth: 10 August 1977, İskenderun / Hatay

Phone: +90 342 3172144

Fax: +90 342 3601103

email: sabah@gantep.edu.tr

EDUCATION

Degree	Institution	Year of Graduation
MS	University of Gaziantep	2004
BS	University of Gaziantep	2001
High School	İskenderun High School	1995

WORK EXPERIENCE

Year	Place	Enrollment
2002- Present	University of Gaziantep	Research Assistant

FOREIGN LANGUAGES: English

PUBLICATIONS

International Journal Papers:

Sabah C. and Uckun S., "Reflection and transmission coefficients of multiple chiral layers", Science in China Series E: Technological Sciences, vol. 49, no. 4, pp. 457–467, 2006.

Sabah C. and Uckun S., "Mirrors with chiral slabs", Journal of Optoelectronics and Advanced Materials (JOAM), vol. 8, no. 5, pp. 1918–1924, 2006.

Sabah C., Öğücü G., and Uckun S., "Reflected and transmitted powers of electromagnetic wave through a double-negative slab", Journal of Optoelectronics and Advanced Materials (JOAM), vol. 8, no. 5, pp. 1925–1930, 2006.

Sabah C. and Uckun S., "Scattering characteristics of the stratified double-negative stacks using the frequency dispersive cold plasma medium", Zeitschrift für Naturforschung A (A Journal of Physical Sciences), vol. 62a, no. 5, pp. 247–253, 2007.

Sabah C. and Uckun S., "Frequency response of multilayer media comprised of double-negative and double-positive slabs", Chinese Physics Letters, vol. 24, no. 5, pp. 1242–1244, 2007.

Sabah C. and Öğücü G., "Reflection from and transmission through the double-negative slab", Journal of Optoelectronics and Advanced Materials (JOAM), vol. 9, no. 6, pp. 1861–1864, 2007.

Sabah C. and Uckun S., "Electromagnetic wave propagation through the frequency-dispersive and lossy double-negative slab", Opto-Electronics Review, vol. 15, no. 3, pp. 133–143, 2007.

Sabah C. and Uckun S., "Physical features of left-handed mirrors in millimeter wave band", Journal of Optoelectronics and Advanced Materials (JOAM), vol. 9, no. 8, pp. 2480–2484, 2007.

Conference Papers:

Sabah C. and Uckun S., "Power reflection and transmission coefficients in multilayer chiral media," 10th National Electrical, Electronics and Computer Engineering Congress, Istanbul, Turkey, September, 2003 (in Turkish).

Sabah C. and Uckun S., "Plane wave reflection and transmission through multilayer chiral slabs," Bianisotropic 2004, 10th International Conference on Complex Media and Metamaterials, Het Pand, Ghent, Belgium, September, 2004.

Sabah C. and Uckun S., "Filter properties of chiral mirrors," II. URSI-Turkey 2004 Scientific Congress, Ankara, Turkey, September, 2004 (in Turkish).

Sabah C. and Uckun S., "Properties of Chiral Mirrors based on Bragg Reflectors," The Second IASTED International Multi-Conference on Antennas, Radar, and Wave Propagation, Banff, Canada, July, 2005.

Sabah C. and Uckun S., "Metamaterials which have negative permittivity and permeability and transmission line approach," 11th National Electrical, Electronics and Computer Engineering Congress, Istanbul, Turkey, September, 2005 (in Turkish).

Sabah C., Öğücü G., and Uckun S., "Reflection and transmission coefficients for electromagnetic wave coming through the surface of double-negative slab – normal incidence case", III. URSI-Turkey 2006 Scientific Congress, Ankara, Turkey, September, 2006 (in Turkish).

Sabah C., Gökpınar S., and Uckun S., "Analysis of metamaterials using transmission line approach", III. URSI-Turkey 2006 Scientific Congress, Ankara, Turkey, September, 2006 (in Turkish).

Sabah C., Öğücü G., and Uckun S., "Power analysis of plane waves through a double-negative slab", IV. International Workshop on Electromagnetic Wave Scattering – EWS'2006, Gebze Institute of Technology, Gebze – Kocaeli, Turkey, 2006.

Sabah C., Urbani F., and Uckun S., "Frequency Dependence of Bloch Impedance in Left-Handed Transmission Line," The Second European Conference on Antennas and Propagation (EuCAP 2007), EICC, Edinburgh, UK, November, 2007.

Sabah C., and Uckun S., "Triangular split ring resonator and wire strip to form new metamaterial," Accepted for publication in the Proceedings of XXIX General Assembly of the International Union of Radio Science, Chicago, Illinois, USA, August 07-16, 2008.

HOBBIES & ACTIVITIES:

Columnist, Mathematics, Physics, Authorship, Art, Philosophy, Chess, World Literature, Jogging, Swimming, Gardening.